Spring 2008

Indication of cylinder pressure rise rate by means of vibration and acoustic emissions of an internal combustion engine

Jeffery A. Massey

Department:

INDICATION OF CYLINDER PRESSURE RISE RATE BY MEANS OF VIBRATION AND ACOUSTIC EMISSIONS OF AN INTERNAL COMBUSTION ENGINE

by

JEFFERY A. MASSEY

A THESIS

Presented to the Graduate Faculty of the

MISSOURI UNIVERSITY OF SCIENCE AND TECHNOLOGY

In Partial Fulfillment of the Requirements for the Degree

MASTER OF SCIENCE IN MECHANICAL ENGINEERING

2008

Approved by

James A. Drallmeier, Advisor
Walter Eversman
Dan McAdams

ABSTRACT

The focus of this study is to investigate the ability of the vibration and acoustic emissions of an internal combustion engine to indicate the cylinder pressure rise rate (PRR). Investigations are conducted on both a small-single cylinder spark-ignition (SI) engine and a larger multi-cylinder compression-ignition (CI) engine. Vibration measurements were made on both engines, however only acoustic measurements were made on the SI engine. Specific vibration and acoustic frequency bands were identified as correlating to energy generated from combustion and energy generated by cylinder cavity resonances.

Initial investigation into general trends of the SI engine's vibration and acoustic emissions showed the energy levels, in the specified frequency bands, increased as both speed and load was increased. The PRR increased with load and decreased with speed, therefore the acoustic and vibration emissions of the SI engine operating under normal spark-ignited combustion was unable to indicate, on average, the level of PRR for all operating conditions. Per-cycle investigations showed high load set points, regardless of engine speed, exhibited a near linear increasing trend between the vibration and acoustic emissions and the PRR. CI engine investigations showed, for a single speed and load set point of 1500 rpm and 37.3 N-m, respectively, the vibration emission also exhibited an increasing trend with the PRR when the fuel injection timing was varied. It was concluded that for SI and CI engines with high energy release rates, non-intrusive sensing techniques have the ability to indicate the level of the initial energy release rates. These results were validated for engine set point average and cycle-to-cycle investigations.

ACKNOWLEDGEMENTS

First, I would like to thank the Missouri University of Science and Technology for allowing me the opportunity to attend graduate school as well as the opportunity to conduct thesis research. Thanks to Kawasaki Motors Manufacturing for providing the project topic and funding for the current research. I would like to thank Dr. James A. Drallmeier and Dr. Daniel McAdams for providing the financial means that has made my graduate school experience available. I would especially like to thank Dr. Drallmeier for his guidance and patience throughout the past two years and for introducing me to internal combustion engine research. I also want to thank Dr. Walt Eversman for answering my innumerable questions and helping me gain a better understanding of the physics of acoustics. I would also like to thank the members of my thesis committee, Dr. Drallmeier, Dr. Eversman, and Dr. McAdams, for giving their time and effort in reviewing and criticizing my thesis.

Secondly, I would like to thank Mark Friedrich, Brian Kaul, David Burd, Nathan Wilke and Clint Cary for all the help they have given me in and out of the lab for the past two years. I also want to acknowledge the Missouri S & T Mechanical Engineering Technical Shop employees. They have been instrumental in the progress of my research.

Finally, I would like to give special thanks my wife, Holly, for the love and support she has given me the past three and a half years of my academic career. I would also like to thank my Parents for their support and for teaching me a solid work ethic.

TABLE OF CONTENTS

LIST OF ILLUSTRATIONS

Page

LIST OF TABLES

Page

NOMENCLATURE

Symbol	Description
B	Bore
C	Speed of sound
$dP/d\theta$	First derivative of pressure
f	Frequency
k	Wave number
m	Circumferential mode number
n	Radial mode number
N	Number of samples
p	Cylinder pressure
P	Pressure
r	radius
R	Correlation coefficient
R^2	Square correlation coefficient
$S(\omega)$	Power spectrum
T	Time period
V	Volume
V_d	Displacement volume
Δf	Frequency resolution
$\rho\ (m,n)$	Vibration mode factor

ABBREVIATIONS

a.u.	Arbitrary Units
ABDC	After Bottom Dead Center
AC	Alternating Current
ATDC	After Top Dead Center
BBDC	Before Bottom Dead Center
BCW	Bottom Cylinder Wall
BNC	Bayonet Neill-Concelman
BTDC	Before Top Dead Center
CAD	Crank Angle Degree
CDI	Common Rail Direct Injection
CI	Compression Ignition
DAQ	Data acquisition
DC	Direct Current
DFT	Discrete Fourier Transform
EGR	Exhaust Gas Recirculation
EVC	Exhaust Valve Close
EVO	Exhaust Valve Open
FEERG	Fuels, Engines, and Emissions Research Group
FFT	Fast Fourier Transform
FIR	Finite Impulse Response
HCCI	Homogeneous Charge Compression Ignition
ICP	Integrated Circuit – Piezoelectric

IMEP	Integrated Mean Effective Pressure
IMEPn	Net Integrated Mean Effective Pressure
IVC	Intake Valve Close
IVO	Intake Valve Open
LCW	Lower Cylinder Wall
LED	Light Emitting Diode
MBT	Maximum Brake Torque
MST	Missouri University of Science and Technology
MU	Mechanical Unit
NI	National Instruments
NTRC	National Transportation and Research Center
NVH	Noise, Vibration, and Harshness
OEM	Original Equipment Manufacturer
PRR	Pressure Rise Rate
RMS	Root Mean Square
SI	Spark Ignition
SOC	Start of Combustion
SPL	Sound Pressure Level
STFT	Short Time Fourier Transform
TDC	Top Dead Center
TF	Time-Frequency
TTL	Transistor-Transistor Logic
UCW	Upper Cylinder Wall

1. INTRODUCTION

In response to the demand for cleaner, more efficient engine operation, engine manufacturers and researchers are developing advanced engine operating modes that have been just recently realized. One unfortunate result of these advanced operating modes is the high cyclic variability that accompanies them. Engine manufacturers and researchers must develop methods in which to diagnose and control these advanced combustion modes in order to properly implement them into the next generation of internal combustion engines. Therefore, as the demand for cleaner, more efficient engine operation rises, so do the needs for inexpensive non-intrusive engine diagnostic and control technologies.

The ideal sensing technique would be the use of an in-cylinder mounted pressure transducer. However, the pressure transducers are subject to the combustion process and must be built to withstand very harsh work environments. This makes them an expensive addition to diagnostic and control technologies for internal combustion engines. Conversely, surface mounted vibration sensors have become quite useful in monitoring the operating condition of an engine. For example, these sensors provide feedback as to when a spark ignition engine is undergoing knock. From the surface vibrations sensed, the spark timing can be adjusted to eradicate the auto-ignition of the fuel-air mixture (the phenomenon creating knock in a spark ignition engine). The use of vibration sensors for diagnostic and control of internal combustion engines provides a low cost alternative to the in-cylinder pressure transducer. Vibration sensors are also easily implementable since they are a non-intrusive sensor with very mature sensing technologies.

Another non-intrusive sensing technique is monitoring the acoustic emission of an engine. Initially, acoustic emission investigations of internal combustion engines have been focused mainly on engines undergoing auto-ignition of the combustion products e.g. diesel engines. This is mostly due to the large amount of annoying noise emitted from engines operating under auto-ignited combustion. These studies have shown the magnitude of the acoustic emission is heavily dependent upon the rate at which the cylinder pressure rises at the onset of combustion. Conversely, only a small amount of work with regard to relating the cylinder pressure rise rate and acoustic emission has been conducted for spark ignition engines operating under normal spark ignited combustion. The fact that the acoustic emission is related to the cylinder pressure rise rate is interesting because the rate of pressure rise can provide indication of the initial rate at which the energy is being released during an engine cycle. This type of information is useful in diagnosing or controlling an internal combustion engine. More recently, acoustic emission has been investigated as a measurement by which to detect faults in an operating engine. Results from such studies have exemplified the potential for acoustic emission for sensing internal combustion engine operating conditions.

Unfortunately, non-intrusive sensing techniques have only been used for diagnosing extreme changes in an engine operating condition. The introduction of advanced engine operating modes has ushered in new research focused on developing vibration and acoustic sensing technologies to provide better diagnostics of the engine operating condition on a more refined scale i.e. on a per engine cycle basis. Therefore, the focus of this study was to investigate the ability of the vibration and acoustic sensors to indicate specific information with regard to the combustion process. Specifically for

this study, the cylinder pressure rise rate. The investigation was conducted on an engine operating condition average and cycle-to-cycle basis to establish the viability of such non-intrusive sensing techniques for high level diagnostic and control in internal combustion engines.

2. LITERATURE REVIEW

Many have investigated the sources of vibration and acoustic emissions of internal combustion engines. Initial investigations focused primarily on compression-ignition (CI) engines due to the increased amount of acoustic emission over the spark-ignition (SI) engine and, correspondingly, their increased annoyance. Later investigations have focused on the knock phenomenon occurring in SI engines. Both the CI combustion process and SI knock are initiated by auto-ignition of the fuel air mixture and result in audibly noisier engine operation. Recently, investigations have been conducted on the acoustic and vibration emissions from engines operating under advanced combustion modes. Investigations on internal combustion engines range from noise source generation to vibration and acoustic transmission paths.

Priede [1] performed a fundamental study of the relation between the form of the cylinder pressure diagram and emitted noise from both indirect (IDI) and direct injection (DI) CI engines. It was shown that the overall emitted noise was dependent upon the form of cylinder pressure rise which could be fully described by the cylinder pressure spectra. Priede investigated the influence of both mechanical noise (such as valve opening and closing events, piston cylinder interaction, piston/connecting rod/crankshaft mechanism interaction, etc..), characterized by the noise emitted when motoring the engine, and the combustion noise, characterized by the cylinder pressure level on the overall emitted engine noise. It was determined that the prominent noise source (mechanical or combustion) was dependent upon the engine geometry (e.g. bore and stroke, or inline- or V-cylinder arrangement) and rate of pressure rise due to combustion.

For an abrupt pressure rise, bulk gas pressure oscillations excite the resonant modes of the cylinder cavity and thus increase the combustion noise emitted in the frequency range of these resonant modes. Conversely, smooth pressure development results in much lower acoustic emission resulting from combustion and the mechanical noise is dominant in the overall noise emitted from the engine. This work was focused on characterizing the overall sound-pressure-level (SPL) of the engine and no cycle-to-cycle variations were considered, nor were SI acoustic emission investigated. Also, characterizing mechanical noise as the motored engine acoustic SPL is insufficient to capture increases in engine structure loads, such as piston slap force, resulting from combustion.

In a following investigation conducted by Anderton [2], an overall relation between the combustion system and engine noise was developed. This relation was derived from the cylinder pressure spectra for various combustion systems (e.g. IDI CI, DI CI, and SI). Anderton noted that previous research conducted showed when combustion is abrupt, the peak heat release rate and peak rate of cylinder pressure rise have a direct correlation and thus combustion noise can be correlated to both. Conversely, when combustion is smooth, such as in a SI engine, the combustion noise can only be related to the form of cylinder pressure development and peak pressure. The focus of his study was developing a model by which to predict combustion noise based on the in-cylinder pressure measurements. No investigation was conducted with regard to specific characteristics of the engine's acoustic and vibration time signatures or spectral energy in relation to the cylinder pressure spectra.

In an effort to study more fundamentally the noise generation sources, Schneider et al. [3] studied the regularities of the cylinder pressure oscillations and their effects on

the combustion process and noise in a CI engine. From this study it was evident the resonant frequencies characteristic of the cylinder bore imposed regular oscillations in the CI engine combustion chamber. Interestingly, Schneider et al. claimed the fixed eigen-frequencies of the engine structure superpose the cylinder resonant frequencies of the combustion process and prohibit separation of the cylinder resonant frequencies from the measured surface vibrations and external acoustic measurements. This conclusion was premature as more recent investigations have shown reasonable correlation between cavity resonances and structure vibration.

After initial investigations had been focused on the rate of cylinder pressure rise in CI engines, Priede [4] and Dutkiewicz performed an investigation of the acoustic response of a gasoline engine under normal and knocking conditions. By motoring the engine and varying the compression pressure via a butterfly throttle valve, it was noticed that higher compression pressures resulted in an increase in high frequency noise. They also investigated the impact of advancing the spark timing to the point of engine knock. If the spark timing was advanced but not to the point of knock, it was noticed that with a 5° advance, the overall engine noise increased 1 dBA, with the noise frequency spectra showing the increase in energy but retaining its overall shape. This type of analysis was done over a range of speeds and thus it was concluded the natural frequencies of the engine determine the basic shape of the noise spectra. When the engine spark timing was advanced to the point of knocking, it was clearly shown the engine noise emitted was highly dependent upon the structure i.e. cylinder cavity resonances. Therefore, it was concluded the overall noise level of an SI engine under normal conditions was dependent upon peak cylinder pressures for normal combustion and pressure rise rate for knocking

conditions. However, no work was done with regard to establishing transmission paths of the forces exerted in the cylinder by the high pressures and fast pressure rise resulting from combustion. Also, cycle-to-cycle variations were not investigated.

To investigate the comparison of the auto-ignition process in CI and SI engines, Schaberg et al. [5] investigated the effects of a rapid pressure rise on the vibration and acoustic emission of both a CI engine running under normal conditions and a SI engine running under knocking conditions. Spectral analysis comparison of the in-cylinder pressure from the CI and SI engines showed the contribution of the pressure oscillations accompanying the regular auto-ignition combustion process of CI engine was not significant to the overall noise levels. However, the noise due to the pressure oscillations from the auto-ignition process resulting in knock in a SI engine was predominate in the overall noise levels of the engine. Accelerometers were placed on the vertical bearing cap of the CI and SI engines. It was concluded, for the CI engine, the bearing cap vibrations were influenced by the rate of pressure rise and were a major contributor to the overall engine noise. Investigation into the differences in common passenger car CI and knocking SI engines were conducted as well. The CI engine emitted higher noise levels but a direct reason for this phenomenon was not established. It was speculated the higher compression pressures just before TDC in the CI engine may the underlying reason. Note that accelerometers were not place on the engine block and thus investigation into the cylinder block vibration and noise generating phenomena were not investigated.

To begin investigation into noise generating phenomena of engine structure vibrations, Vora [6] and Ghosh investigated the vibration response of a SI engine to piston slap and of a CI engine to combustion. For the SI investigation, accelerometers

were placed on the cylinder walls normal to the piston skirt location at TDC. Speed and load were varied to detect any dependence of piston slap induced vibrations from each. It was noticed that as the speed increased, the amplitude of the excitation frequency increased. This is expected since the excitation frequency of the engine is entirely dependent upon engine speed. Conversely, the vibration level of the excitation frequency was not dependent upon load (i.e. brake power), however the maximum level of vibration for a cycle was dependent upon load. Vora and Ghosh concluded that vibrations induced by piston slap in a SI engine occur below 500 Hz. They also investigated the influence of combustion on the axial vibration of a CI engine cylinder. It was concluded the vibration from the CI engine was dependent upon the peak value of the first derivative of the pressure i.e. peak pressure rise rate. Note that only piston slap was investigated for the SI engine and no experimental work was done with regard to low frequency combustion noise or cavity resonances.

Kanda et al. [7] studied the source, transmission and radiation characteristics of noise generation of a diesel engine. From this investigation it was concluded the combustion and piston slap noises made up 80% of the overall noise emitted from the engine. It was also concluded that 80% of the total noise was radiated from four main parts: the flywheel, gear case, oil pan and cylinder block. Results were reported to be consistent for different engine speeds; however the operating engine load was not reported in the results. Kanda et al.'s research was primarily focused on transmission paths. Noise generation phenomena were not correlated to specific vibration and acoustic characteristics.

Carlucci et al. [8] investigated using measured block vibrations as a way of monitoring the combustion evolution in a CI engine. Fuel injection timing was varied resulting in various types of combustion. The S-method time-frequency representation was used to investigate any connection between the in-cylinder pressure and vibration signals. It was seen that the peak power in the frequency components revealed on the pressure signal were detected by the vibration signal with a time collocation directly linked to the combustion development. Investigation of a correlation of the frequency content or vibration generating phenomena was not conducted.

Another investigation of engine structure vibration response to combustion was conducted by Carlucci et al. [9]. For this investigation, injection parameters were varied, resulting in changes in combustion development, to determine the effect of these changes on the engine block vibrations of a CI engine. The first derivative of the pressure and the heat release rate were calculated to investigate the relation of "internal parameters" useful to describe the combustion process and the engine structure vibrations. It was observed that at the highest level of injection pressure, both the pilot injection timing and duration variations could be outwardly detected. The injection pressure was always clearly detectable causing a coherent trend of the "internal parameters" and the engine vibration signals. It was suggested further study should be conducted with regard to the relation of the "internal parameters" and engine structure vibrations.

In an effort to advance vibration and acoustic analysis techniques appertaining to engine research, Chiatti [10, 11] and Chiavola performed experimental analysis with regard to estimating a mean frequency for the cylinder pressure trace in SI and CI engines. This estimation involved averaging the spectral energy for small time windows

and thus resolving an evolution in time of the "spectral composition" of the cylinder pressure. Experimental investigations were done over a range of speeds and loads. Results showed mean frequency values concentrated in lower frequency bands and was deemed useless for the current study. It was speculated such an analysis technique could provide insight to the acoustic emission of an engine, however no experimental results were presented to verify such a claim.

Patro [12] conducted time-frequency analysis of a CI engine using the Short-Time Fourier Transform (STFT). From the time-frequency (TF) plots it was noticed that not only did the pressure rise effect the noise, vibration, and harshness (NVH) of the engine, but the pressure fall also generated high frequency combustion excited NVH. Therefore, it was speculated the engine NVH may be more dependent upon the rate of heat release rather than just the pressure rise rate and peak pressure. However, no results from such an investigation were presented. Patro also compared the indicated mean effective pressure values to the measured structure vibrations and recorded sound pressure levels. It was concluded that if the indicated mean effective pressure (IMEP) levels could be lowered, many of the structure borne noise levels could be reduced and some noticeable improvements in powertrain roughness would be realized.

In another effort to understand analysis techniques used in engine vibration and acoustic investigations, an interesting study was conducted by Villarroel [13] and Agren. They used wavelet transforms to investigate characteristics of surface vibrations in an 11L diesel engine. Wavelet transforms are capable of providing time-frequency representation of a discrete signal, much like the STFT. It was shown that the wavelet transform was capable of indicating events considered to be the "combustion pulse" and

piston slap. This study was a preliminary investigation and primarily focused on comparison of the wavelet analysis to the conventional Fourier transform analysis. Wavelet analysis provides superior time-frequency representation compared to the STFT because it adjusts the time window width to the corresponding frequency band i.e. longer time windows for low frequencies and shorter time windows for high frequencies. One drawback to this method is the computational resources it requires and therefore was not used in the current investigation.

In a more recent study, Stoffels [14] and Collings investigated the effect of the advanced combustion mode homogenous-charge-compression-ignition (HCCI) on engine acoustics and vibration. They operated a four-cylinder in-line gasoline engine under both normal SI and HCCI operations. Results showed the HCCI combustion delivers maximum cylinder pressures and cylinder pressure rise rates that are approximately twice as high as those a conventional SI combustion mode. Consequently the vibration and acoustic emissions were greater in magnitude for the HCCI combustion compared to the conventional SI combustion mode. This finding is important as it validates the investigations of vibration and acoustic sensors for indicating the level of cylinder pressure rise rate in an engine operating under an advanced combustion mode.

Souder et al. [15] used electret condenser microphones and a knock sensor to detect combustion. Souder et al. defined combustion timing in the engine cycle as the engine crank position in crank angle degrees at 50% heat release. Experiments were conducted on a single-cylinder Caterpillar 3401 CI engine operating under HCCI combustion running at a constant speed at light and high loads. The acoustic and vibration data collected from the experiments showed a definite increase in magnitude at

the onset of combustion. Souder et al. then decided to model the acoustic and vibration signals and investigate their usefulness as an engine controller input. By calculating the combustion timing from the cylinder pressure for each engine cycle, it was shown the combustion timing appeared to be a normally distributed process. Therefore, the acoustic and vibration data occurring before combustion was modeled as normally distributed white noise and confidence bounds were set on the pre-combustion data. At the onset of combustion, the acoustic and vibration amplitudes increased dramatically, exceeding the preset confidence intervals, and provided a step signal which could be input into a controller. For medium to high loads, it was shown the vibration and acoustic signals provided a sufficient signal for use in closed-loop engine controllers. Souder et al. did not actually use the acoustic and vibration sensors to control an engine, but rather demonstrated its sufficiency by comparing its behavior to the cylinder pressure. Also, only the entire output of the acoustic and vibration signals were analyzed rather than specific frequency bands. No direct correlation between the acoustic and vibration signals and the cylinder pressure were investigated.

Primarily, investigation of noise emission in internal combustion engines have been focused on CI engines since these engines emit much higher noise levels. However, investigations into understanding the development of knock in SI engines have become more prevalent in recent years. Interestingly, little investigation has been done with regard to a SI engine operating under normal combustion conditions. It is well established that noise emitted from both CI and SI engines undergoing auto-ignition of the fuel-air mixture is related to the rapid pressure rise development in the cylinder. Therefore, externally sensed acoustic and vibration characteristics are indicative of the

rate of cylinder pressure rise or combustion initiated by auto-ignition of the fuel-air mixture.

For the current study, the acoustic and vibration characteristics (being generated by two phenomena: cavity resonances and combustion noise) of SI and CI engines operating under normal combusting conditions are considered to determine under what conditions these characteristics are indicative of rate of cylinder pressure rise amplitudes. This investigation will provide a fundamental study of the vibration and acoustic emission signatures measured from an SI engine operating under normal combusting conditions. The goal is to study the relation between the combustion, represented by the cylinder pressure development and spectra, and noise emitted from the engine. Vibration sensing will provide experimental information describing the response of the engine structure and allude to suspected acoustic emission. Using a single cylinder small displacement engine will eliminate extraneous vibration and acoustic information that are present in multi-cylinder engines. Conversely, vibrations measured from a multi-cylinder CI engine will allow investigation into the robustness of the non-intrusive sensing techniques ability to indicate the cylinder PRR in the presence of extraneous noise. Currently, most studies have performed data reduction using large cycle number averaged data sets as opposed to individual cycle analyses. Cycle-to-cycle comparisons will be conducted to establish any relation between the vibration and acoustic emissions specific to cycle cylinder pressure variations. Once the basic relation between the vibration and acoustic emissions of the engine are understood, further study can be conducted using vibration and acoustic sensing techniques for engine control and diagnostics.

3. EXPERIMENTAL SETUP

3.1 MISSOURI S&T FACILITY AND PROCEDURES

3.1.1 Engine Setup and Control. Vibration and acoustic data were collected from a small, single-cylinder, air-cooled SI engine. The specifications for this engine are given in Table 3.1. Since the engine is a single cylinder engine, the data collected was uninfluenced by excitations that would be present using a multi-cylinder engine platform.

Table 3.1 Single cylinder SI engine specifications

Cylinders	1
Displacement (L)	0.401
Bore (mm)	82
Stroke (mm)	76
Connecting Rod Length (mm)	124
Compression Ratio	8.2
IVO (°ATDC)	-7.1
IVC (°ABDC)	45.1
EVO (°BBDC)	33.4
EVC (°BTDC)	-1

Due to the acoustic sensitivity of the measurements, it was desired to use a dynamometer that gave adequate engine control while maintaining low operation noise. An engine control system from Land & Sea Inc. provided the appropriate solution to the unique problem encountered. The proprietary system included a 9" DYNOmite torid water brake dynamometer, two DYNOmite data acquisition computers, and the DYNOmite DYNOmax Pro engine control software. An automatic load valve and

throttle controller were also acquired to facilitate the automatic load and throttle capabilities of the Land & Sea engine control system.

The water brake dynamometer was mounted to the engine using a custom fabricated coupler and output shaft. The coupler consisted of a 42.54 mm long, 39.85 mm diameter shaft with a 9.53 mm thick, 60.48 mm diameter flange with four equally spaced 5.08 mm diameter bolt holes located a radius of 25.4 mm from the center axis. This shaft was supported by a pillow block bearing mounted to a support block, see Figure 3.1.

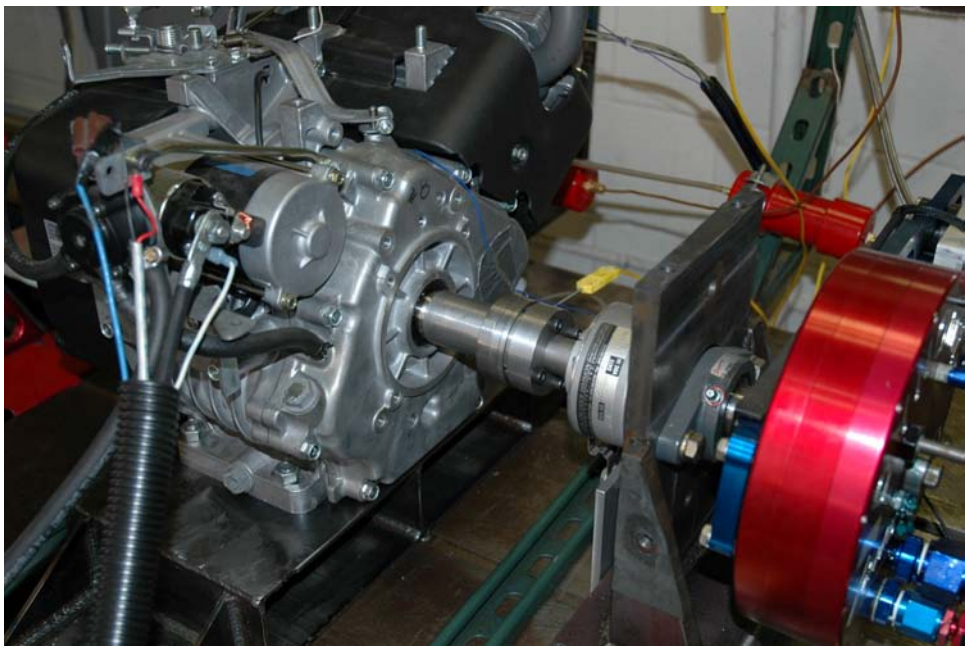

Figure 3.1 Engine/dynamometer coupling system with shaft encoder

The torque arm of the dynamometer was mounted to a 25.4 mm diameter Delrin support shaft, which allowed movement of the torque arm in the axial direction of the

engine crankshaft without inducing bending that would alter any torque readings. The torque arm is designed such that the exact distance between the dynamometer center axis and the support shaft center axis is not needed. The output shaft and torque arm supports are mounted to a common base to provide simple mobility of the dynamometer and support hardware.

Measurements were taken from the DYNOmite dynamometer using two 28-channel DYNOmite data acquisition (DAQ) computers. These proprietary computers were used to read parameters such as: torque, speed, throttle position, and various temperatures. Not only did the DYNOmite DAQ computers read data but also provided the ability to output collected parameters (e.g. torque) via a scaled 0-5 V signal. This signal could then be read by other DAQ systems, resulting in exact time synchronization to other engine events.

All data collected by the DYNOmite data acquisition computers were recorded by a personal computer using DYNOmax Pro software. Automated tests could be developed and implemented by use of the DYNOmax software, DAQ computers, and automatic throttle and load controllers. Automated testing was advantageous because it provided consistent throttle and load combinations between testing.

Power was supplied to the engine starter via a 12 V DC battery. A simple push button starter switch was constructed to facilitate starting the engine from the engine lab. Two engine stop switches were placed in the same box as the starter switch to provide redundancy in ensuring ability to stop engine operation. Another engine stop switch was placed inside the engine test cell to provide a means of stopping engine operation while

in the cell with the engine. A simple wiring diagram of the engine electrical setup is shown in Figure 3.2.

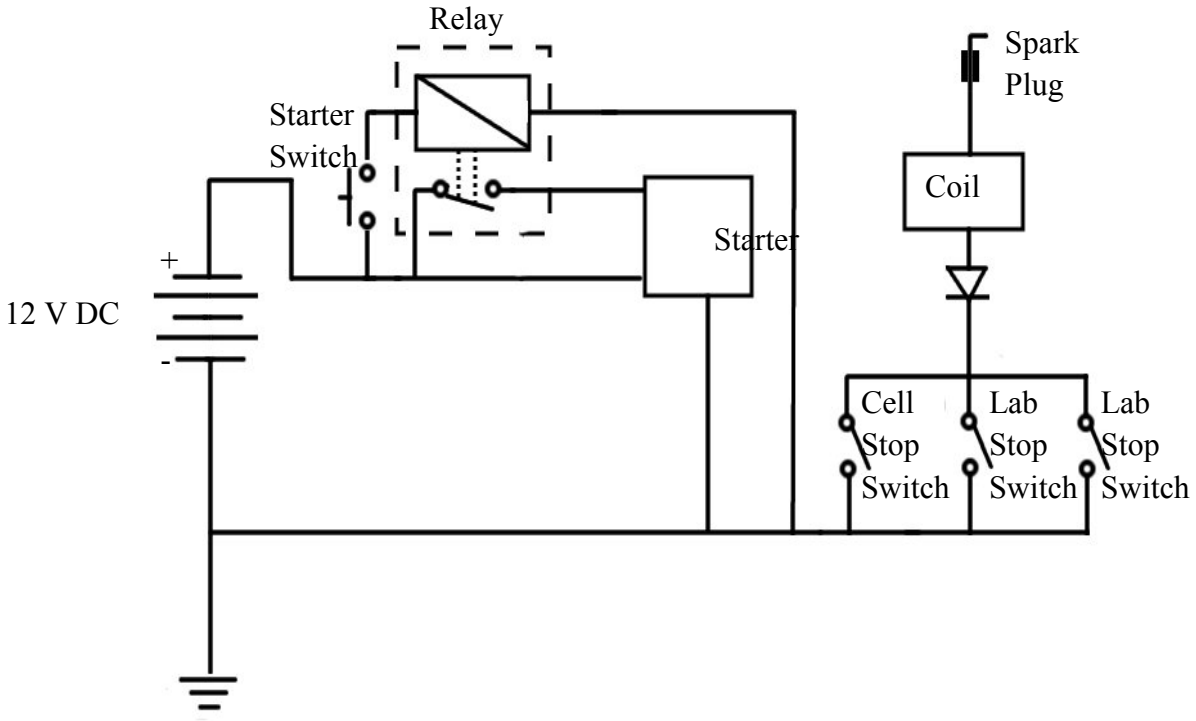

Figure 3.2 Engine run/stop electrical diagram

Fuel was supplied to the engine from a nitrogen gas pressurized fuel tank. Compressed nitrogen gas was delivered through a compressed gas regulator on the nitrogen tank side of the pressure system. An air pressure regulator on the inlet side of the fuel tank was used to maintain a low gas pressure in the tank, equivalent to the pressure provided by the OEM gravity fed gas tank.

3.1.2 In-cylinder Pressure Measurements. In-cylinder pressure measurements were taken using a Kistler 6061B water-cooled pressure transducer. The

use of a water-cooled transducer decreased the amount of measurement drift brought about by the unsteady temperature fluctuations in the cylinder. The pressure transducer was flush mounted into the engine cylinder via a M10x1 tapped hole, see Figure 3.3.

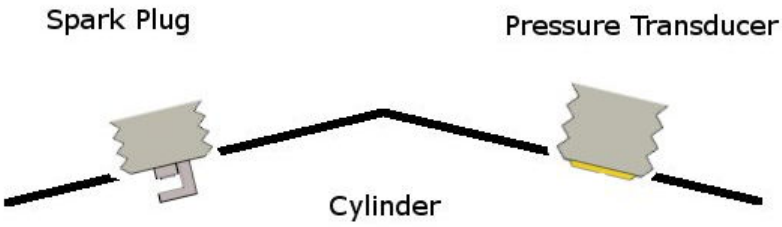

Figure 3.3 In-cylinder pressure transducer mounting location

To gain access to the engine cylinder and provide a path for installation of the pressure transducer, a 19.05 mm hole was drilled through the valve cover, engine head, and into the cylinder. This hole left the oil passages exposed to the engine valves and more importantly the pressure transducer. The engine valves were also exposed to ambient conditions via the hole left in the valve cover. To protect the pressure transducer from oil spatter as well as the inner engine components from ambient conditions, a 19.05 mm outer diameter, 152.40 mm long metal tube was fabricated and installed into the hole. The tube had a wall thickness of 1.27 mm.

Adequate water flow was needed to provide a quasi-static temperature reference to the pressure transducer. This was accomplished using a simple tank filled with distilled water and immersed in a cooling water bath. The distilled water was pumped to the pressure transducer using a small AC pump. The pressure transducer water tank was

designed to have a large amount of surface area which gave adequate heat transfer from the pressure transducer water to the cooling water bath resulting in minimal temperature transients in the distilled water.

Due to the unique installation of the pressure transducer into the engine head (i.e. being installed inside a tube with no air flow), a large amount of heat was trapped in the tube close to the pressure transducer. The OEM pressure transducer water tubes were unable to extract enough heat from the surroundings, and thus the cooling water lines kept expanding and bursting off the pressure transducer water tubes. Two small stainless steel 3 mm outer diameter tubes 152.40 mm long were fabricated to replace the OEM pressure transducer water tubes. Each tube was tapped to a size M3x0.35 on one end to thread into the existing pressure transducer cooling tube locations. These longer tubes allowed the cooling water lines to be exposed to ambient temperature and therefore dissipate enough heat to reduce expansion.

The Kistler 6061B pressure transducer is a charge type transducer and required a charge amplifier/converter for adequate use. A Kistler model 5010 charge amplifier set to 20 MU/Volt was used to convert the sensor charge into a usable voltage. The resulting output voltage was then sent to the data acquisition systems via BNC connections.

3.1.3 Vibration Measurements Subsystem. Accelerometers were used to measure surface vibrations at various locations on the engine. Two types of single-axis accelerometers made by PCB Piezotronics, Inc. were used: “integrated circuit – piezoelectric” (ICP) and charge type. Two miniature ICP accelerometers were used to sense vibrations in locations that didn’t have sufficient room for standard size accelerometers (e.g. behind the flywheel). These accelerometers were flush mounted to

the engine surface using a high temperature adhesive. A PCB model 352B10 was mounted behind the flywheel to sense vibrations induced by the axial crankshaft movement, see Figure 3.4. The other ICP accelerometer, a PCB model 320C17, was purchased with a mounting stud to provide a more robust mounting for areas of the engine where the conditions are extremely harsh (i.e. around the engine head). The 320C17 was mounted in the oil passage against the lower cylinder wall (this accelerometer location will be designated LCW), see Figure 3.5. This location was chosen due to being normal to the piston skirt when the piston is at top-dead-center (TDC).

Figure 3.4 Flywheel accelerometer mounting location

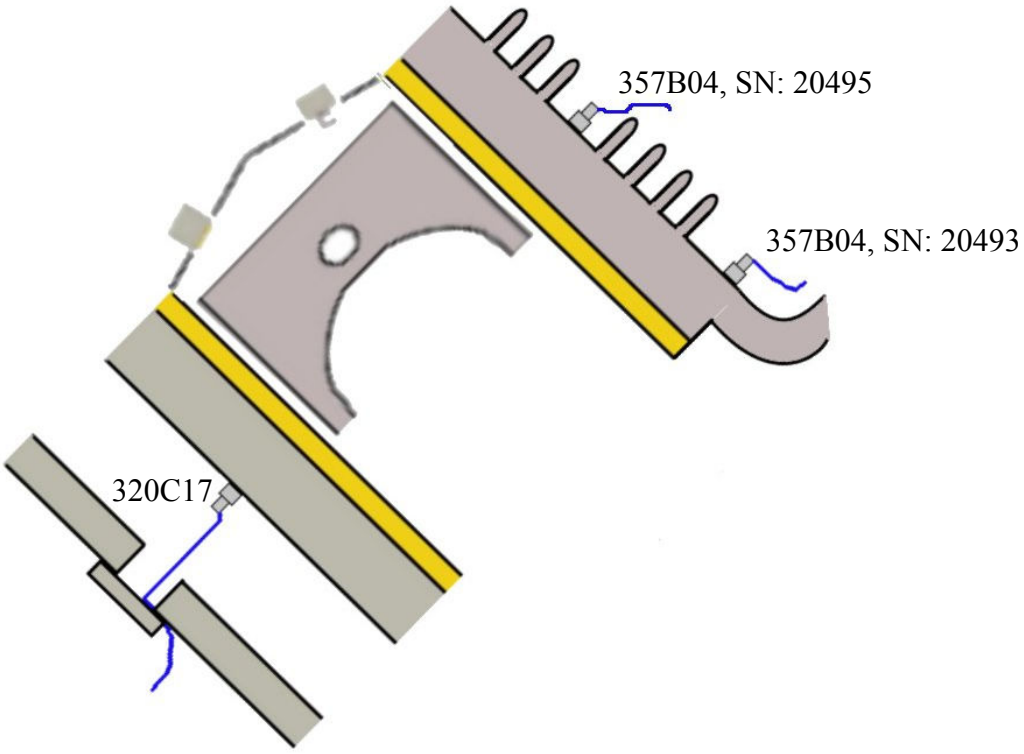

Figure 3.5 Cylinder wall accelerometer mounting locations

The miniature ICP accelerometers provide acceleration sensing in small enclosures but were limited to the range of temperature they could handle. To facilitate acceleration sensing for higher temperature surfaces, such as the cylinder walls, PCB 357B04 charge type accelerometers were selected. These accelerometers could handle higher temperatures than the miniature ICP accelerometers. One PCB 357B04 accelerometer was mounted on the upper cylinder wall (this accelerometer location will be designated UCW) normal to the piston skirt at TDC using a 10-32 thread mounting stud. Another PCB 357B04 accelerometer was mounted on the same cylinder wall but much closer to the crankcase (this accelerometer location will be designated BCW). This location was chosen to investigate cylinder wall vibrations when the piston was at

bottom-dead-center (BDC). The mounting locations can be seen in Figure 3.5. The output specifications for the PCB accelerometers can be found in Appendix A.

The output of the miniature ICP accelerometers was a very low level voltage; therefore, a PCB 483B03 12-channel rack-mount inline signal conditioner was used to amplify the signal to a usable voltage. This voltage was then sent via BNC connections to the data acquisition system.

Two methods were used to convert the charge signal output by the 357B04 accelerometers to a usable voltage. The UCW accelerometer was connected to a Kistler 5010 charge amplifier set to 200 MU/Volt. The BCW accelerometer was sent to an in-line charge converter which converted the charge from pC to volts. The signal was then sent from the in-line converter to the PCB 483B03 signal conditioner. Finally, the signal was sent via BNC connections from the signal conditioning hardware to the data acquisition system.

3.1.4 Acoustical Measurements Subsystem. The engine test cell is an extremely acoustically harsh environment. Large acoustic reverberations are present due to the close proximity of the engine to the engine lab walls and ceiling. Reverberation is the physical phenomenon attributed to acoustic waves propagating outward from a source and then being reflected from a surface back toward the source. If the source is constantly supplying acoustic power, such as a running engine, the reverberations will increase and the reflected acoustic waves will mask any new acoustic energy output from the source.

Secondly, the parallel geometry and rigidity of the surrounding walls and ceiling create yet another acoustic phenomenon: standing waves. Standing waves are created

when two acoustic waves of the same frequency are travelling in opposite directions, low amplitude acoustic pressure wave nodes are created in the room. If the microphone is placed at one such node, there will be no acoustic energy recorded for this frequency.

To decrease the reverberation and standing wave phenomenon of the engine lab, low cost acoustic absorbing material panels were created to alter propagation paths of the acoustic waves. These panels were hung between the engine and the surrounding walls and ceiling to decrease any immediate reverberations, see Figure 3.6.

Figure 3.6 Acoustic absorbing panels installed in the engine test cell

A RODE NT3 microphone was selected for acoustic measurements. This microphone was advantageous due to its sensitivity to direction. This was preferred for the engine lab to reject any acoustic pressure waves propagating behind the microphone and only detect acoustic waves coming from the source. To maintain consistency in the

acoustic data collected from the engine, the microphone had to maintain a consistent mounting location. The microphone location was selected by moving the microphone to different locations until combustion noise was most noticeably detected. A microphone boom was used to hold the microphone in place. To decrease the amount of extraneous noise imposed on the acoustic measurements, it was required to mount the microphone in a location that was out of any incoming or outgoing air stream of the engine.

The RODE NT3 microphone uses a very thin diaphragm to detect very low amplitude pressure perturbations. In order for the acoustic output of this microphone to be useful, it needed to be amplified before it was sent to the data acquisition system. A SMPro Audio PR4V four channel microphone preamp was used to amplify the incoming microphone signal to a usable level for data acquisition. The PR4V used an XLR cable to connect to the microphone. Another advantage to using this preamp is that it supplied the 48 volt phantom power required by the microphone. Once the signal had been amplified, it was sent to the data acquisition system via standard ¼" straight instrument cables. A listing of the input channels is given in Table 3.2.

Table 3.2 Audiofire input channels

Channel	Signal
1	TDC
2	Microphone
3	LCW Accelerometer
4	UCW Accelerometer
5	Pressure
6	Crank Angle
7	Flywheel Accelerometer
8	Pulse
9	BCW Accelerometer

3.1.5 Data Acquisition System. It is common for data acquisition of an internal combustion engine to be timed using a crank-angle resolved hardware time clock. Although advantageous for engine analysis, this type of data acquisition is not sufficient for vibration and acoustic signals. First, because the response of the human ear is between 20 and 20,000 Hz, it is required to collect data at a minimum of 40,000 Hz to account for the Nyquist frequency, properly reconstruct the signal, and obtain usable spectral information. Secondly, crank-angle resolved data acquisition results in signal samples that are not evenly spaced in time. This does not appear to affect the time series waveform with regard to reconstruction, but the spectral content is affected tremendously. A 100 Hz sine wave was sampled with uniform time intervals and then non-uniform time intervals, Figure 3.7.

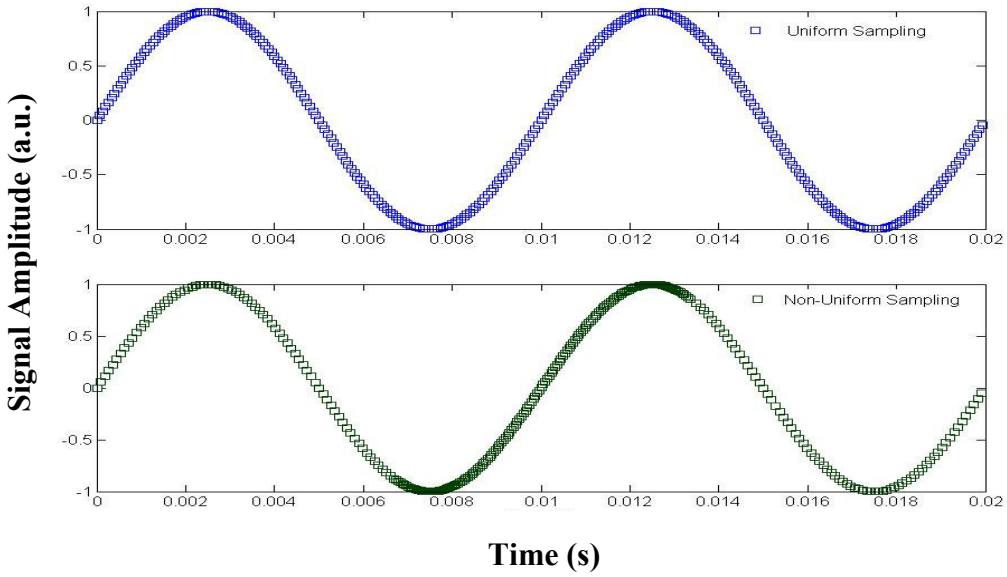

Figure 3.7 Time signature comparison of the uniformly and non-uniformly sampled data

It is clear that, in time, the signal appears to be represented well by both types of sampling schemes. However, the spectral content, shown in Figure 3.8, shows there is a large difference in the spectral content represented by the two different sampling schemes. Therefore, to obtain accurate spectral content, the vibration and acoustic data was to be sampled with uniformly spaced time intervals.

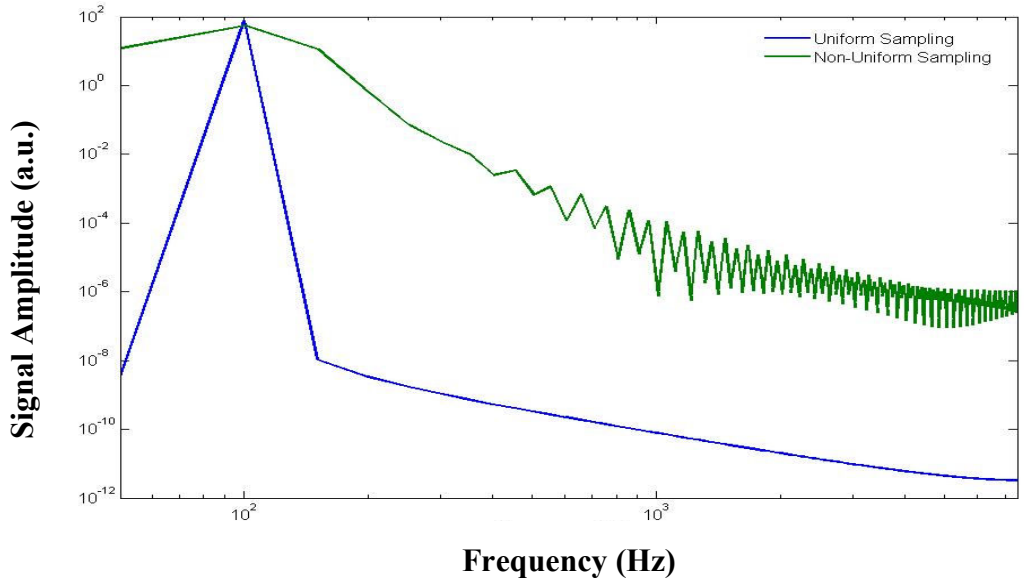

Figure 3.8 Frequency content comparison of the uniformly and non-uniformly sampled data

To accommodate uniformly spaced time resolved data acquisition, an Echo Audiofire12 audio recording rack was selected. The Audiofire12 allows for up to 12 balanced inputs that can all simultaneously be sampled at a maximum of 192,000 Hz. Also, the Audiofire interfaces with a personal computer via a FireWire (IEEE 1394a) interface resulting in very fast data transfer of up to 400 megabytes-per-second (Mbps).

To collect and store the data in the computer, Adobe Audition audio recording and analysis software was used. The Audiofire12 drivers were compatible with the Adobe software and thus Audition could be used to collect up to 12 channels of data at a desired sampling rate without any extra programming needed.

Uniformly spaced time resolved data acquisition provides accurate spectral content and is preferred for vibration and acoustic data acquisition. However, it is not an optimized data collection method for internal combustion engine data. A better approach to collecting engine data is to hardware time the data acquisition system i.e. sample every crank-angle-degree (CAD). First, this type of data acquisition provides the same number of samples per engine cycle regardless of engine speed. This is advantageous for comparing events occurring during an engine cycle and decouples the data from influences, such as acceleration or deceleration of the engine, causing instantaneous changes in engine speed during a cycle. Secondly, higher rates of data acquisition can result in large amounts of unwanted data. By sampling at a one CAD resolution, smaller amounts of data are collected.

Hardware timed data collection was conducted using a BEI optical shaft encoder as the clock signal. The shaft encoder output one pulse per CAD as well as one pulse per revolution which was used for a top dead center reference. The encoder signals were input into a Cosworth engine controller which served as a signal conditioner. The Cosworth engine controller converted the raw CAD and TDC pulses into TTL pulse signals suitable for use by the data acquisition system.

The conditioned CAD and TDC pulses were connected to a National Instruments (NI) BNC-2090 rack mounted BNC terminal block. This terminal block served as the

external interface for the CAD resolution data acquisition system. The terminal block was connected to a NI PCI-6259 data acquisition card. To collect and save the data, a data collection program was written in NI LabVIEW. Table 3.3 shows the signals collected to each channel for this study.

Table 3.3 Crank-angle resolved channel inputs

Channel	Signal
1	Crank Angle
2	Pressure
3	--
4	Torque
5	Pulse
6	Spark
7	--

For the current study, both uniformly spaced time clocked data and non-uniformly spaced CAD clocked data collection was desired. This would provide an optimized data acquisition system for vibration, acoustic and engine data. However, it was realized that the different acquisition rates of the two clocked systems would result in a different number of samples per cycle. A method by which to synchronize the time clocked data with the CAD clocked data needed to be developed. Therefore, a small step signal box was constructed.

The step signal box consisted of two AA batteries wired in series such that the effective voltage supplied was approximately 3 V. The step input was controlled via simple on/off switch. A LED was also installed to provide verification that, when switched on, the step signal was operational. The signal was output through a voltage

divider into two BNC output terminals. One BNC terminal as connected to an input channel on the Audiofire recording rack and the other was connected to the NI DAQ system. Due to the 1V input limitations of the Echo Audiofire recording rack, a voltage divider circuit, see Figure 3.9, was designed to output a ~0.35V step signal from the box.

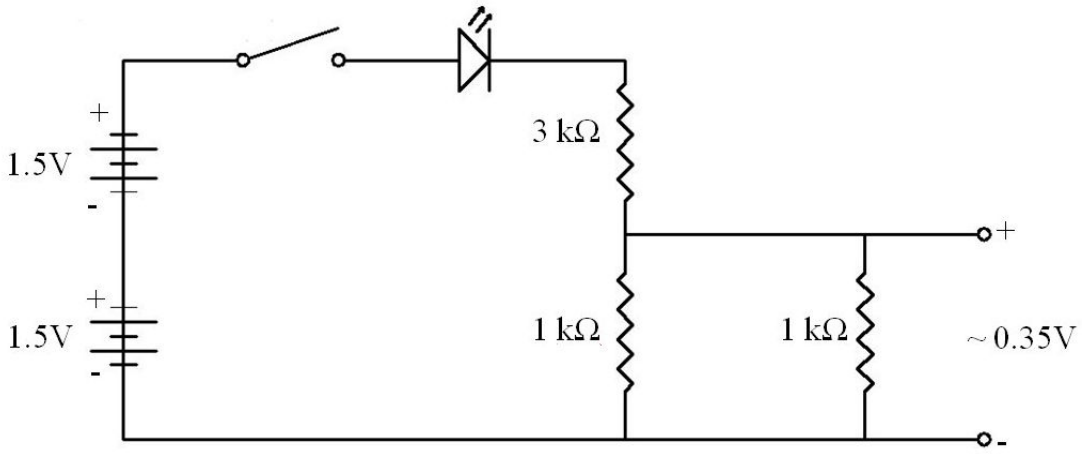

Figure 3.9 Wiring diagram of the step signal generator

When the signal was switched on, an output step voltage was supplied to the time and CAD clocked data acquisition systems. This step, since it was recorded by the two data acquisition systems at the same instance in time (i.e. during the same engine cycle), provided a common reference in each data set to effectively synchronize each engine cycle in the time and CAD clocked data.

3.2 NTRC FACILITY AND PROCEDURES

3.2.1 Research Engine and Support Systems. Data was collected in conjunction with the Fuels, Engines, and Emissions Research Group (FEERG) at the

National Transportation and Research Center (NTRC). The engine used for data collection was a Mercedes 1.7L common-rail direct injection (CDI) compression ignition engine. The engine specifications are listed in the Table 3.4. This engine was controlled via a Midwest induction dynamometer and personal computers running proprietary software.

Table 3.4 Mercedes 1.7L engine specifications

Cylinders	4
Displacement (L)	1.689
Bore (mm)	80
Stroke (mm)	84
Connecting Rod Length (mm)	140
Compression Ratio	19
IVO (°ATDC)	23-24
IVC (°ABDC)	7
EVO (°BBDC)	3-4
EVC (°BTDC)	22

Pressure sensing was available for all four cylinders using Kistler model 6053 non-cooled cylinder pressure sensors mounted using Kistler glow-plug adapters. Although in-cylinder pressure data for each cylinder was available, data was collected from cylinder 1 only since this was the cylinder to which the knock sensor was mounted closest to. The in-cylinder pressure sensors were connected to Kistler 5010 charge amplifiers before the signals were acquired by the data acquisition system.

Engine block surface vibrations were detected using a Lamerholm Fleming model VP50/1 knock sensor. The VP50/1 knock sensor is a piezoelectric accelerometer specifically designed for knock sensing in automotive applications. The raw knock sensor

data was unconditioned and connected directly to the data acquisition system. The sensitivity specifications for this accelerometer can be found in Appendix A.

3.2.2 Time Resolved Data Acquisition. Time clocked data acquisition was done using an IOtech Wavebook ethernet-based Portable high-speed waveform acquisition system. The Wavebook had eight built-in DAQ channels with a sampling rate of 1 MHz. For the current study, five channels of data, shown in Table 3.5, were collected at 200 kHz each. The data acquisition rate was chosen to provide adequate sample resolution for reconstruction of the short CAD pulse and Z-Pulse signals. Data was collected using the IOtech WaveView software on a Dell notebook computer.

Table 3.5 IOtech channel inputs

Channel	Signal
1	Z-Pulse
2	Injector
3	Crank Angle
4	Pressure
5	Knock

3.2.3 Crank Angle Resolved Data Acquisition. Crank-angle-degree resolved data was acquired using an AVL IndiModul 621 coupled to a shaft encoder. The shaft encoder output a pulse signal every 1/5 CAD. Along with the CAD pulse, the shaft encoder output a pulse signal (Z-pulse) once every resolution. The Z-pulse was set to start trigger the AVL data acquisition system at -63 CAD ATDC and provided a common signal to synchronize the time and CAD clocked data. Data was collected using proprietary software developed specifically for the FEERG.

4. DATA COLLECTION AND ANALYSIS PROCEDURES

4.1 DATA COLLECTION PROCEDURES

Before discussing the data collection procedures, it is necessary to briefly discuss the types of signals collected, the desired information to be extracted, and the impact these considerations had on data collection.

In order to characterize combustion noise and cavity resonances, the frequency content of the acoustic and vibration signals were investigated. Vibration and acoustic signals are composed of energy waves that propagate in an oscillating manner that can be modeled as a sinusoidal function of time. Obviously, this time dependant oscillating signal can have a varying wavelength and, consequently, a varying frequency. Vibration and acoustic energy waves can be composed of a single oscillating wave or a superposition of many oscillating waves. Therefore, vibration and acoustic energy waves can be composed of a single frequency energy wave (a pure tone) or an energy wave composed of multiple frequencies. Analysis of the frequency content of a signal is important in understanding the energy composition and determining source of a signal.

The number of samples in the discrete time signal waveform and the signal sampling rate has a direct effect on the frequency resolution of the transformed signal. For example, 100 samples of a signal collected at a sampling rate of 8000 Hz will have a frequency resolution (Δf) of 80 Hz. The relationship used in MATLAB to derive the frequency resolution is:

$$\text{frequency resolution} = \Delta f = \frac{1}{\text{number of samples}} \times \text{sampling rate} \qquad (4.1)$$

or using the values from the previous example:

$$\Delta f = \frac{1}{100 \text{ samples}} \times 8000 \frac{\text{samples}}{\text{sec}} = 80 \text{ Hz} \ . \tag{4.2}$$

It is important to collect enough samples during an engine cycle to provide adequate frequency resolution and avoid aliasing when reconstructing the frequency spectrum. Considering sample length along with the need to collect data at a rate sufficient to account for the Nyquist frequency, the sampling rate for the time resolved data collection conducted at Missouri S&T was 88,200 Hz. Data was collected for at least one minute or 1000 engine cycles, which ever was temporally longer. Data collected at the NTRC for the diesel (CI) engine investigation was collected at 200 kHz for 5 engine cycles. For the SI engine, the engine operating set point test matrix is shown in Table 4.1.

Table 4.1 Test matrix for SI experiments

Set Point	Speed (rpm)	Load (N-m)
1	1500	4.1
2	1500	13.6
3	2520	4.1
4	2520	13.6
5	2520	27.1
6	3000	4.1
7	3000	13.6
8	3000	27.1

This text matrix was designed to examine low, medium, and high speed and load conditions. The CI engine was operated at a single speed and load of 1500 rpm and 37.3 N-m, respectively.

4.2 PRESSURE ANALYSIS

4.2.1 Average Pressure Rise Rate. It was desired to represent the cylinder pressure rise rate (PRR) as an indicator of the energy release rate of the combustion process. In a spark-ignition (SI) engine, the rapid release of energy at the onset of combustion results in a near linear cylinder pressure increase from start-of-combustion (SOC) to the resulting peak cylinder pressure, especially when an engine is operated at high load. Therefore, the slope of this near linear increase was chosen as a metric by which to quantify the pressure rise rate and as an indicator of the energy release rate of the combustion process. This slope will be referred to as the average pressure rise rate. A least-squares linear regression from SOC (time of spark) to the resulting peak cylinder pressure was conducted to determine the slope representing the average PRR, see Figure 4.1

A proprietary program utilizing the `polyfit` function in MATLAB was written to implement the least squares regression analysis on each engine cycle. From the `polyfit` function, a first order coefficient representing the slope of the linear fit (e.g. 140 kPa/deg in the equation shown in Figure 4.1) was determined. The slope represented a time averaged PRR value rather than an instantaneous peak PRR value generally determined from the first derivative of the cylinder pressure.

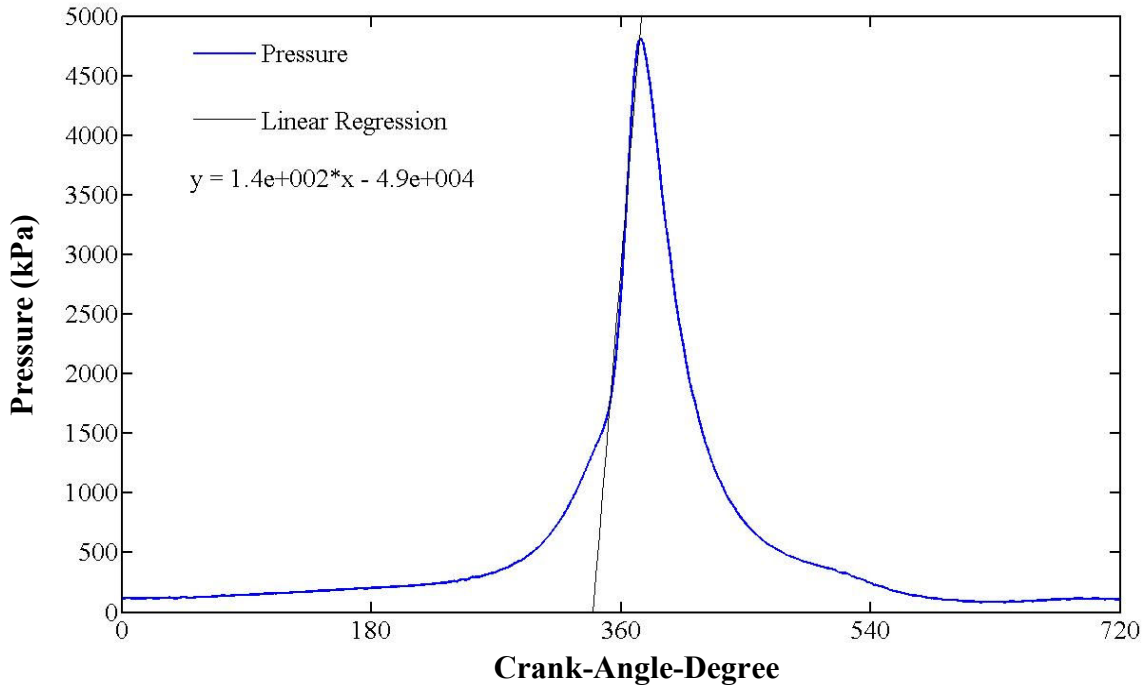

Figure 4.1 Linear regression for one engine cycle (2520 rpm, 27.1 N-m)

4.2.2 Instantaneous Pressure Rise Rate. To investigate the relation of the peak instantaneous PRR to emitted acoustic or vibration energy, the first derivative of the pressure signal was calculated. Numerical differentiation of the acquired pressure signals was conducted on a per-engine-cycle basis using a central difference method:

$$\frac{dP_i}{d\theta} = \frac{P_{i+1} - P_{i-1}}{2h}. \qquad (4.3)$$

P represents the discrete pressure signal and h represents the change in crank-angle-degree (CAD) between two pressure values. Numerical differentiation was implemented on the hardware timed signal, therefore h = 1 CAD. Selection of the peak instantaneous pressure rise rate value was conducted by windowing the pressure derivative from 340 – 450 CAD (effectively windowing combustion), and determining the peak pressure derivative value, see Figure 4.2.

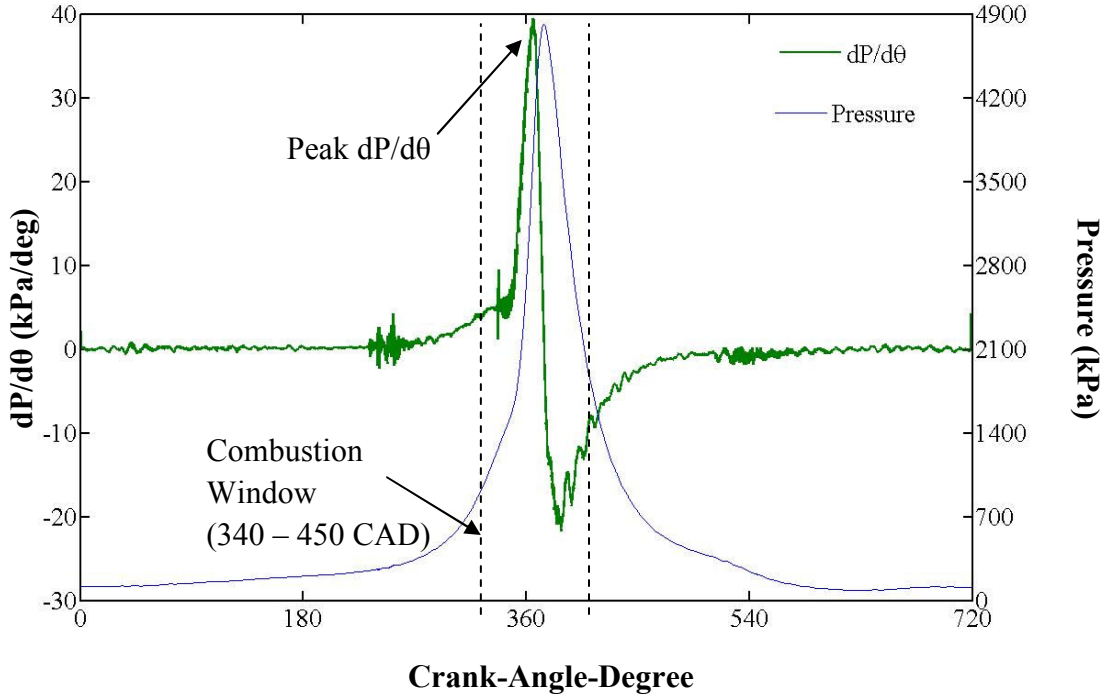

Figure 4.2 First derivative of in-cylinder pressure. The pressure trace has been added to show occurrence in cycle (1 cycle, 2520 rpm, 27.1 N-m)

4.3 SPECTRAL ANALYSIS

4.3.1 Frequency Spectrum Analysis. To extract frequency content from experimentally collected discrete time signals, a discrete Fourier transform (DFT) was performed using the MATLAB `fft` function on the signal. The algorithm used by the `fft` function to compute the DFT of a discrete signal is:

$$X(k) = \sum_{j=1}^{N} x(j) e^{-2\pi i (j-1)(k-1)/N}. \qquad (4.4)$$

X(k) is the transformed signal vector (also known as the spectral density), x(j) is the discrete time signal vector, N is the number of samples in the discrete signal vector, k is the transformed discrete signal sample number, j is the discrete time signal sample

number, and i is an imaginary number. Since k is an integer, the DFT algorithm will output complex values at integer multiples of the signal's frequency resolution. In order to eliminate the complex numbers and provide a real number useful for spectral energy representation, the power spectrum was calculated using the following expression:

$$S(\omega) = \lim_{T\to\infty} \frac{1}{T} |X|^2, \tag{4.5}$$

The number of samples for each cycle, N, was substituted for the time period T and $|X|^2$ was calculated using the expression:

$$|X|^2 = (XX^*) = Re(X)^2 + Im(X)^2, \tag{4.6}$$

(* denotes the complex conjugate).

The result is the power spectrum of the transformed signal or:

$$S(\omega) = \frac{XX^*}{N}, \tag{4.7}$$

with units equivalent to the original signal's units. To give an example, the lower cylinder wall (LCW) accelerometer's time series waveform for one engine cycle is shown in Figure 4.3. Its corresponding frequency content is shown in the frequency spectrum in Figure 4.4. Note the peaks occurring between approximately 1500 – 2100 and 6500 – 8200 Hz, exposing vibration energy increases in these frequency bands not apparent from the time signal waveform in Figure 4.3. This example illustrates the importance of the Fourier transform and the frequency spectrum for determining a signal's energy wave frequencies.

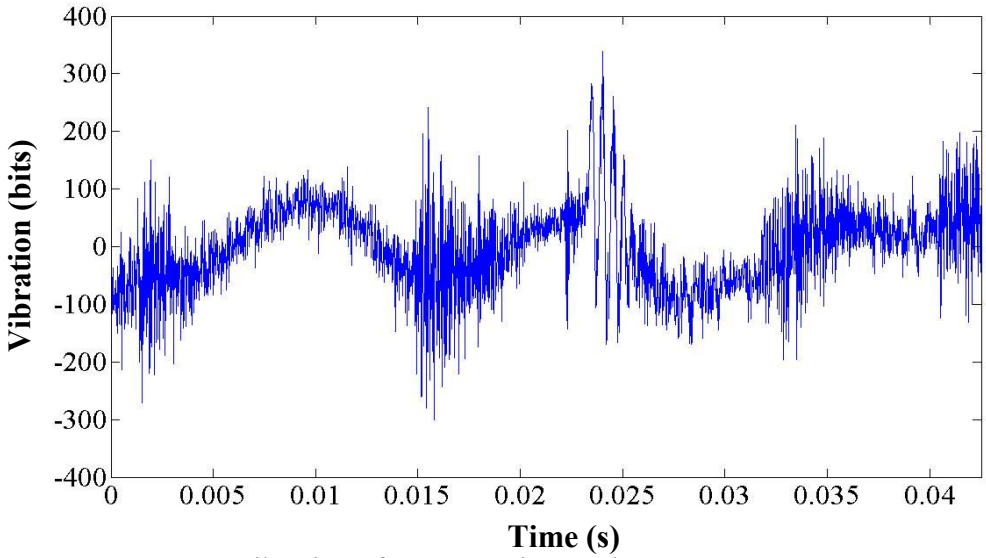

Figure 4.3 LCW vibrations for one engine cycle

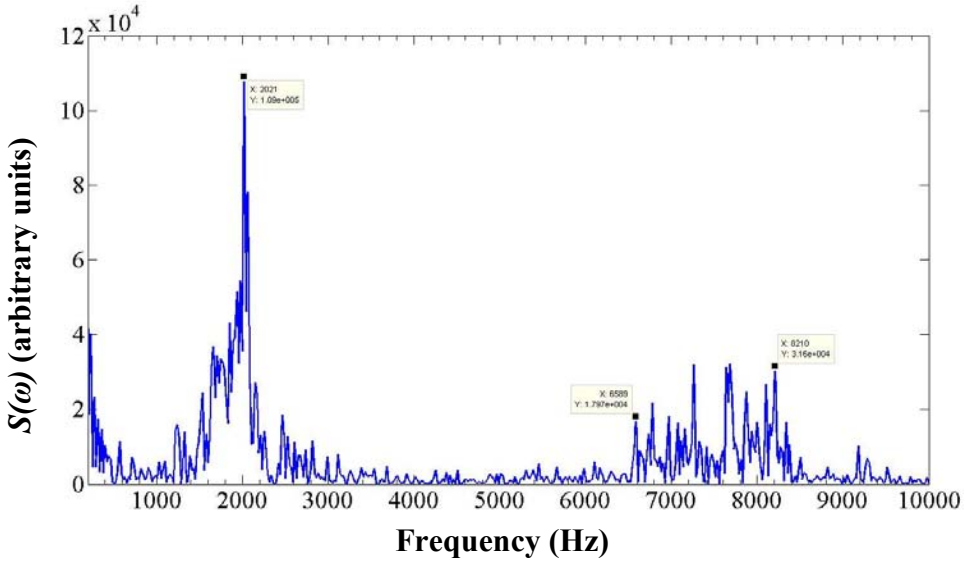

Figure 4.4 Frequency content of the LCW vibration for one engine cycle (2520 rpm, 27.1 N-m)

4.3.2 Joint Time-Frequency Analysis. A frequency spectrum is an invaluable tool for performing frequency content analysis, however it can be quickly noted the

temporal description of the energy increases is completely lost. Consequently, this is a major downfall of using only the Fourier transform of a signal to analyze frequency content. In an effort to preserve time signal events and gain the frequency content analysis, a joint TF analysis technique was implemented. Joint TF analysis is important in this study since vibration and acoustic events are random events that are repeated every engine cycle.

In particular for this study, the STFT time-frequency analysis method was chosen to extract the frequency content of a signal while preserving the time signal events. The STFT algorithm windows a small segment of the time series waveform and implements a DFT on the data contained in the window. The window is stepped through the time signal until the entire waveform is analyzed. The result is a set of data representing the signal's energy signature in frequency and time, see Figure 4.5. One drawback to using this method is the tradeoff between time and frequency resolutions. Increasing the time segment will increase the frequency resolution and decrease the time resolution and vise versa. For the analysis shown in the following TF plots, due to a the sampling rate of 88200 and the chosen time window segment of 300 samples, the time resolution was approximately 26 CAD and the frequency resolution was 300 Hz.

The bottom blue plot in Figure 4.5 is one engine cycle of the lower cylinder wall (LCW) accelerometer's time series waveform. The left red plot is the corresponding frequency content (or Fourier transform) of the blue time series waveform. This plot is Figure 4.4 rotated 90° counter-clockwise. The large center contour plot is the corresponding STFT. The energy increases in the 1500 – 2100 and 6500 – 8200 Hz frequency bands can clearly be seen in the STFT plot. Additionally, by use of the STFT,

the temporal occurrences of these events can be determined, thus illustrating the value of the STFT.

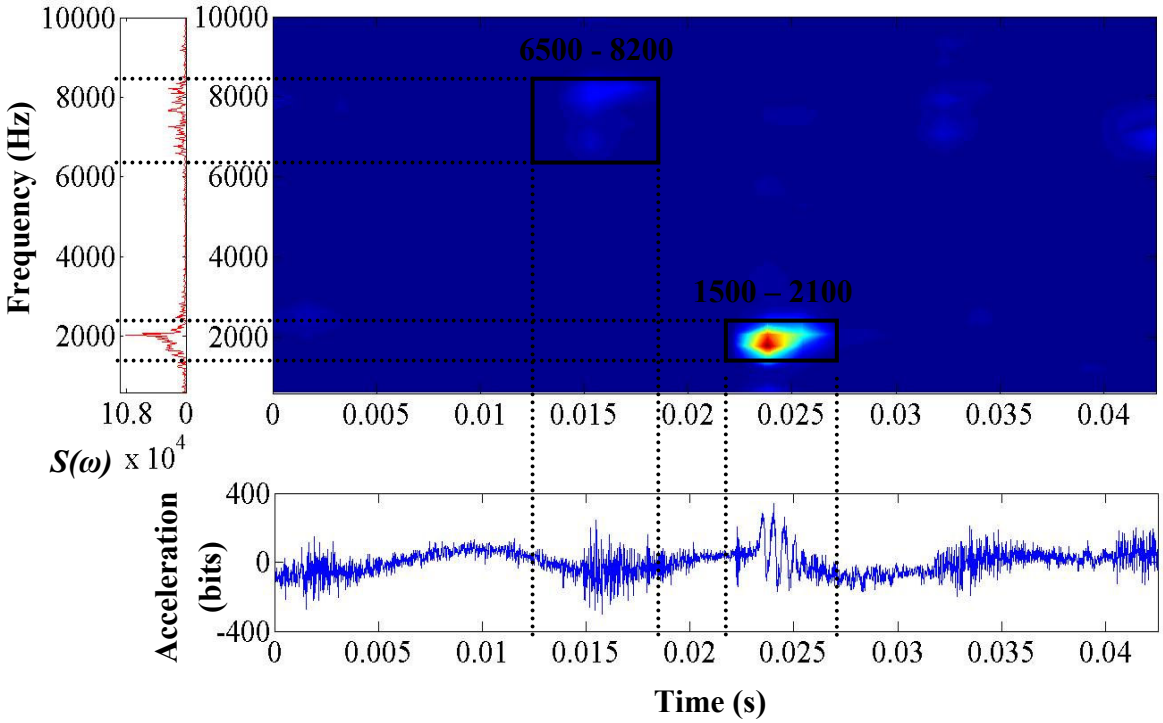

Figure 4.5 STFT of the LCW vibration for one engine cycle (2520 rpm, 27.1 N-m)

4.4 ESTABLISHING CHARACTERISTIC FREQUENCY BANDS

In order to determine possible correlations between acoustic and vibration energy and cylinder PRR, metrics were established for the acoustic and vibration energy. More specifically, certain frequency bands were selected to represent combustion noise and cavity resonances. The following sections will discuss the selection of these frequency bands.

4.4.1 Cavity Resonant Frequency Bands. As was explained by Naber et al. [16], the cavity resonant frequency modes of the engine can be estimated by the solution

of the wave equation on a disk. The equation describing the frequency modes is:

$$f = C\frac{\rho(m,n)}{\pi B}, \tag{4.8}$$

where f is the frequency, C is the speed of sound in the gas, and B is the cylinder bore. $\rho(m,n)$ is a constant representing the vibration mode factor. A brief discourse with regard to the cylindrical wave equation applied to a disk will further explain its origin.

At the onset of combustion, when the piston is at nearly top-dead-center, the bulk gas can be modeled as a circular disk. The wave equation on a disk expressed in cylindrical coordinates has the form:

$$\frac{d^2P}{dr^2} + \frac{1}{r}\frac{dP}{dr} + \left(k^2 - \frac{m^2}{r^2}\right)P = 0 \tag{4.9}$$

where P is the pressure amplitude, k is the wave number, r is the radius and m is the circumferential mode number. The solution of Equation 4.9 is of the form:

$$P = AJ_m(kr)\ . \tag{4.10}$$

A is a constant, and J_m is Bessel's function of the 1st kind. The roots of the first derivative of J_m will give the possible periods of vibration. Kinsler et al. [17] gives the values of $\rho(m,n)$ that would satisfy $J'_m(\rho(m,n)) = 0$, shown in Table 4.2, as:

Table 4.2 Extrema of Bessel Functions of the first kind, $J'_m(\rho(m,n)) = 0$

	ρ(m,n)	
n / **m**	**1**	**2**
0	0	3.83
1	1.84	5.33
2	3.05	6.71

Therefore, $\rho(m,n)$ is a constant from Table 4.2 representing the extrema of Bessel functions of the first kind, where m represents the circumferential mode number and n represents the radial mode number.

To determine the cavity resonance frequencies, assumptions had to be made with regard to the bulk gas conditions during combustion since this information could not be measured in the cylinder. The properties of the bulk gas and the speed of sound were calculated at a temperature of 2000 K. Kinsler et al. [17] gives an expression for the speed of sound in a perfect gas when scaled to the speed of sound in the gas at a temperature of 273K as:

$$C = C_0 \sqrt{T_K / 273}\,. \tag{4.11}$$

Gasoline has an air to fuel ratio (A/F) of approximately 14, which means there is approximately 14 times the amount of air than gas in the mixture. Therefore, the speed of sound in air was used to predict the cavity resonance frequencies for the engine cylinder. Taking the speed of sound in air at 273K to be 332 m/s, the speed of sound used in the cavity resonant frequencies approximation was:

$$C = 332 \sqrt{2000 / 273} \approx 900 m/s \tag{4.12}$$

Inserting the bore for the small-single cylinder spark ignition engine (B = 82 mm), speed of sound in air (C = 900 m/s), and the values found in Table 4.3 into Equation 4.8 yields the predicted cavity resonant frequencies in Table 4.3.

Since compression ignition engines generally operate under increased in-cylinder pressures (this is required to achieve combustion), the assumed bulk gas temperature was

Table 4.3 Cavity resonant frequencies for the small single-cylinder SI engine

	***f* (kHz)**	
n / ***m***	**1**	**2**
0	0	13.4
1	6.4	18.6
2	10.7	23.4

2500 K. The cavity resonance frequencies can be modeled as was done in the SI engine. The speed of sound in air calculated for the higher temperature is:

$$C = 332\sqrt{2500/273} \approx 1000 m/s \tag{4.13}$$

The bore of the Mercedes 1.7 L engine used in the diesel engine investigation was 80 mm and, thus, the cavity resonant frequencies, given in Table 4.4, of this engine were:

Table 4.4 Cavity resonant frequencies for the CI engine

	***f* (kHz)**	
n / ***m***	**1**	**2**
0	0.0	15.2
1	7.3	21.2
2	12.1	26.7

The cavity resonant frequency values presented in Table 4.3 and Table 4.4 are only estimated values and certain characteristics of the combustion process in a reciprocating engine should be noted. It is assumed the bulk gas is at a constant pressure and temperature. This is not the case in a firing engine cylinder where the volume is

changing due to the piston travel and thus expansion of the bulk gas creates decreases in gas temperature and pressure. Also, the bulk gas being modeled as air is a weak assumption and including the gas properties of the fuel would provide a better cavity resonant prediction. While improvements could be made to current cavity resonant frequency estimates, they provide a reasonable value with which to begin analysis.

For this investigation an arbitrarily chosen frequency bandwidth of 6 – 6.6 kHz was selected as the frequency band characterizing cavity resonance in the SI engine. This bandwidth would encompass the first circumferential mode which, from previous literature [14], was suspected to be the prominent frequency mode resulting from cavity excitation. Results presented in this document with regard to the CI engine will focus only on the first cavity resonant mode. The research conducted on the CI engine was performed during a 10 week research fellowship at the National Transportation and Research Center (NTRC). Therefore time and facilities did not permit investigation with regard to acoustic energy emission of the CI engine. A frequency bandwidth of 5000 – 8000 Hz was selected to characterize the cavity resonance of the CI engine. Investigation into the frequency spectrum of the in-cylinder pressure showed this bandwidth contained a burst of energy, see Figure 4.6, which encompassed the theoretical first circumferential mode of 7.3 kHz given in Table 4.4. The metric used for comparison in this investigation was an RMS value of the energy contained in the specified SI and CI cavity resonant frequency bands.

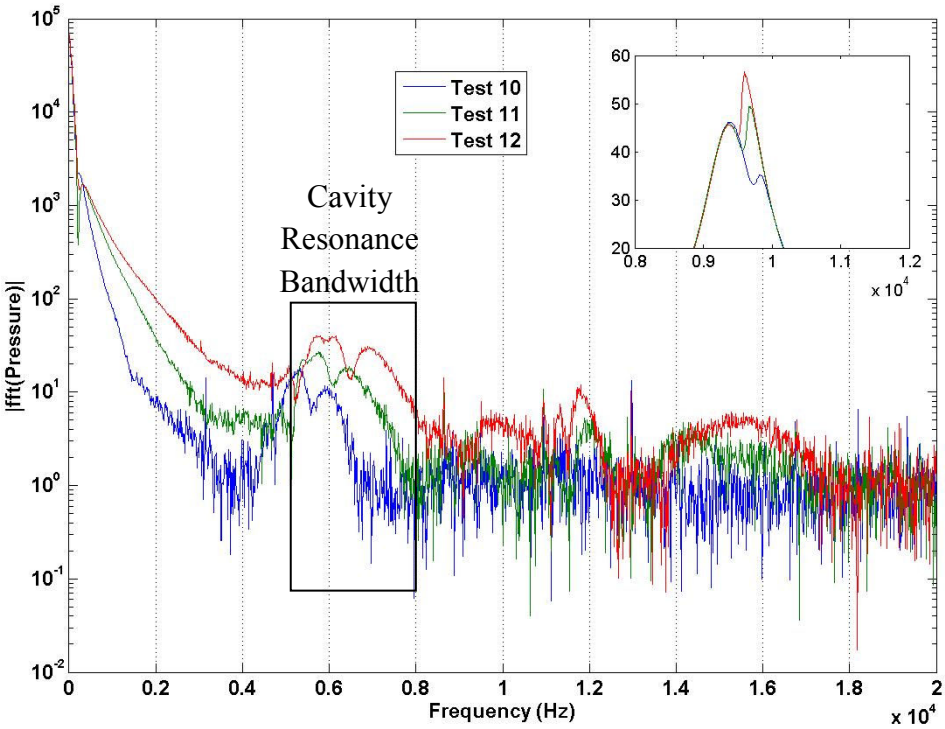

Figure 4.6 Comparison of the frequency content for three different injection timing conditions used in the CI investigation, the original pressure traces are shown in the inset

4.4.2 Combustion Frequency Bands for the SI Engine. Acoustic Frequency: To determine the characteristic frequencies in the acoustic energy emitted from the engine as a result of combustion, a 10 cycle average of low and high average PRR cycles and the corresponding acoustic data are presented in Figure 4.7. Both sets of data are from the small single cylinder engine at a set point of 2520 rpm, 27.1 N-m, a full load condition. This condition was selected due the engine's increased acoustic output.

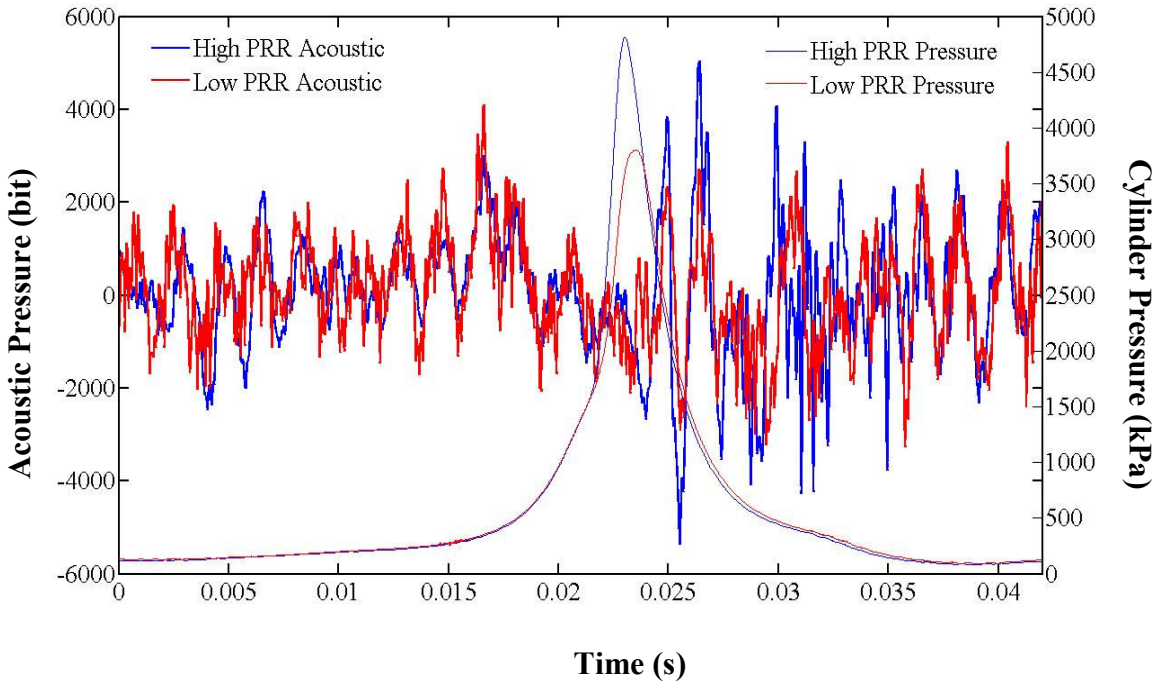

Figure 4.7 A 10 cycle average of the acoustic energy emitted from the SI engine for low and high PRR cycles with the corresponding 10 cycle average pressure signals added to identify cycle timing (2520 rpm, 27.1 N-m)

Pressure is shown on the plot to identify the occurrence of specific acoustic events with respect to cycle time, however the acoustic signal is delayed a few milliseconds from the in-cylinder pressure signal due to travel time of the acoustic pressure waves. Notice the acoustic time waveform for high average PRR cycles (blue line) exhibits an increase in amplitude just after combustion when compared to the low average PRR cycles. Also, the time waveform takes on a characteristic period of oscillation. This characteristic frequency was determined by plotting a STFT of the low and high average PRR acoustic signals, see Figure 4.8 and Figure 4.9, respectively. The pressure trace has been added to Figure 4.8 and Figure 4.9 to identify events with relation to cycle timing. In Figure 4.8 and Figure 4.9, the majority of acoustic energy occurring during combustion is below 1000 Hz. Note the acoustic energy increases when the PRR and

peak pressure increases. To further estimate the frequency band containing this acoustic energy, the y-axes of the Figure 4.8 and Figure 4.9 were scaled from 0 – 1000 Hz and the x-axes were scaled to 0.022 – 0.026 s, see Figure 4.10 and Figure 4.11.

It was clearly evident from Figure 4.10 and Figure 4.11 there is a significant burst of energy in the 500 – 700 Hz bandwidth during combustion of an engine cycle for the high average PRR cycles when compared to the low average PRR cycles. Therefore, for this investigation, the energy contained in the 500 – 700 Hz bandwidth was used to characterize the combustion noise as detected by the microphone. The root mean square (RMS) value of the acoustic energy in this frequency band is used in this investigation for comparisons. The RMS value provides a measure of the magnitude of the acoustic energy in the frequency band.

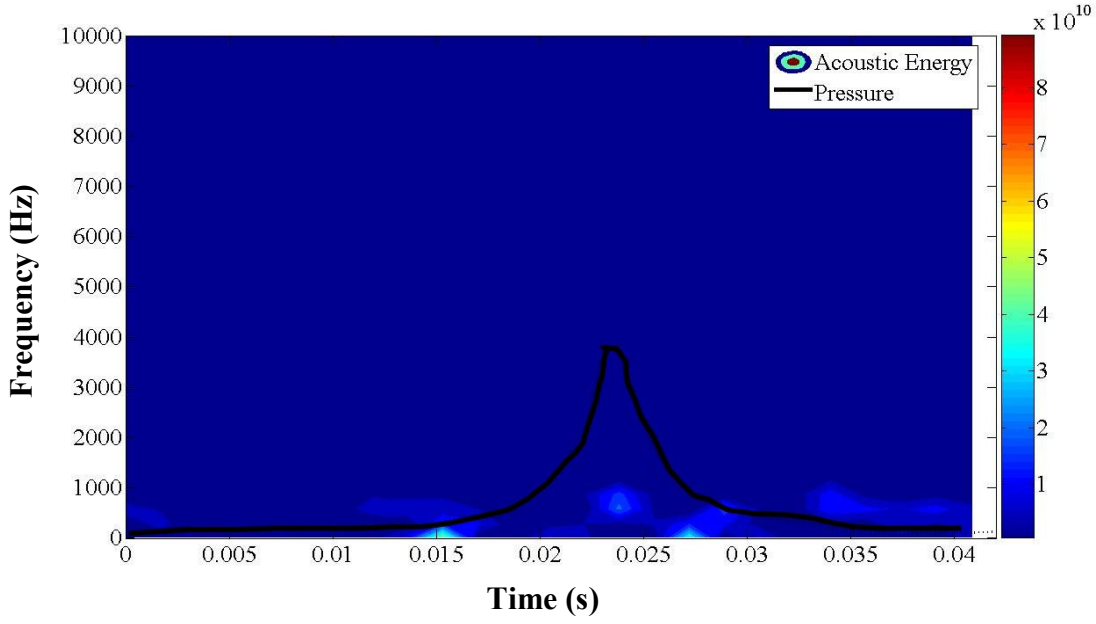

Figure 4.8 STFT of the acoustic energy for the **low** PRR 10 cycle average

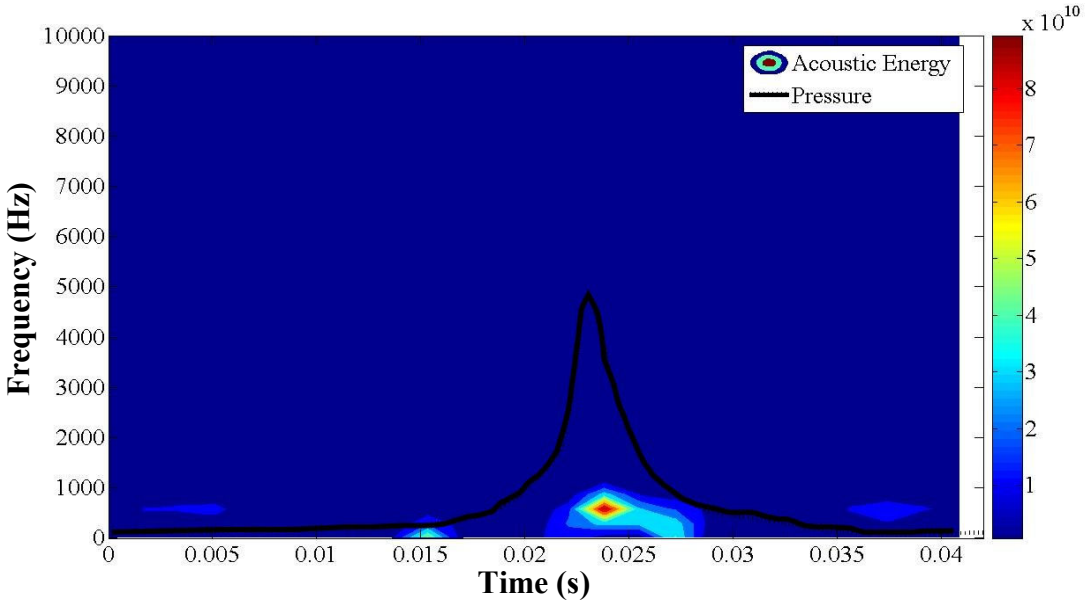

Figure 4.9 STFT of the acoustic energy for the **high** PRR 10 cycle average

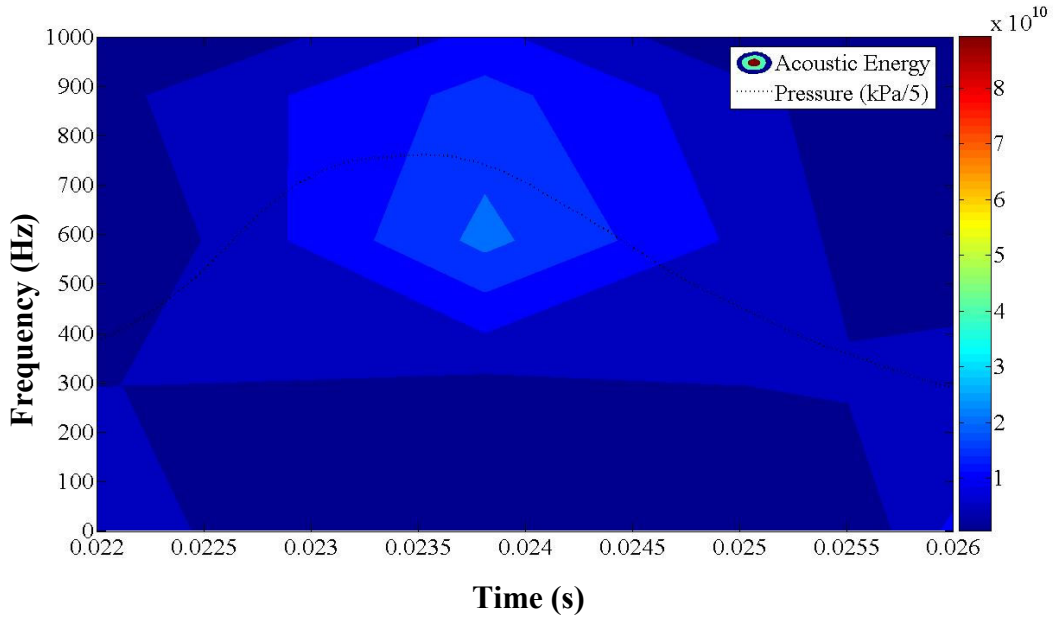

Figure 4.10 Examination of the acoustic energy occurring during combustion for the **low** PRR cycles

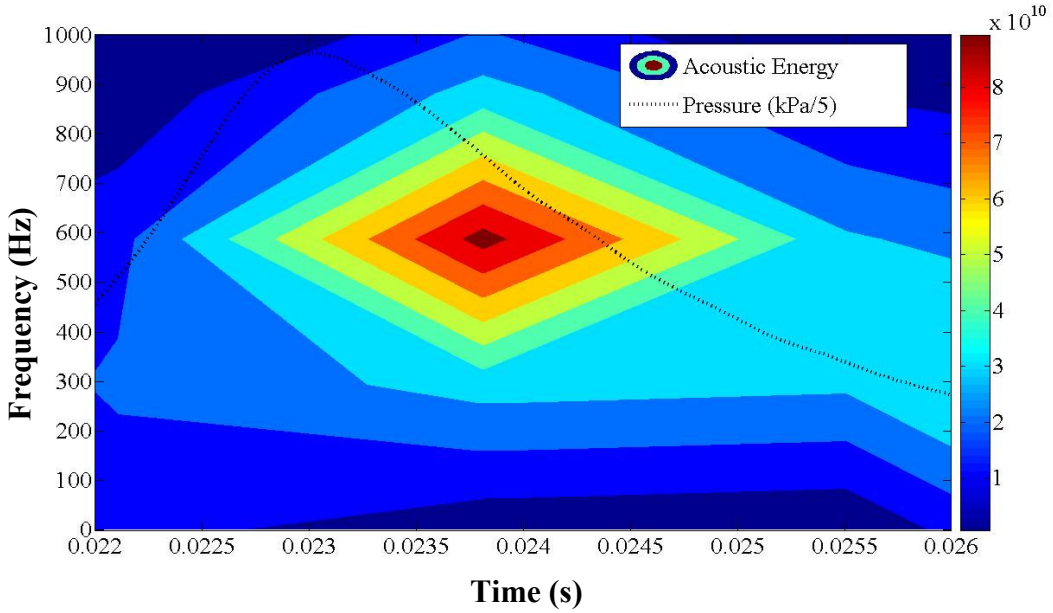

Figure 4.11 Examination of the acoustic energy occurring during combustion for the **high** PRR cycles

Vibration Frequency: The vibration waveform was analyzed in the same manner as the acoustic waveform. Ten cycles of low and high average PRR cycles were averaged and compared, see Figure 4.12. All accelerometer locations were investigated and exhibited the same frequency content at the 2520 rpm, 27.1 N-m set point, therefore the lower cylinder wall (LCW) accelerometer will be used for illustrations in this section. Notice the high average PRR cycles exhibit an increase in vibration energy during the combustion process. The small time delay in the vibration signal is negligible since the transducers are mounted directly to the engine structure.

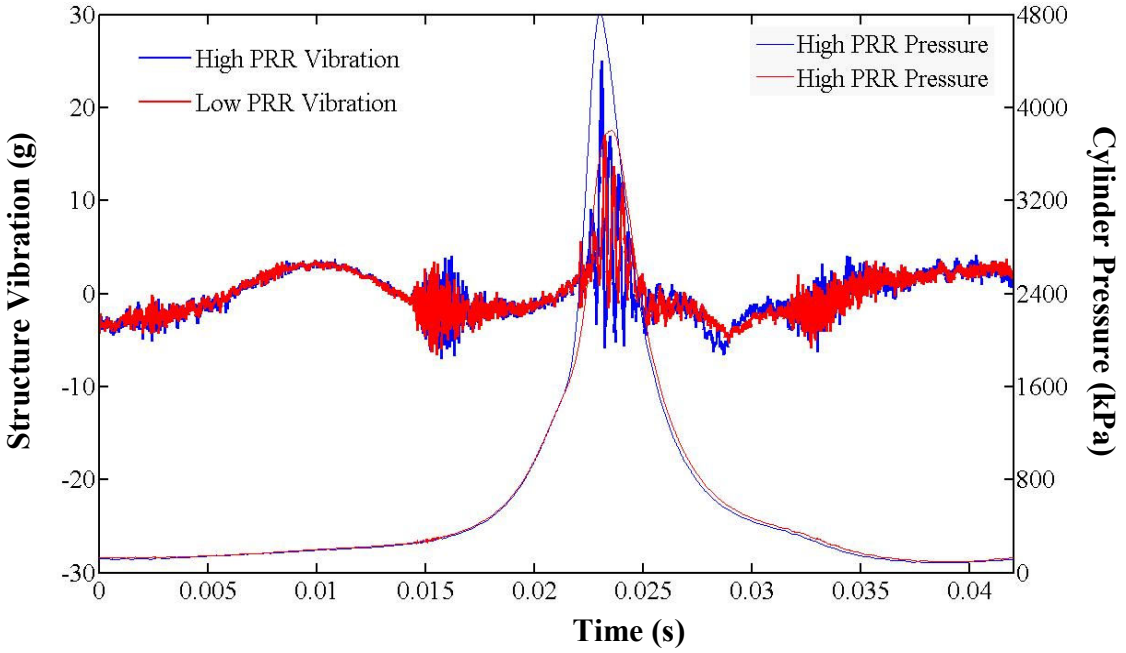

Figure 4.12 10 cycle average of the structure vibration from the SI engine for low and high PRR cycles with the corresponding 10 cycle average pressure signals added to identify cycle timing (2520 rpm, 27.1 N-m)

STFT's of the low and high average PRR LCW vibration waveforms, see Figure 4.13 and Figure 4.14, respectively, indicate a burst of vibration energy is occurring in the 2000 – 3000 Hz frequency band. The pressure and LCW vibration signals have been imposed on the STFT plots to identify when the events are occurring with respect to cycle time. Interestingly, it appears the burst of energy is occurring before combustion develops and is out of phase with the original time series vibration waveform. This is explained by the STFT windowing effect. When the STFT windows a segment of time and performs a FFT on the segment, the resulting frequency content is for an average time segment. Therefore, the time series events can slightly shift, depending on the window size used by the STFT.

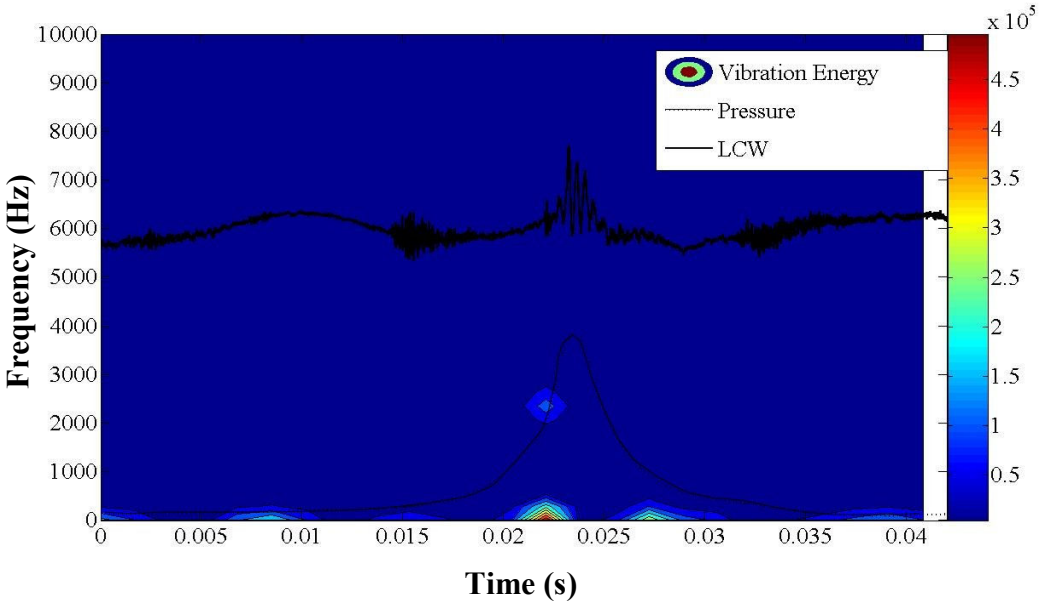

Figure 4.13 STFT of the structure vibration energy for the **low** PRR 10 cycle average

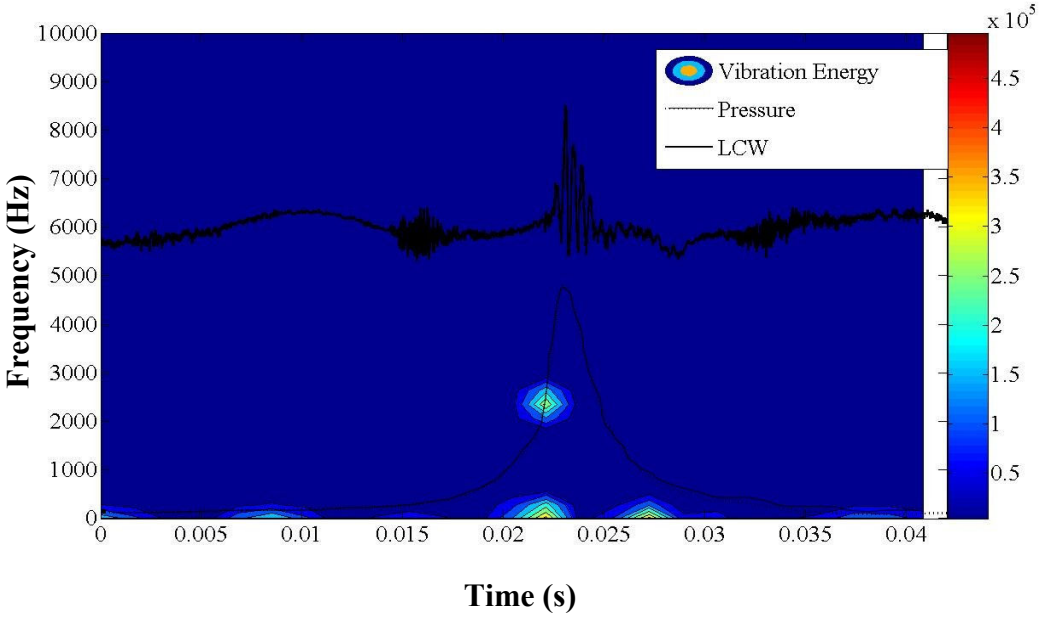

Figure 4.14 STFT of the structure vibration energy for the **high** PRR 10 cycle average

Since the vibration energy in the 2000 – 3000 Hz frequency band represented by the STFT appeared to be occurring before combustion, further verification was desired

before this frequency band was selected to characterize vibration energy resulting from combustion. Therefore, the vibration waveform for both the low and high average PRR LCW accelerometer waveforms was windowed from 0.022 - 0.026 s and the Fourier transform was used to extract the frequency content, see Figure 4.15.

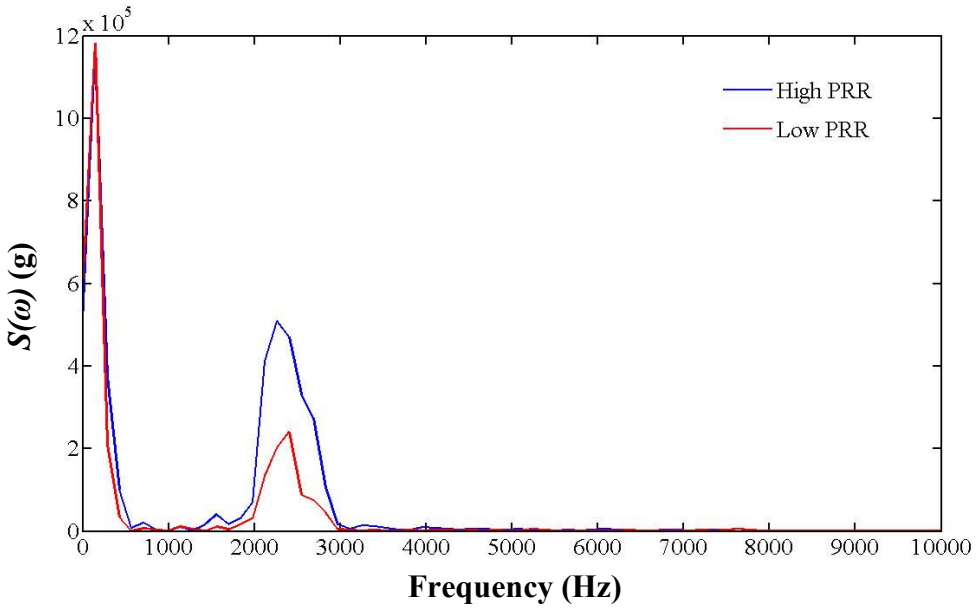

Figure 4.15 Frequency content of structure vibration occurring during combustion for low and high PRR cycles

Notice there are two large peaks in the frequency spectrum of the vibration waveform. The first peak is occurring at approximately 141 Hz and has the same magnitude for both low and high average PRR cycles. This peak represents a low frequency sine wave apparent in the signal, most likely from the AC powered signal conditioners used with the accelerometers. Further investigation confirmed that this signal is an approximately 75 Hz sine wave, see Figure 4.16.

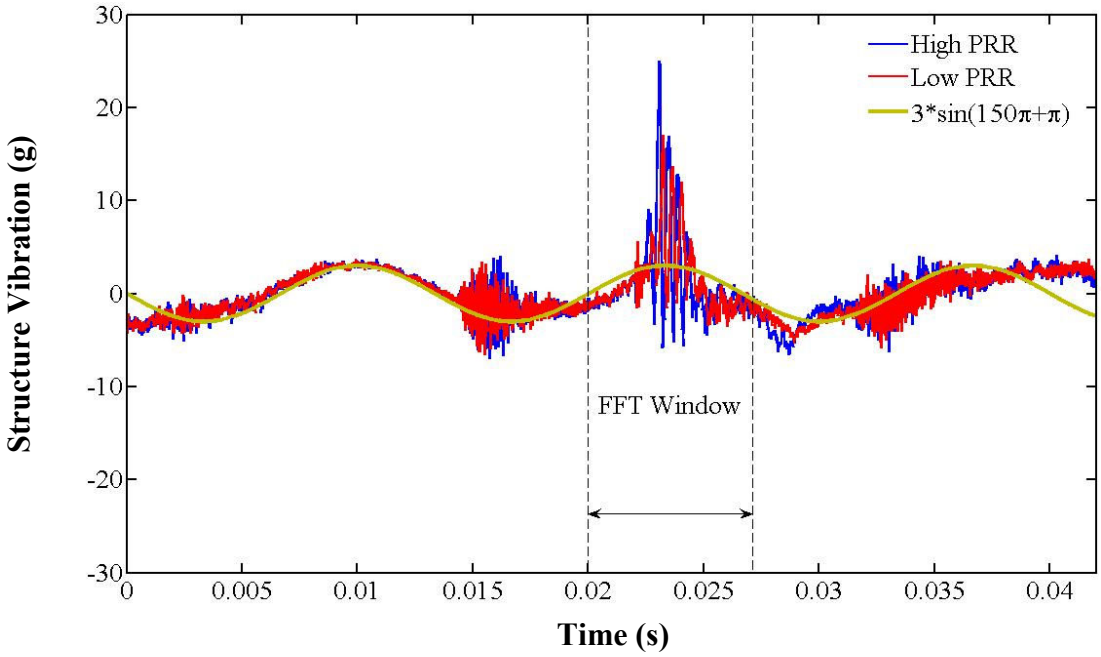

Figure 4.16 Illustration of the low frequency sine wave imposed on the vibration signal from the vibration signal conditioners

Notice that the sine wave matches the low amplitude wave imposed on the vibration signal, confirming the small influence of the AC powered signal conditioners. It is important to explain why this peak is occurring at 141 Hz in the frequency spectrum. The Fourier transform was implemented on very a small window of time, shown in Figure 4.16, and, consequently, a small number of discrete samples. Recall the sampling rate and number of samples have a direct effect on the frequency resolution, governed by Equation 4.1. The number of samples used in the Fourier transform of the "FFT Window" portion of Figure 4.16 was 625 with a sampling rate of 88,200 Hz, resulting in a frequency resolution of:

$$\Delta f = \frac{1}{625 \text{ samples}} \times 88{,}200 \frac{\text{samples}}{\text{sec}} = 141 \text{ Hz}. \tag{4.14}$$

Therefore, due to aliasing, the low level 75 Hz wave imposed on the vibration signal is being represented on the first frequency node in the frequency spectrum (i.e. 141 Hz).

The second peak in Figure 4.15 is occurring between 2000 and 3000 Hz. Notice the magnitudes for the low and high PRR cycles power spectrum are different in this frequency band. The frequency resolution of 141 Hz imposes a small amount of aliasing at this high of frequency. However, since the frequency bands investigated are approximately 15 times in magnitude of the frequency resolution and the energy increase is over a much wider band, it was apparent the aliasing had only a minimal effect on the frequency spectrum resulting in a good representation of the frequency content. Considering the frequency spectrum of the vibration waveforms occurring during combustion along with the vibration signals' STFTs, for this investigation, the energy contained in the 2000 – 2500 Hz frequency band was chosen to represent the SI engine's structure vibration response to combustion. An RMS value was calculated from the power spectrum contained in the 2000 – 2500 Hz frequency band to provide a viable metric for comparisons.

5. TRENDS INDICATING LEVEL OF PRESSURE RISE RATE VIA ACOUSTIC AND VIBRATION EMISSION

This investigation involved experiments on two internal combustion engines. A small single-cylinder spark ignition (SI) engine and a larger multi-cylinder Mercedes 1.7L compression ignition (CI) engine were used. The majority of the analyses were conducted on the SI engine. Acoustic and structure vibration measurements were readily available for this engine. The SI engine was operated under normal combusting conditions (i.e. no auto-ignition of the fuel/air mixture). Due to the short amount of time available for experiments on the CI engine, only structure vibration data was collected. These experiments allowed for comparisons between a small displacement SI engine and a large CI engine. The results from both engine platforms will be presented in this section. Results will begin with the SI engine, with the CI engine following.

5.1 SI ENGINE INVESTIGATION

Both acoustic and vibration measurements were made on the SI engine; therefore this section will be divided into three subsections. Subsection 5.1.1 will explain initial acoustic experiments conducted and present the results from those experiments. Based upon the results from Subsection 5.1.1, it was decided further vibration and acoustic investigations should be conducted to better understand any relationship between the structure vibration/acoustic emissions and the PRR. Subsection 5.1.2 will focus on results from the structure vibration measurements. Acoustic measurement results will be presented in Subsection 5.1.3.

For the SI engine results, reference will be made to certain set point numbers given in Table 5.1. This table is comparable to Table 4.1 with the torque value replaced by the average *net indicated mean effective pressure* (IMEPn).

Table 5.1 SI engine operating set points

Set Point	Speed (rpm)	IMEPn (kPa)
1	1500	231
2	1500	533
3	2520	231
4	2520	533
5	2520	945
6	3000	231
7	3000	533
8	3000	945

While torque is a good measure of a particular engine's ability to do work, it is dependent upon engine size and engine friction. Therefore, a more relative engine performance parameter is desired to represent the work output of the engine cylinder. Heywood [18] defines the IMEPn as the work delivered to the piston over the entire four strokes of the cycle, per unit displacement. The IMEPn is obtained by integrating the per cycle cylinder pressure (p) with respect to cylinder volume (V) and normalizing by the displacement volume (V_d) of the engine. This definition is written mathematically as:

$$\text{IMEPn} = \frac{\int p dV}{V_d}. \tag{5.1}$$

Since the acquired cylinder pressure is a discrete signal, the trapezoidal rule is implemented to calculate the integral. The final numerical calculation of the IMEPn from the cylinder pressure becomes:

$$\text{IMEPn} = \frac{[p_i + p_{i+1}][V_{i+1} - V_i]}{2V_d}. \tag{5.2}$$

Using the IMEPn as a metric representing the engine work output (or load) facilitates comparison of the results to other engines of different sizes. Note, from equation 5.2, the IMEPn will have units of pressure.

For the following vibration and acoustic results, the vibration and acoustic data will be presented in values of bits. This is the default raw signal format exported from the Adobe Audition recording software. The units of the vibration and acoustic data results are irrelevant for this study, since the results will focus on differences in magnitudes and data trends rather than absolute values.

To calculate a metric useful for comparisons, the Fourier transform was applied to the structure vibration and acoustic data on a per cycle basis at each accelerometer location. Once the spectral content was extracted, RMS values for the 500 – 700, 2000 – 2500, and 6000 – 6600 Hz frequency bands were calculated. Averages over 500 engine cycles of the calculated RMS value will be used in the average set point comparisons in the following results. The single-cycle based RMS value will be used in the per-cycle investigations in the following results.

5.1.1 Initial Experiments. Initial experiments were conducted on the small-single cylinder SI engine at only a single operating condition: 2520 rpm, 947 kPa IMEPn. This high-load operating condition was initially selected due to a sharp, non-periodic annoying noise being detected from the engine at this operating speed and load. Upon

investigation of the annoying noise, an increasing trend between the acoustic emissions in the 500 – 700 and 2000 – 2500 Hz frequency bands and the average PRR was noticed, see Figure 5.1 and Figure 5.2. Figure 5.1 and Figure 5.2 show 500 engine cycles of acoustic emission in the 500 – 700 and 2000 – 2500 Hz frequency bands, respectively, plotted as a function of the average PRR. It was clear an increase in the average PRR resulted in an increase in magnitude of the acoustic emissions in these frequency bands. From these results, it was desired to investigate these trends at other operating conditions, i.e. other speed and load combinations.

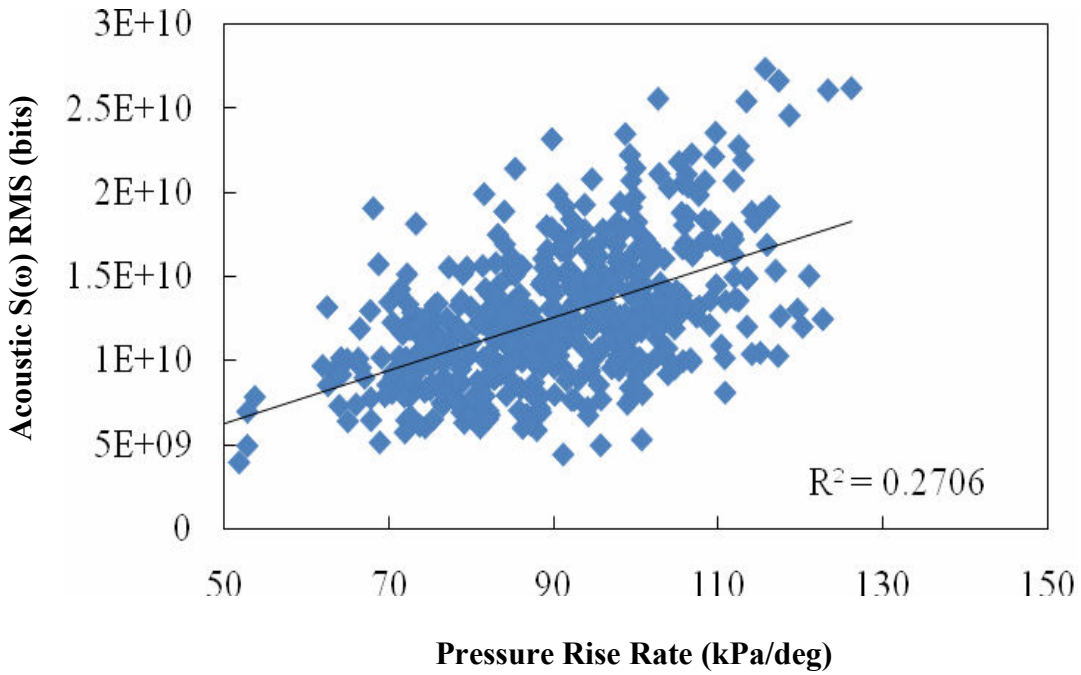

Figure 5.1 Per-cycle 500 – 700 Hz frequency band acoustic emission as a function of the average PRR (2520 rpm, 947 kPa)

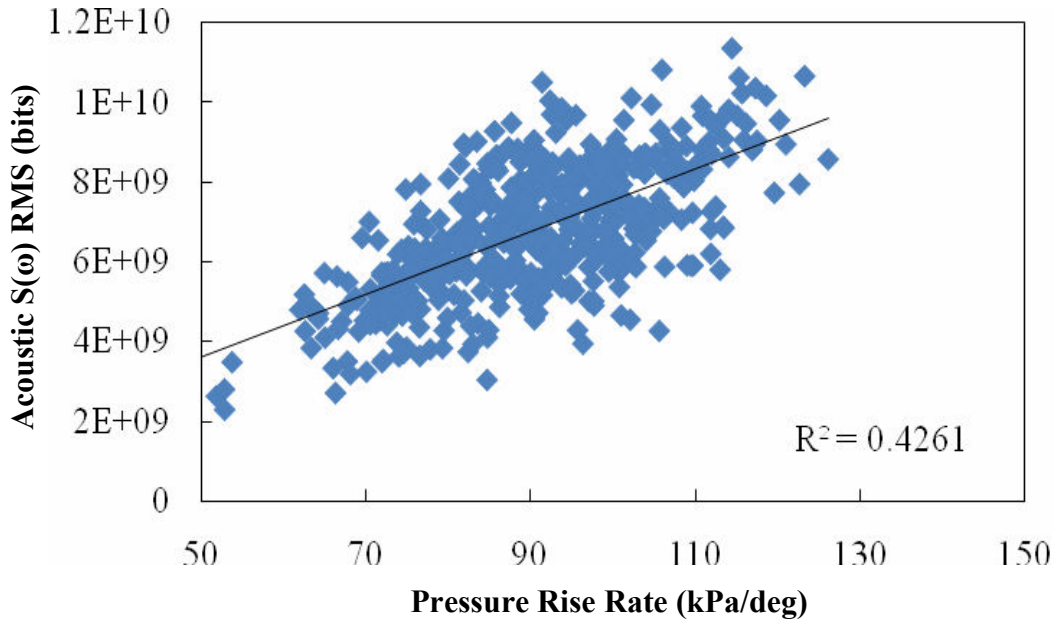

Figure 5.2 Per-cycle 2000 – 2500 Hz frequency band acoustic emission as a function of the average PRR (2520 rpm, 947 kPa)

5.1.2 Structure Vibration Results. Following the initial acoustic emission experiments, attention was directed toward the structure vibrations to identify possible acoustic energy transmission sources. However, presenting these results would be beyond the scope of this Thesis. Therefore, only trends between the structure vibrations from the previously specified frequency bands and the PRR will be presented.

5.1.2.1 Set point speed and load average results. Before detailed per cycle correlations were investigated, it was desired to establish any possible general trends of the structure vibration level of the engine when the speed and load was changed. These trends will be compared to the development of PRR with speed and load. A 500 cycle average of the per-cycle RMS values for the energy contained in the 500 – 700 Hz frequency band of the flywheel accelerometer was calculated and plotted as a function of

speed, see Figure 5.3. The LCW accelerometer exhibited the same trends for this comparison. The different color markers represent the average IMEPn, indicative of the engine load, of the set points given in Table 5.1. Each marker represents a 500 cycle average of vibration energy at a set point given in Table 5.1.

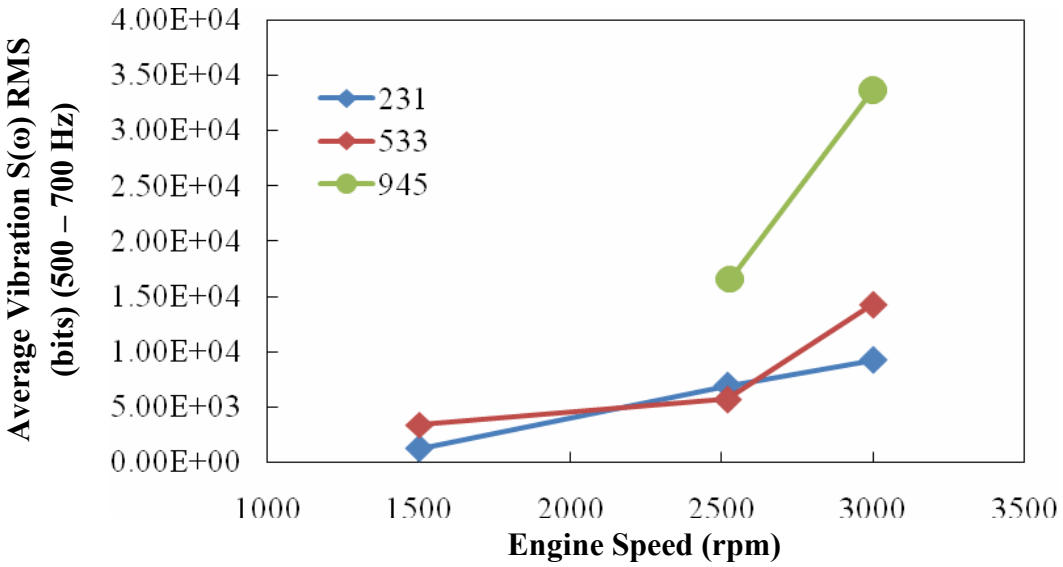

Figure 5.3 Development of flywheel structure vibrations (500 - 700 Hz) with speed and load

Interestingly, the vibration energy contained in the 500 – 700 Hz frequency band of the flywheel and LCW vibrations exhibited a general increase with speed and load. The 231 kPa IMEPn yields a near linear development with speed. However, the 533 kPa IMEPn does not exhibit the same trend. Although the values increase with speed, the increase is not linear and the average vibration energy at a speed of 2520 rpm drops below that of the lower 231 kPa IMEPn at the same speed. The exact reason for this nonlinear trend is unclear. Note the average vibration level of the 500 – 700 Hz

frequency band at the 945 kPa IMEPn does increase with speed. In fact, this vibration level increase with speed is seen for all frequency bands of all vibration and acoustic data at the high-load 945 kPa IMEPn engine operating condition. In general, the average structure vibration levels for the flywheel and LCW accelerometer locations exhibit increases with speed and load, excluding the 2520 rpm, 533 kPa set point.

The UCW structure vibrations exhibited slightly different behavior with increasing speed and load, see Figure 5.4. Although the 500 – 700 Hz vibration level increases are not linear, it is apparent the vibration level at the UCW structure vibration does increase with increasing speed and load.

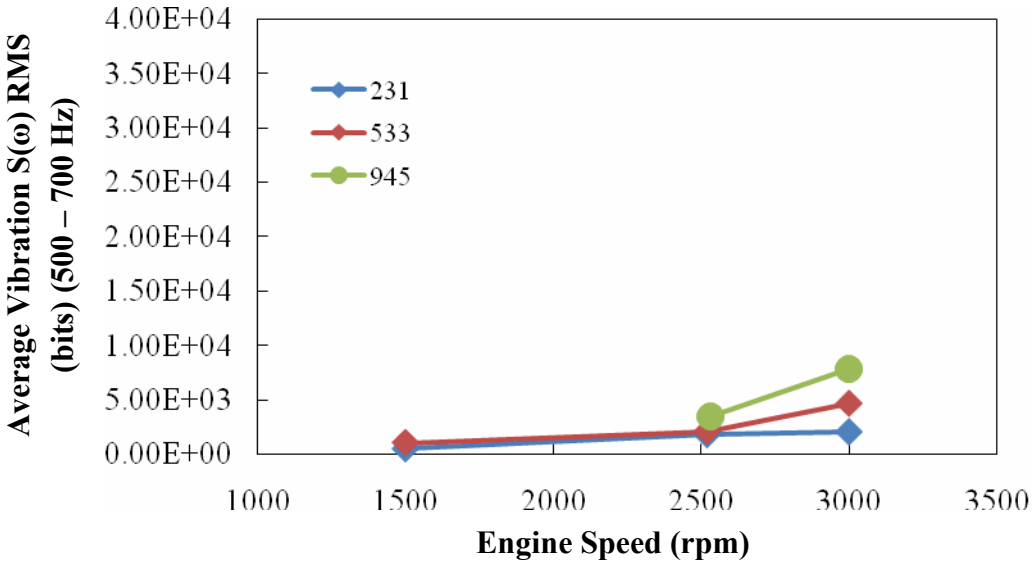

Figure 5.4 Development of UCW structure vibrations (500 - 700 Hz) with speed and load

Investigation of the BCW structure vibrations in the 500 – 700 Hz frequency band yields differing results from the other structure vibration locations previously presented,

see Figure 5.5. Again, for each load, there is a general increase of structure vibration level in the 500 – 700 Hz frequency band with speed. Interestingly, the vibration level at the 3000 rpm, 533 kPa is lower than the vibration level at the 3000 rpm, 231 kPa set point. Again the reason for this result is unclear. However, in general, the vibration levels are increasing with speed and load.

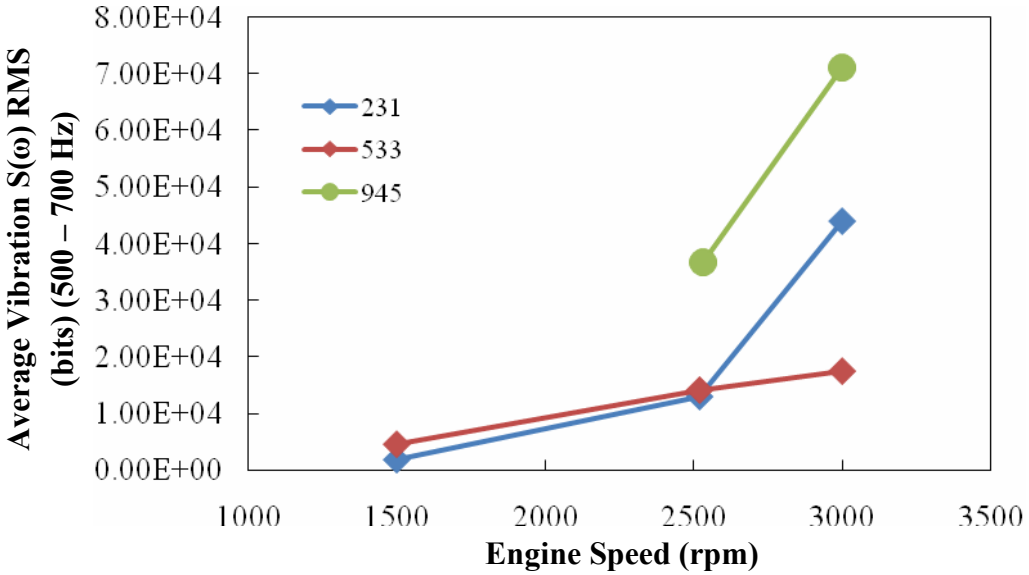

Figure 5.5 Development of BCW structure vibrations (500 - 700 Hz) with speed and load

The vibration level in the 500 – 700 Hz frequency band, characterizing the combustion energy, exhibited somewhat inconsistent results for the four structure vibration locations, but did show a general increasing trend with speed and load. The structure vibrations in the 2000 – 2500 and 6000 – 6600 Hz frequency bands exhibited much more consistent behavior, see Figure 5.6. Figure 5.6 shows the development of the LCW structure vibrations in the 2000 – 2500 Hz frequency band with increasing speed

and load. The 6000 – 6600 Hz structure vibrations, characterizing the cavity resonant mode, exhibited the same trend and will not be shown. Note the vibration levels in increase as the speed and load increase. This trend is seen at all four accelerometer locations for both the 2000 – 2500 and 6000 – 6600 Hz frequency band.

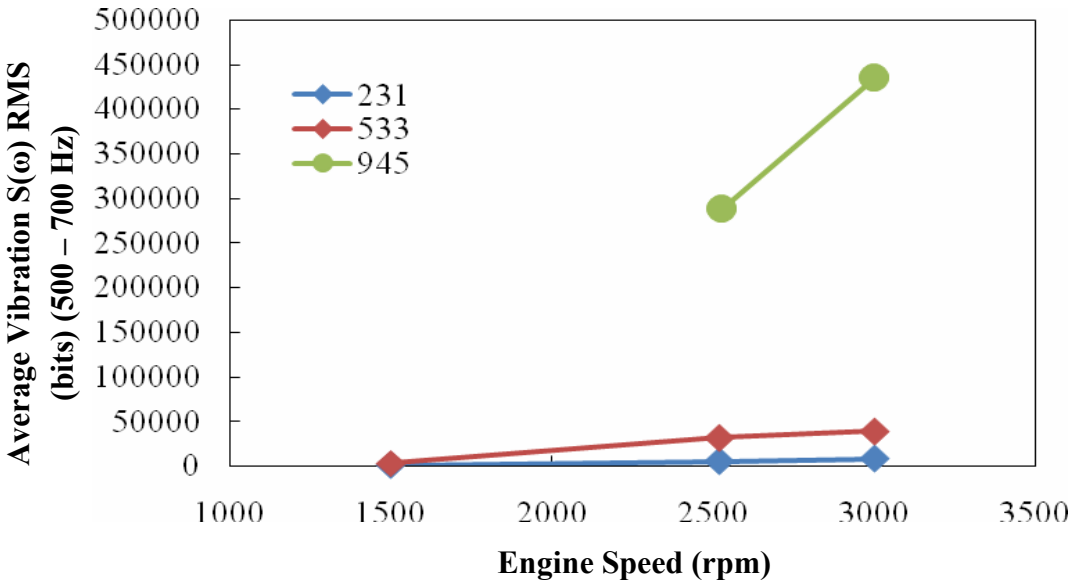

Figure 5.6 Development of LCW structure vibrations (2000 - 2500 Hz) with speed and load

Next, the 500 cycle average PRR for each set point was plotted as a function of speed and load to investigate the development of the average and instantaneous PRR with increasing speed and load, see Figure 5.7. The instantaneous PRR exhibited the same trends as the average PRR. Interestingly, the average PRR value decreases with increasing speed, but increases with load. Notice, the large increase in magnitude of the structure vibrations and PRR between the 533 and 945 kPa IMEPn operating points. This is not surprising since the difference in engine work output, characterized by the IMEPn,

between the 945 kPa and the 533 kPa operating point is almost twice the difference between the 533 kPa and 231 kPa operating points.

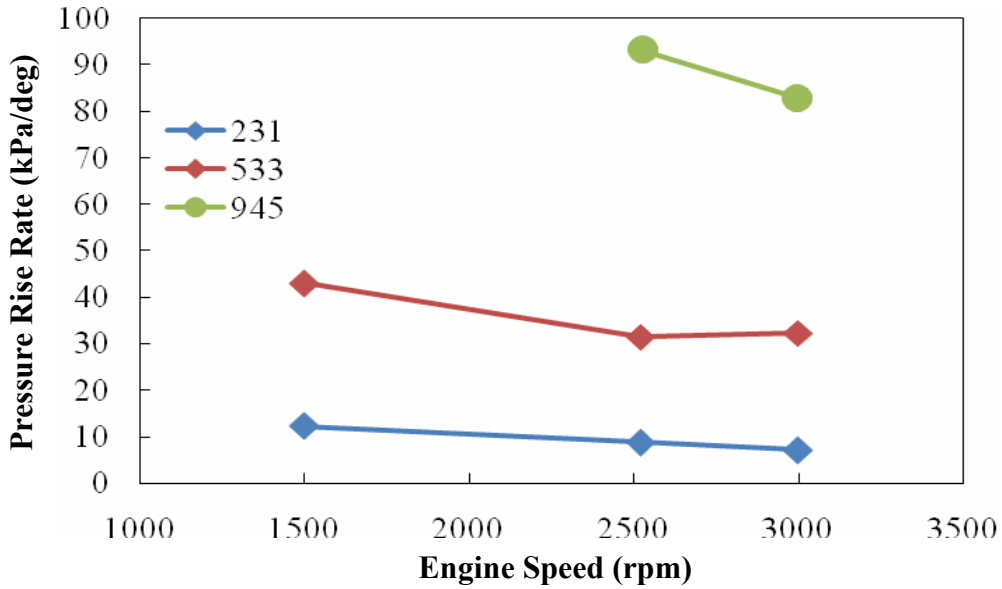

Figure 5.7 Development of average PRR with speed and load

The increase of PRR with load at a given speed is a result of introducing more fuel to achieve greater work output. The SI engine used a carbureted fuel delivery system. As the throttle was opened and more air was inducted into the engine, to maintain a specific equivalence ratio (the ratio of the actual fuel/air ratio to the stoichiometric fuel/air ratio), the amount of fuel delivered was increased. Increasing the amount of fuel-air mixture being inducted into the engine consequently resulted in higher charge densities in the engine cylinder. Higher charge densities resulted in increased pressure and temperature in the cylinder, leading to faster flame propagation and higher mixture burning rates.

Increasing the engine speed also increases turbulence in the engine cylinder thus increasing the rate of development and propagation of the turbulent premixed engine flame. However, the increased engine speed decreases the amount of time required to travel one crank-angle-degree (CAD). The increase in flame propagation speed and decrease in CAD time are not linearly proportional and therefore an increase in engine speed results in a slight increase in combustion duration in CAD. Also, the spark timing is constant for this SI engine regardless of speed and load. This results in operating set points that produce peak pressures at cycle times that are not coincident with the maximum-brake-torque (MBT) cycle time (conventionally 16 CAD ATDC). The increased combustion duration and off MBT peak pressure timings results in lower peak pressures occurring later in the cycle for higher speeds. Recall the average PRR is calculated using a least-squares linear regression from start of combustion (SOC) to peak pressure. To better understand the development of the cylinder pressure, from which the average and instantaneous PRR is derived, at constant load but increasing speed, a 10 engine cycle average of cylinder pressure for each speed at an average load of 231 kPa was plotted as a function of crank-angle-degree (CAD), see Figure 5.8. It is clearly evident the lower pressure values along with longer combustion duration in CAD from SOC to peak pressure for the higher speed case would result in lower average PRR values.

Generally, the structure vibration magnitudes at all four accelerometer locations for all three frequency bands increased with speed and load. Conversely, the average and instantaneous PRR magnitudes decreased with speed but increased with load. This indicates, for constant engine speed operating conditions, the structure vibrations may be

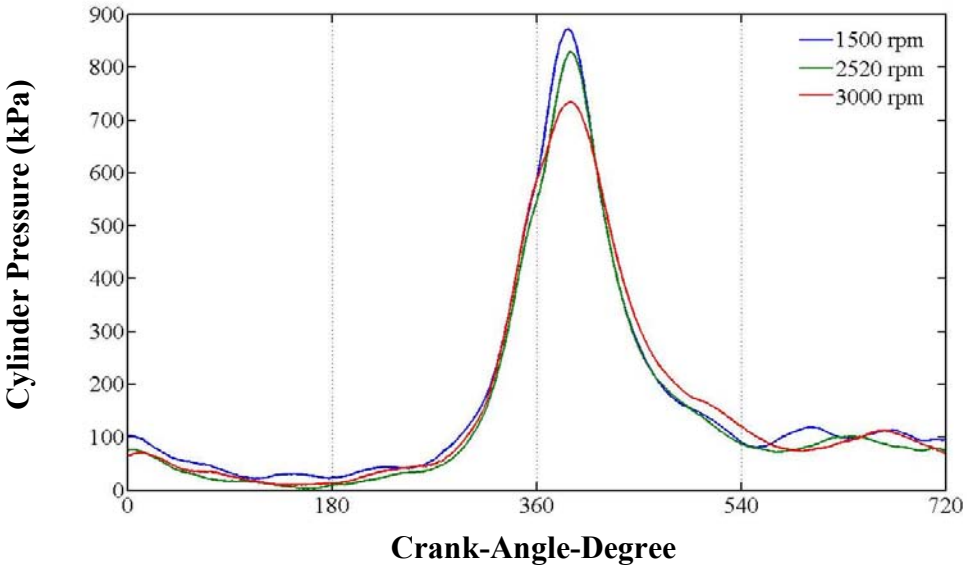

Figure 5.8 A 10 engine cycle average comparison of cyilnder pressure for increasing speeds at a constant load of 231 kPa

able to indicate average cylinder PRR resulting from load variations. However, if a constant load is maintained and speed is varied, the structure vibrations would be less likely to indicate the level of cylinder PRR. If comparison of the average magnitude of PRR at different operating conditions, regardless of speed and load, is desired with non-intrusive sensors, i.e. without using a cylinder pressure transducer, the results show average structure vibrations would be inconsistent. The general speed and load comparisons provided an initial indication of a relation between the structure vibrations and the cylinder PRR. However, direct comparisons between the structure vibrations and the PRR should be investigated before any final conclusions are made.

5.1.2.2 Set point average structure vibrations and PRR comparisons. To investigate any other relation between the structure vibrations and level of PRR, 500 cycle average structure vibration were plotted as a function of average and instantaneous

PRR, see Figure 5.9 and Figure 5.10, respectively. The set point values from Table 5.1 have been added to identify which engine operating condition the markers represent. All four accelerometer locations exhibited the same trends and therefore only the LCW results are shown. Notice, in general, there is an increasing trend in the structure vibration levels with increases in the PRR. However the data exhibits a large amount of scatter due to the vibration level changes resulting from engine speed changes.

Interestingly, if the each marker in Figure 5.9 is formatted according to its speed set point (i.e. 1500, 2520 and 3000 rpm), the structure vibration in the 500 – 700 Hz frequency band exhibits a linear increase with the PRR, see Figure 5.11. For an engine operating under varied speed and load conditions, the average RMS value for structure vibrations in the 500 – 700 Hz frequency band, representing the combustion frequency, would provide inadequate representation of the overall magnitude of the PRR. However, for comparisons of an SI engine operating under a changing load at constant speed condition, the structure vibrations provide some level of indication of PRR. The only contradiction to this result is that, from Figure 5.11, the structure vibrations are less sensitive to changes in PRR at low speeds. Therefore, as the speed is increased, the structure vibrations exhibit a greater ability to predict the PRR. Interestingly, for the 2520 rpm speed set point, the structure vibrations in the 500 – 700 Hz frequency band for the higher load number 4 set point decreases. The reason for this decrease from the same speed, lower load number 3 set point is unknown.

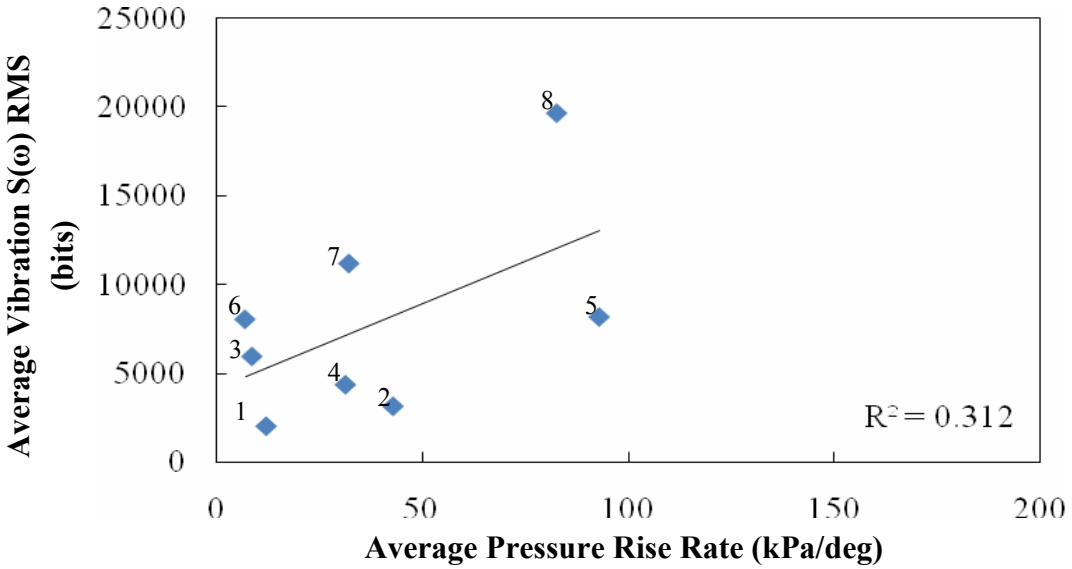

Figure 5.9 A 500 cycle average of LCW 500 – 700 Hz frequency band structure vibration RMS as a function of average PRR, each point represents a set point from Table 5.1

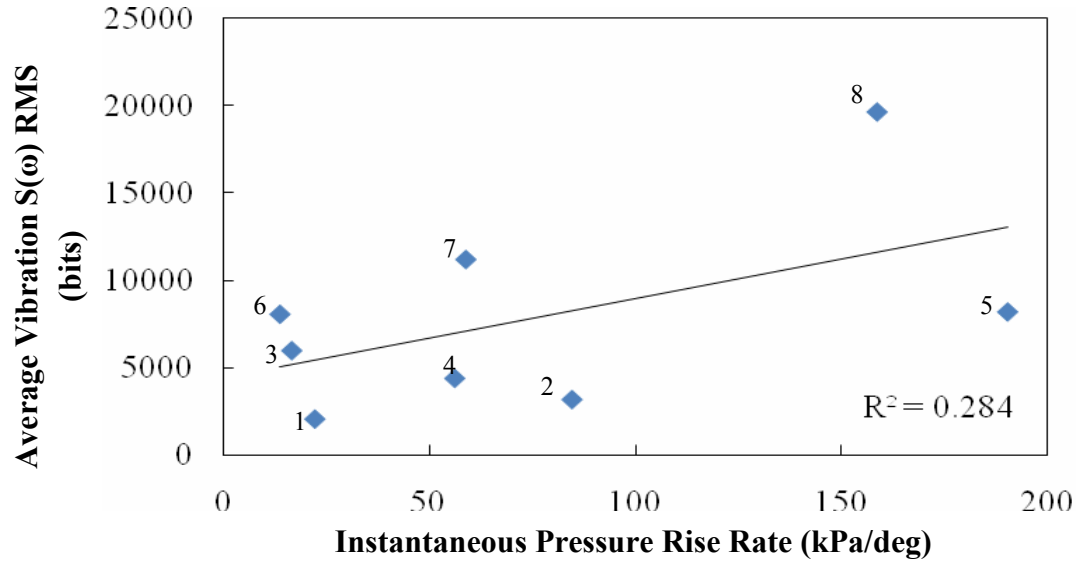

Figure 5.10 A 500 cycle average of LCW 500 – 700 Hz frequency band structure vibrations RMS as a function of instantaneous PRR, each point represents a set point from Table 5.1

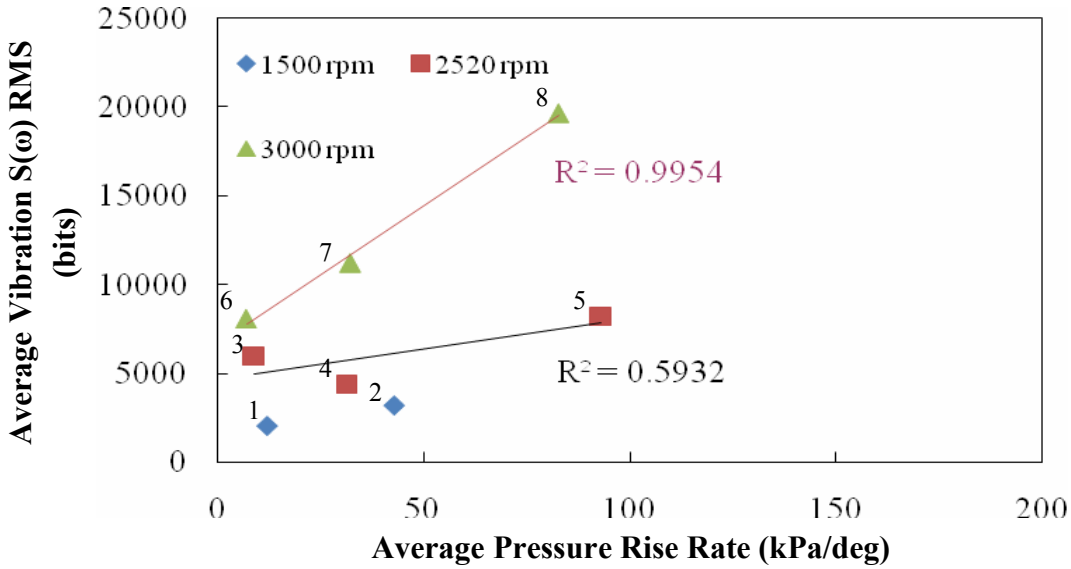

Figure 5.11 Influence of engine speed on 500 cycle average LCW 500 – 700 Hz frequency band structure vibrations RMS as a function of average PRR

Comparisons of the structure vibrations in the 2000 – 2500 Hz and 6000 – 6600 Hz frequency bands to the average PRR were conducted in the same manner as the 500 – 700 Hz frequency band, see Figure 5.12 and Figure 5.13, respectively. Comparison of the vibrations in these frequency bands to the instantaneous PRR exhibited similar trends and will not be shown. The scatter between each engine set point becomes much lower, yielding a better correlation between the structure vibrations in these frequency bands and the PRR. Note the trend is not as easily discerned for the 2000 – 2500 Hz structure vibration comparison in Figure 5.12. This is due to the large structure vibration magnitude difference between the mid- and high-load cases. Again, all four accelerometer locations exhibited the same results and therefore only the LCW results are shown. Recall for the 500 – 700 Hz frequency band, the mid-load case at the 2520 rpm engine speed exhibited lower average structure vibration magnitudes than the low-load

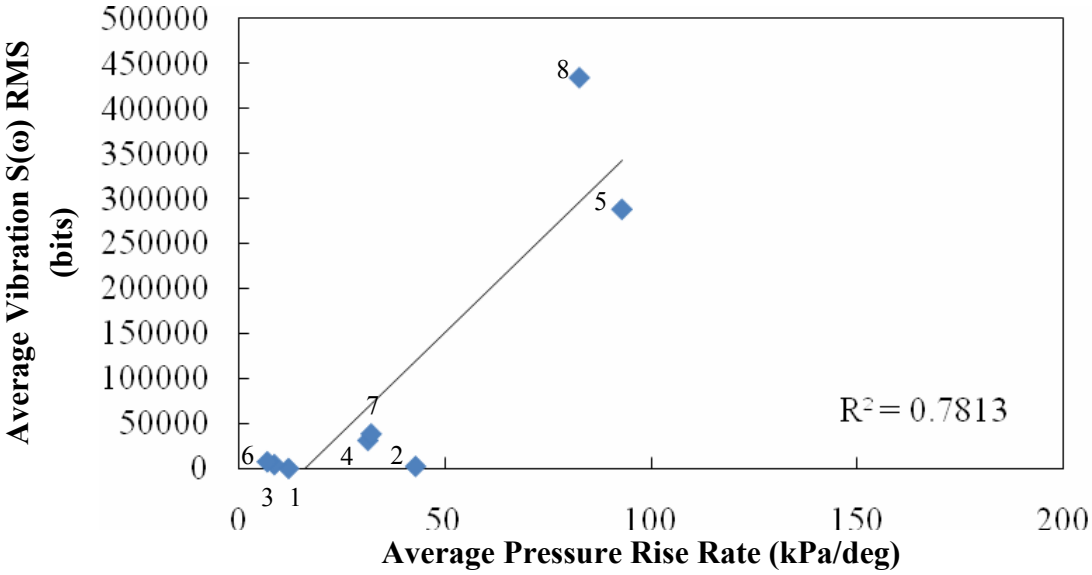

Figure 5.12 A 500 cycle average of LCW 2000 – 2500 Hz frequency band structure vibrations RMS as a function of average PRR, each point represents a set point from Table 5.1

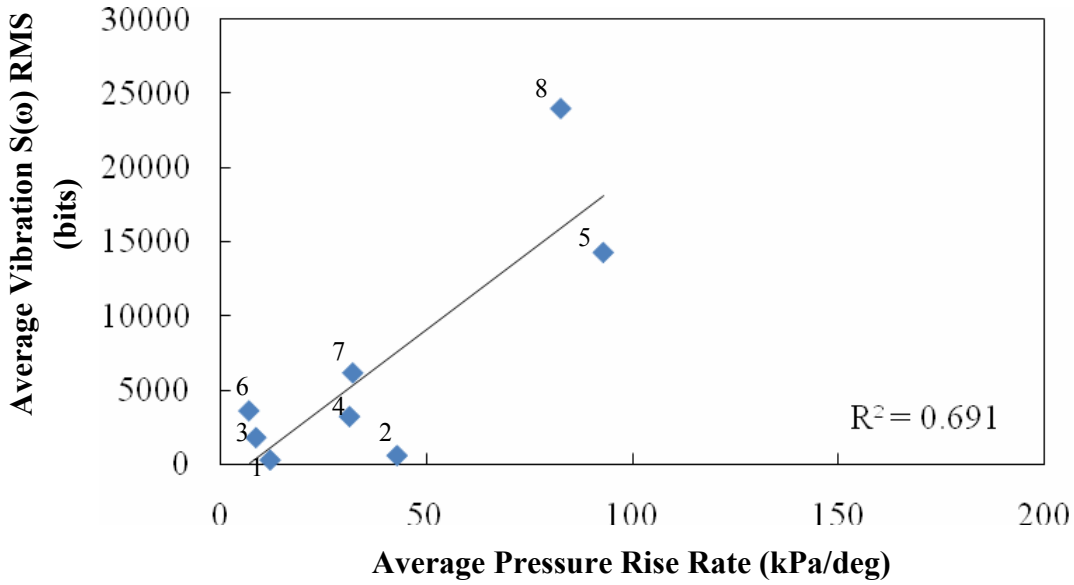

Figure 5.13 A 500 cycle average of LCW 6000 – 6600 Hz frequency band structure vibrations RMS as a function of average PRR, each point represents a set point from Table 5.1

case for the same speed. The vibration levels at all accelerometer locations for both the 2000 – 2500 Hz and 6000 – 6600 Hz frequency bands did not exhibit this mid-load decrease at the 2520 rpm speed. From these results, it was suspected these frequency bands in the structure vibrations were more sensitive to the level of PRR than the lower frequency band of 500 – 700 Hz.

The direct structure vibration and PRR comparisons showed an increasing sensitivity of the vibration emission levels to PRR with increasing engine speed. Consistent with the average speed and load results, the direct comparison results also exhibit the increasing structure vibration levels with increasing PRR. Considering these two results together, it was suspected structure vibration levels would be less likely to indicate PRR levels at low engine speed and load set points. Conversely, it was suspected the structure vibration levels would provide adequate indication of the cylinder PRR levels at higher speed and load set points. However, per-cycle comparisons were to be conducted before final conclusions were drawn.

5.1.2.3 Per-cycle results. The structure vibrations in all the frequency bands analyzed generally increased as the average and instantaneous PRR's increased. These trends were seen on the previous average set point magnitude comparisons. Next, it was desired to investigate the sensitivity of response of the structure vibrations to PRR on a per engine cycle basis. A plethora of plots were constructed to investigate any correlations between the three structure vibration frequency bands and the PRR. It is not useful to include all of these in the results section, therefore this section of results will begin with listing the engine operating conditions at which no correlation was seen between the per-cycle structure vibrations and PRR. Next the results will be presented in

a low – high load format. Not surprisingly, this is due to the correlations of the per-cycle results being more dependent upon load than speed.

Per-cycle structure vibration RMS values for all three frequency bands along with the average and instantaneous PRR of 500 engine cycles were calculated at each engine operating condition. The per-cycle structure vibration RMS values were plotted as a function of the per-cycle average and instantaneous PRR. Figure 5.14 shows the results for the LCW structure vibrations in the 500 – 700 Hz frequency band at the number 1 set point from Table 5.1. It is clear no correlation exists between the structure vibration in this frequency band and the average PRR for each cycle. There were a number of set points at which the structure vibrations and average PRR did not correlate. These include all frequency bands for set points 1, 2 and 3 and the 6000 – 6600 Hz frequency band for all engine set points. Interestingly, there was no correlation between the per-cycle structure vibration RMS values and instantaneous PRR for any frequency band at any set point. The reason for this is unclear at this time. It is speculated that it may be a result of the calculation of the cylinder pressure derivative on a per-cycle basis. The cylinder pressure was not smoothed before the numerical derivative was calculated and there could be slight discontinuities (i.e. signal noise) that are present in the pressure trace causing erroneous peak values in the pressure derivative.

For the per-cycle results, the square of the correlation coefficient (R^2) value of the least-squares linear regression line applied to each plot was used to quantify how well the structure vibrations correlated to the average PRR. In the preceding discussions comparing the 500 cycle average vibration and PRR values, the R^2 values of the trends are displayed on the plots.

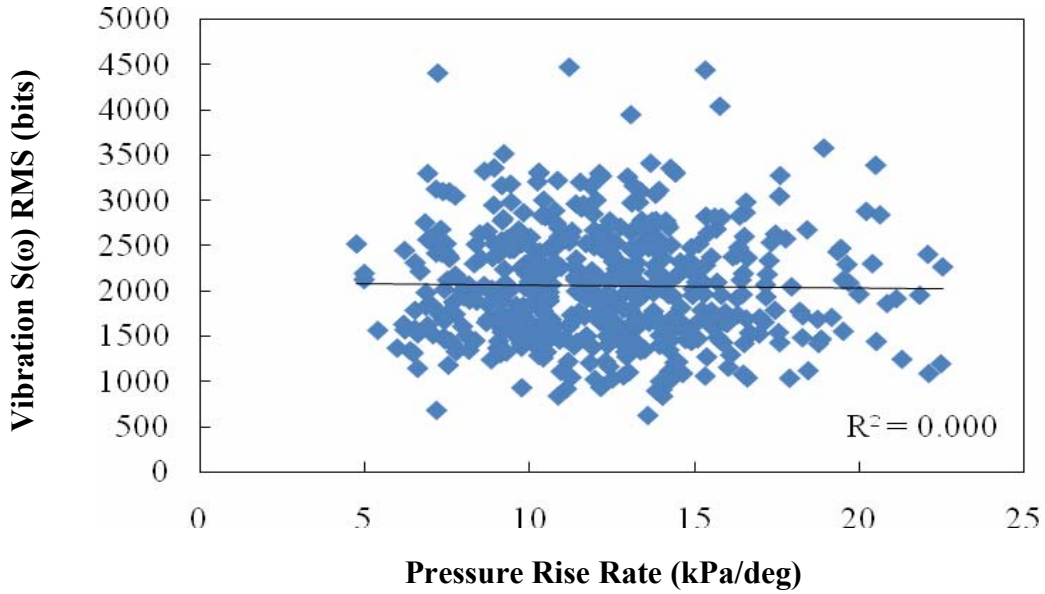

Figure 5.14 Per-cycle LCW 500 – 700 Hz frequency band structure vibrations as a function of the average PRR (1500 rpm, 231 kPa)

However, there were a small amount of samples present and the use of the R^2 value as a metric of determining the goodness of a fit was inadequate. For the per-cycle results, there are 500 points for each set point which provides a larger sample set to predict the correlation between the structure vibrations and the PRR. Since the sample set is larger, the R^2 value will provide an adequate indication of the goodness of fit of the linear least-squares regression lines applied, and therefore initially indicate the strength of the correlation between the structure vibrations and average PRR. Devore [19] identifies the values of the correlation coefficient R that indicate the level of strength of a linear fit as: R = 0 – 0.49 as a weak fit; R = 0.5 – 0.79 as a moderate fit; and R = 0.8 – 1.0 as a strong fit. These values correspond to R^2 = 0 – 0.24 as a weak fit, R^2 = 0.25 – 0.63 as a moderate fit, and R^2 = 0.64 – 1.0 as a strong fit. These R^2 values will be used to quantify the strength of the correlation between the vibration and acoustic data and the PRR.

Both the 1500 and 2520 rpm speed set points for the 231 kPa IMEPn showed no correlation between the structure vibrations in any frequency band analyzed at any accelerometer location and the average PRR. Interestingly, the 3000 rpm speed showed slightly different results. The flywheel structure vibrations in the 500 – 700 Hz frequency band yielded a moderate correlation as shown in Figure 5.15. The UCW structure vibrations in the 500 – 700 Hz frequency band exhibited the same behavior as shown in Figure 5.15 and will not be presented. The vibrations sensed at the LCW and BCW accelerometer locations for the 3000 rpm engine speed exhibited no correlations to the average PRR. Although the bulk of the cycles are clustered between 2.5 and 10 kPa/deg, it is clear that as the average PRR increased, so did the structure vibration in the 500 – 700 Hz frequency band. As for the structure vibrations in the 2000 – 2500 Hz frequency band, only weak correlations were found between the structure vibrations at any accelerometer location and the average PRR.

As the load was increased from 231 kPa to 533 kPa IMEPn, the structure vibrations became more sensitive to changes in PRR. Figure 5.16 shows the moderate correlation between the structure vibrations in the 500 – 700 Hz frequency band at the flywheel accelerometer location and the average PRR. The 500 – 700 Hz vibrations at the BCW accelerometer location exhibited the same results as the flywheel; however, the vibrations at the LCW and UCW locations exhibited weak correlations.

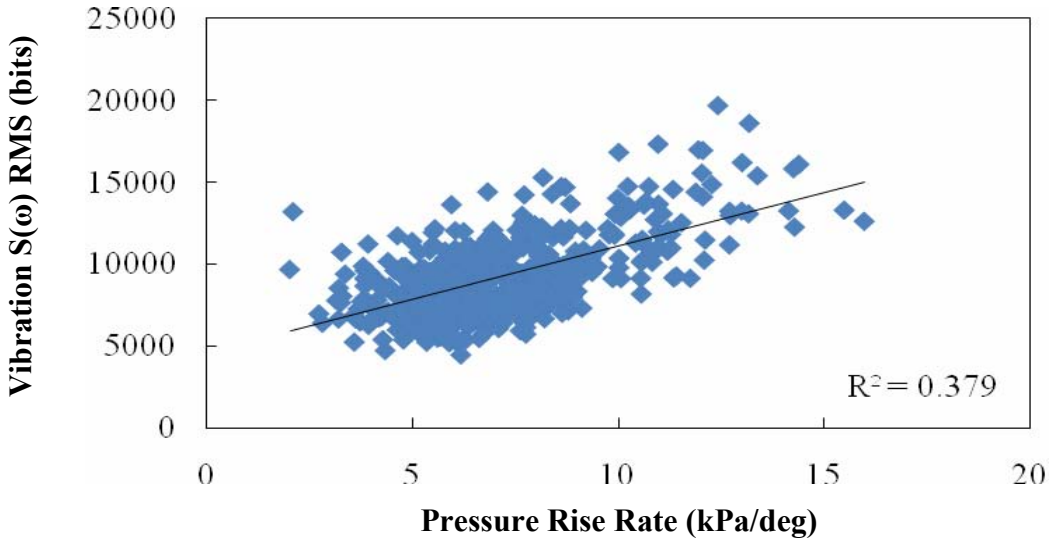

Figure 5.15 Per-cycle flywheel 500 – 700 Hz frequency band structure vibrations as a function of the average PRR (3000 rpm, 231 kPa)

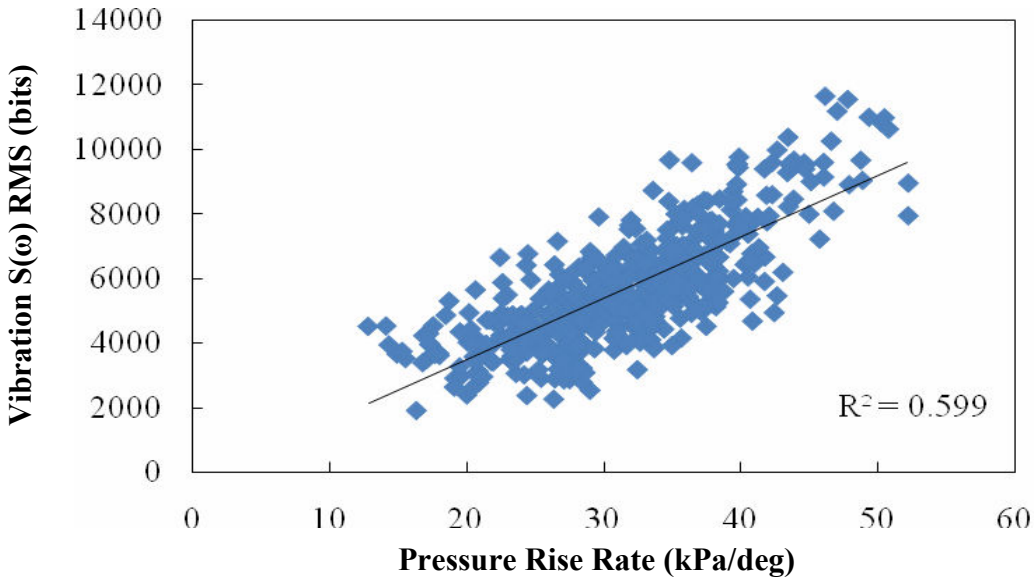

Figure 5.16 Per-cycle flywheel 500 – 700 Hz frequency band structure vibrations as a function of the average PRR (2520 rpm, 533 kPa)

Although the correlation is weaker, the relation between the structure vibrations in the 2000 – 2500 Hz bandwidth of the flywheel, LCW, and UCW locations and the average PRR exhibited interesting results, see Figure 5.17. Since all three locations showed the same trends, only the flywheel data is shown in Figure 5.17. The structure vibration appears to increase with average PRR until approximately 36 kPa/deg at which it begins to level off. The reason for this behavior is unknown and is only seen at the 533 kPa IMEPn load.

The structure vibrations in the 500 – 700 Hz frequency band exhibited a moderate correlation with the average PRR for all accelerometer locations at the 3000 rpm 533 kPa IMEPn engine operating condition, just as was previously seen with the 2520 rpm 533 kPa operating condition. The structure vibrations in the 2000 – 2500 Hz frequency band for the 3000 rpm, 533 kPa IMEPn set point exhibited the same unique behavior with the average PRR for all accelerometer locations as was seen at the 2520 rpm, 533 kPa IMEPn engine set point. However, the R^2 values of the 2000 – 2500 Hz vibrations were at approximately 0.170 thus showing a weak correlation. With the unique relation between the structure vibrations in this frequency band and the average PRR, the lower R^2 values are not surprising.

As the load was increased to 945 kPa IMEPn the correlation between the structure vibrations and the average PRR appeared to be comparable to the 533 kPa IMEPn load. The structure vibrations in the 500 – 700 Hz frequency band showed a moderate correlation to the average PRR, see Figure 5.18. Interestingly, this moderate correlation was only present at the BCW accelerometer location. The flywheel, LCW and UCW accelerometer locations did not exhibit the same moderate correlation or increasing trend.

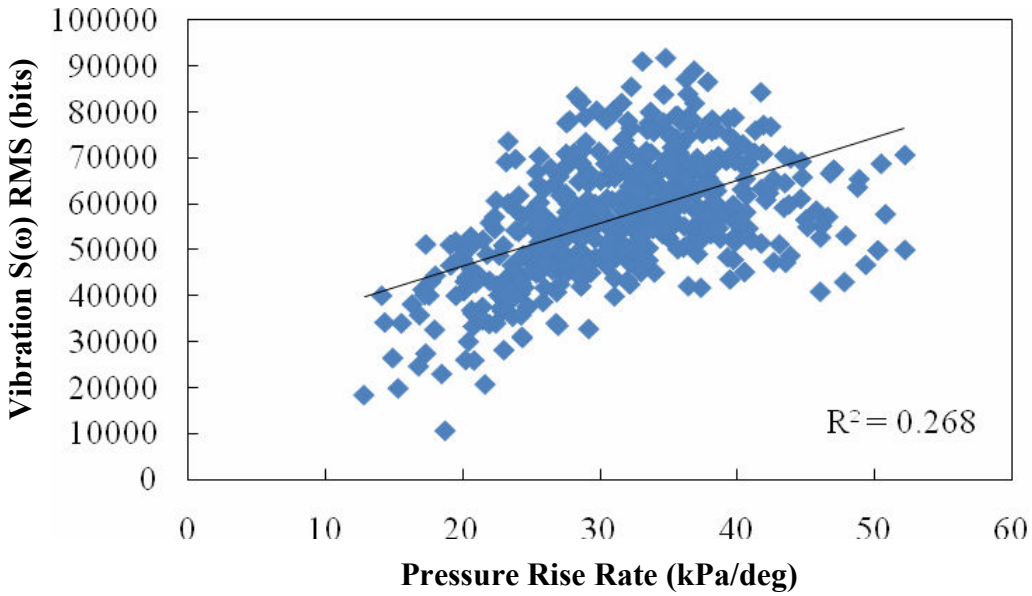

Figure 5.17 Per-cycle flywheel 2000 – 2500 Hz frequency band structure vibrations as a function of the average PRR (2520 rpm, 533 kPa)

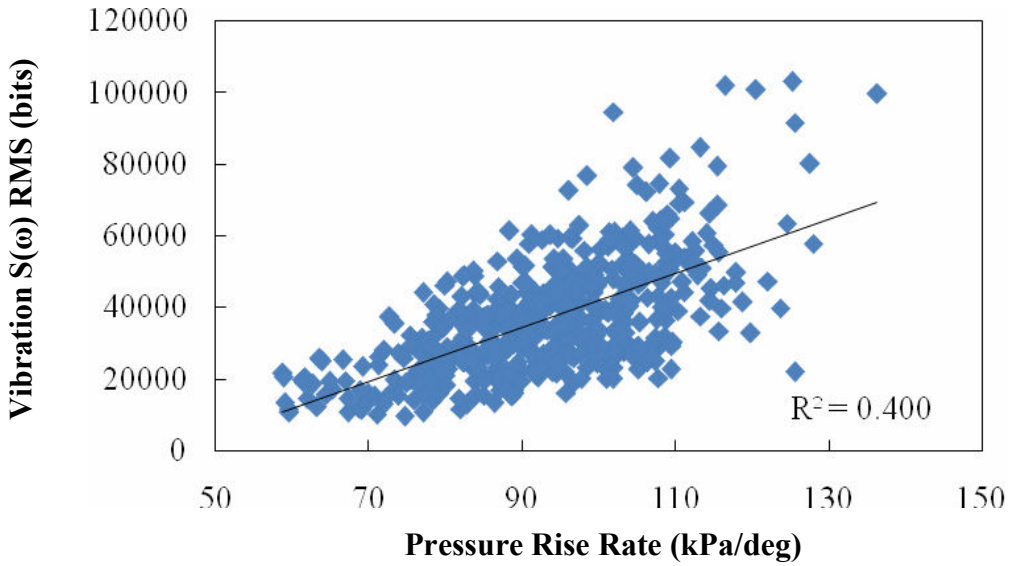

Figure 5.18 Per-cycle BCW 500 – 700 Hz frequency band structure vibrations as a function of the average PRR (2520 rpm, 945 kPa)

Conversely, the structure vibrations in the 2000 – 2500 Hz frequency band at the flywheel, LCW and UCW accelerometer locations showed a strong correlation to the average PRR while the BCW did not, see Figure 5.19.

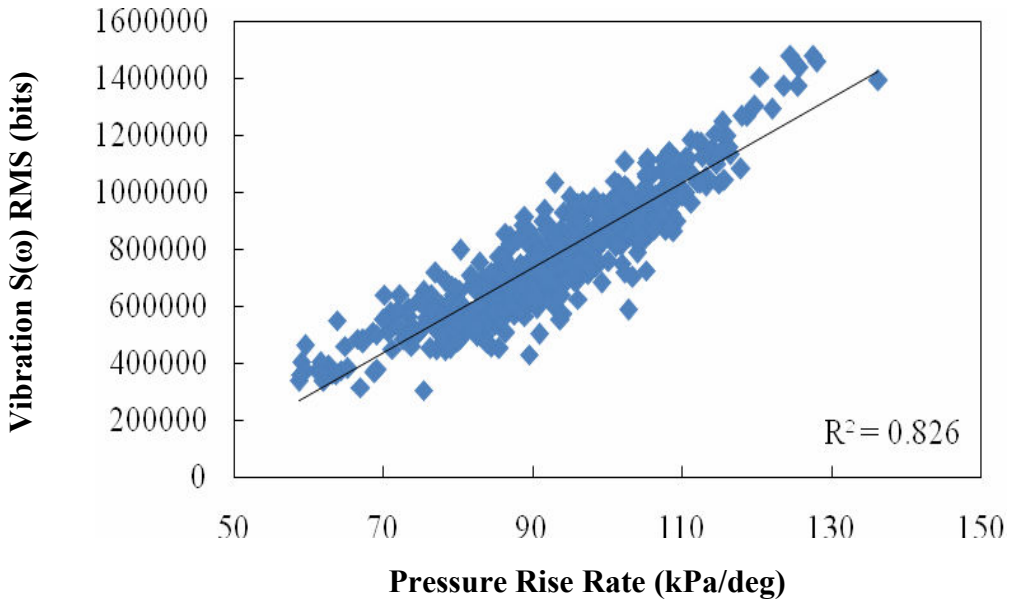

Figure 5.19 Per-cycle flywheel 2000 – 2500 Hz frequency band structure vibrations as a function of the average PRR (2520 rpm, 940 kPa)

At the 3000 rpm, 945 kPa IMEPn set point, the structure vibrations in the 500 – 700 Hz frequency band at the flywheel, UCW, and BCW accelerometer locations exhibited a moderate correlation to average PRR, see Figure 5.20. This correlation is comparable to the 500 – 700 Hz BCW structure vibrations for the 2520 rpm, 945 kPa IMEPn. The LCW accelerometer location at this set point exhibited only a weak correlation between the 500 – 700 Hz structure vibrations and the average PRR.

The structure vibrations in the 2000 – 2500 Hz frequency band for all accelerometer locations at this set point correlated to the average PRR. Figure 5.21

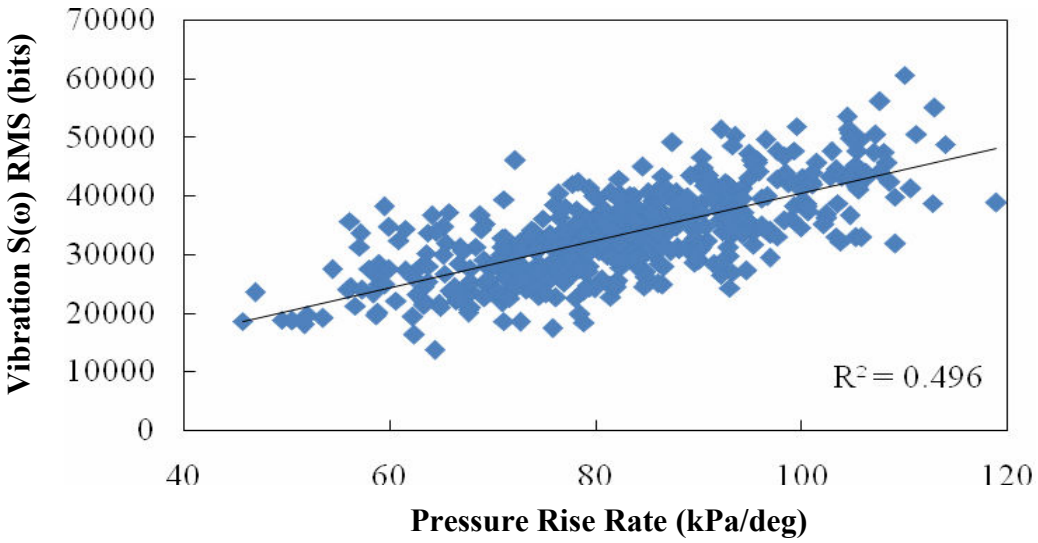

Figure 5.20 Per-cycle BCW 500 – 700 Hz frequency band structure vibrations as a function of the average PRR (3000 rpm, 945 kPa)

shows the 2000 – 2500 Hz structure vibrations as a function of the average PRR for the flywheel accelerometer location. The LCW and UCW accelerometer locations exhibited the same correlations. There is clearly a strong correlation between the structure vibrations and average PRR at this set point. The 2000 – 2500 Hz vibrations at the BCW location exhibited a moderate correlation with the R^2 value being 0.483.

It was apparent the structure vibrations in the 500 – 700 Hz frequency bands exhibited, at best, only a moderate correlation with the average PRR. However, as the load was increased the correlation between the structure vibrations in the 2000 – 2500 Hz frequency band and average PRR increased. This was consistent for the 2520 and 3000 rpm set points, with most accelerometer locations showing increases. It is hypothesized this structure vibration is not a product of combustion or cavity resonances directly, but rather a result of piston slap brought on by the violent release of energy associated with a high average PRR. Further investigation should be conducted to test this hypothesis.

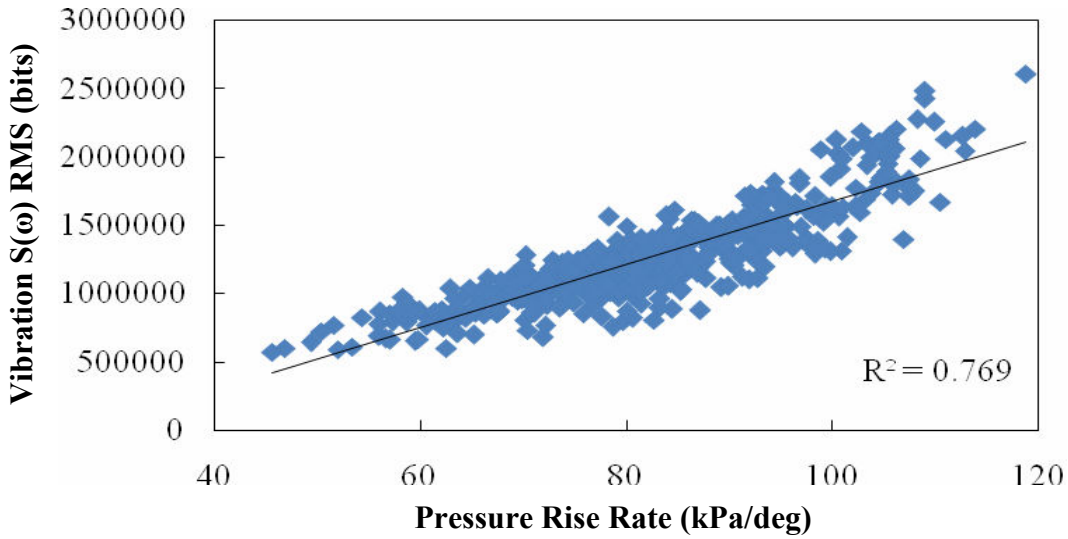

Figure 5.21 Per-cycle flywheel 2000 – 2500 Hz frequency band structure vibrations as a function of the average PRR (2520 rpm, 945 kPa)

From the per-cycle structure vibration results presented, it would be inadequate to use the RMS value of any of the frequency bands analyzed at any accelerometer location to predict the level of PRR of an SI engine undergoing normal combustion operation over a range of engine operating conditions. However, if the current SI engine tested is operating at a mid- to high- load, the 2000 – 2500 Hz frequency band could provide some level of PRR indication.

The per-cycle results do exhibit behavior consistent with the average speed and load comparisons and the direct comparison between the average vibration and PRR levels. Vibration levels at the low speed and load set points provided weak indication of the PRR level. Conversely, vibration levels at the higher speed and load set points provided adequate indication of the level of PRR. Therefore, the ability of vibration

sensing to predict the initial release rate of energy from the combustion process increases with an increase in the initial rate of energy.

5.1.3 Acoustic Results. The structure vibrations analyzed provided little promise of a non-intrusive sensor for indicating the level of PRR of the SI engine under normal combustion operation over a range of speed and load. Therefore, attention was turned to the acoustic emission of the engine. The acoustic data was analyzed with the same comparisons and metrics used in the structure vibration analysis.

5.1.3.1 Set point average speed and load results. As was done for the structure vibration emission, the development of average acoustic emission with speed and load was initially investigated, see Figure 5.22. The acoustic emission exhibited the same trends for the 500 – 700, 2000 – 2500, and 6000 – 6600 Hz frequency bands, however only the 500 – 700 Hz frequency band is shown in Figure 5.22. Note the y-axis is logarithmic due to the large differences in magnitude between each load set point. Interestingly, the average magnitude of the acoustic emission increased with both speed and load in all frequency bands.

Recall that the structure vibrations, in general, increased with both speed and load. Since the acoustic emission will depend on the structure vibrations, these results are not surprising. Also recall the PRR decreased with speed and increased with load. Since the magnitude of the structure vibrations increased with load and was found to become more dependent on PRR with an increase in load, the acoustic emission was expected to follow the same trend.

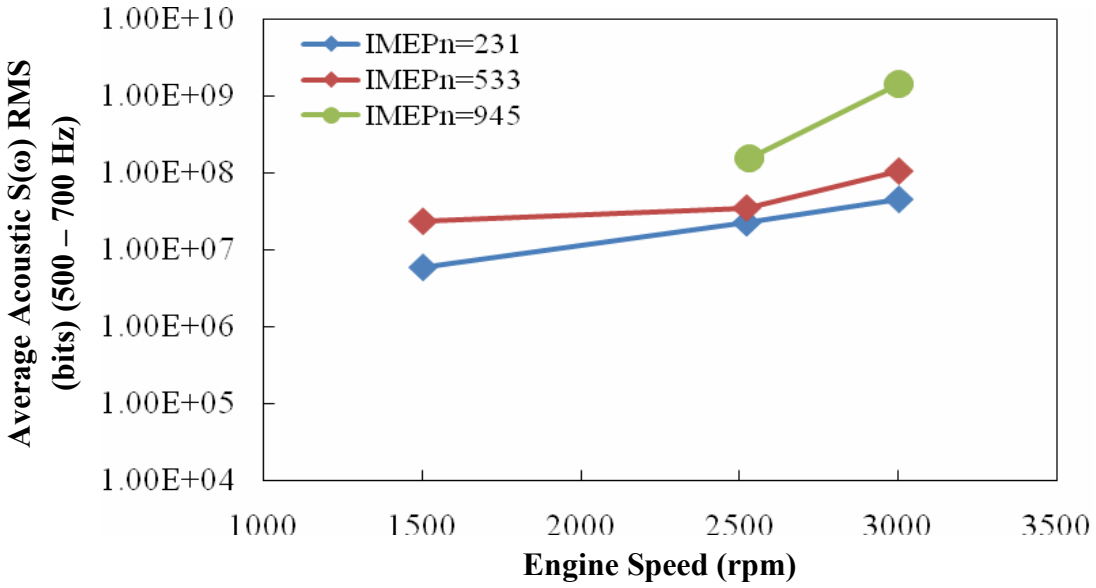

Figure 5.22 Development of acoustic emission (500 - 700 Hz) with speed and load

5.1.3.2 Set point average acoustic emission and PRR comparisons. To investigate the direct relation between the magnitude of acoustic emission in the three frequency bands and the PRR, a 500 engine cycle average of acoustic emission in the 500 – 700 Hz frequency band was plotted as a function of the average PRR at each set point, see Figure 5.23. The set point values from Table 5.1 are shown in Figure 5.23 beside each data marker to identify the engine operating conditions. A comparison of the 500 – 700 Hz acoustic emission and instantaneous PRR is shown in Figure 5.24. The trend is comparable to the trends seen in Figure 5.9 and Figure 5.10 for the structure vibrations. Again, since the acoustic emission will depend heavily on the structure vibrations, the results are not surprising.

Notice in Figure 5.23 and Figure 5.24 the lower load set point markers have less scatter whan what was present in the structure vibration results. This is attributed to the larger scatter in the high load set point markers (set point numbers 5 and 8). It is

apparent the number 5 set point lies more in line with the lower load set points than the number 8 set point. Therefore, the 500 cycle average 500 – 700 Hz acoustic emission was replotted as a function of the average PRR with the number 8 set point excluded, see Figure 5.25. Excluding set point number 8 from the comparison of the 500 – 700 Hz acoustic emission to the instantaneous PRR exhibited the same results as the average PRR and will not be shown. It is much clearer from Figure 5.25 how similar the relation between the acoustic emission and PRR is to the structure vibration and PRR.

The same comparison was made with the 2000 – 2500 Hz acoustic emission and the average and instantaneous PRR, see Figure 5.26 and Figure 5.27, respectively. The comparison of the 6000 – 6600 Hz acoustic emission and PRR followed the same trend and therefore will not be shown. Again, note how similar this is to the structure vibrations.

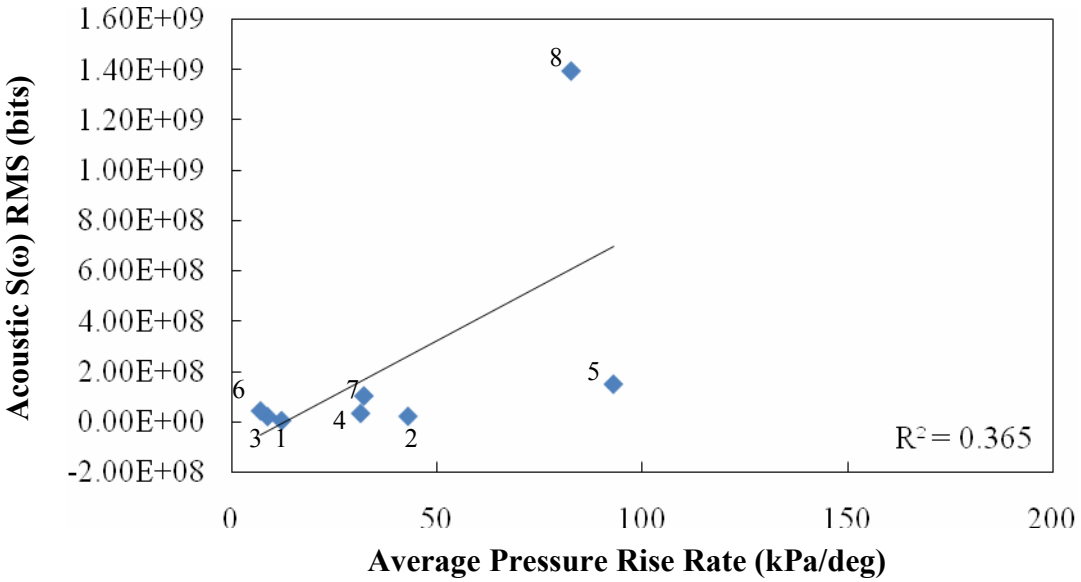

Figure 5.23 A 500 cycle average of the 500 – 700 Hz frequency band acoustic emission RMS as a function of average PRR, each point represents a set point from Table 5.1

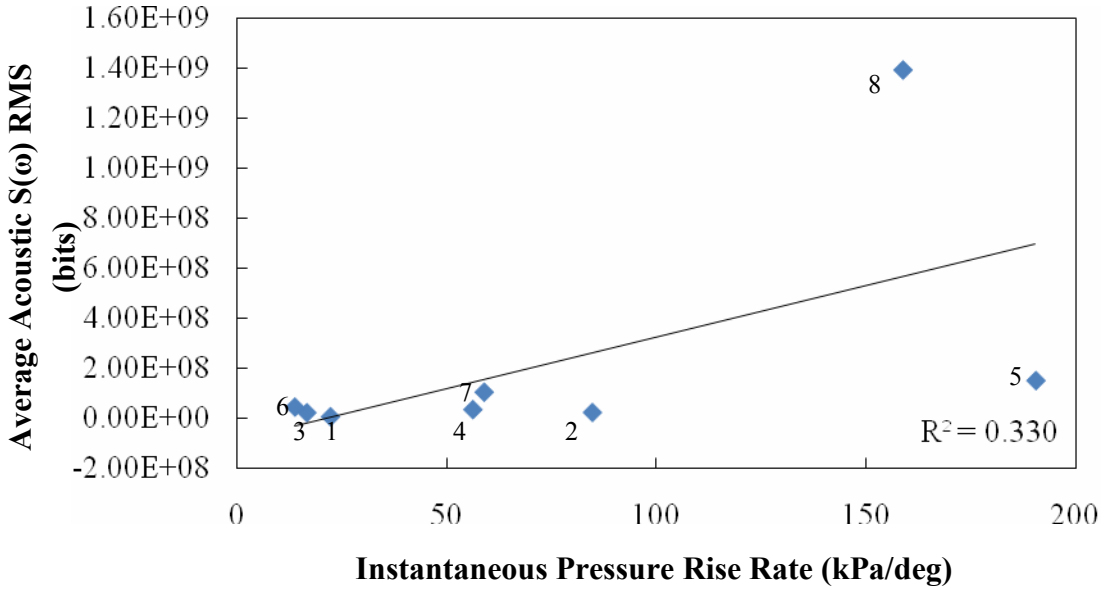

Figure 5.24 A 500 cycle average of the 500 – 700 Hz frequency band acoustic emission RMS as a function of instantaneous PRR, each point represents a set point from Table 5.1

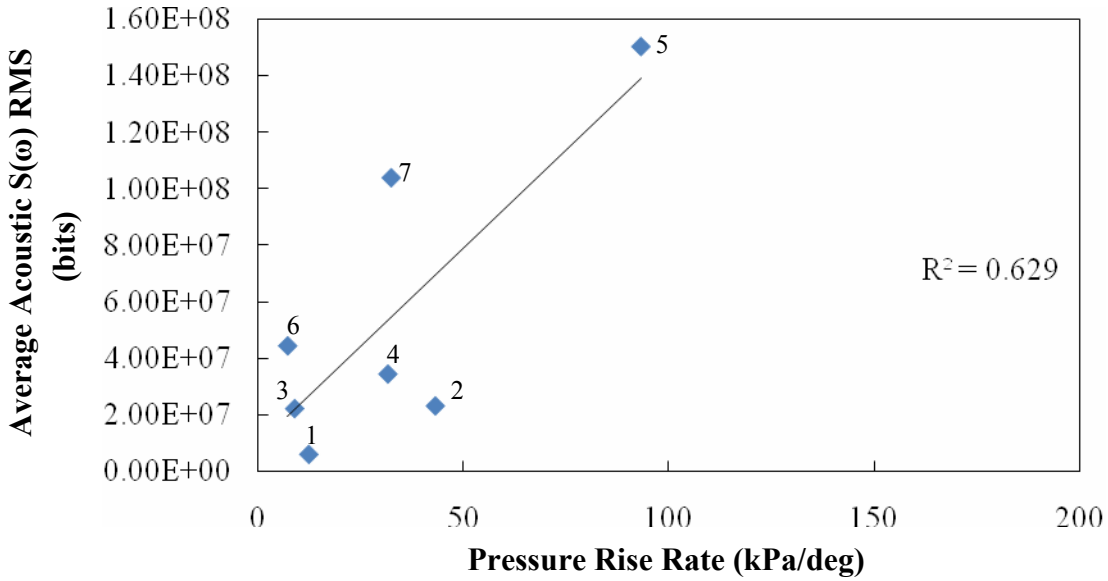

Figure 5.25 A 500 cycle average of the 500 – 700 Hz frequency band acoustic emission RMS as a function of average PRR, excluding set point number 8

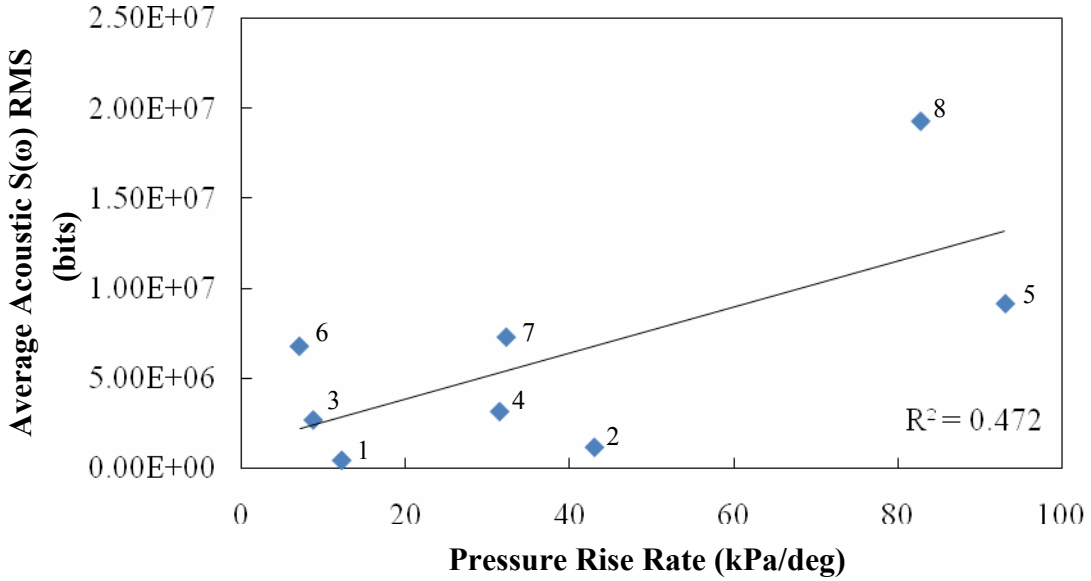

Figure 5.26 A 500 cycle average of the 2000 – 2500 Hz frequency band acoustic emission RMS as a function of average PRR

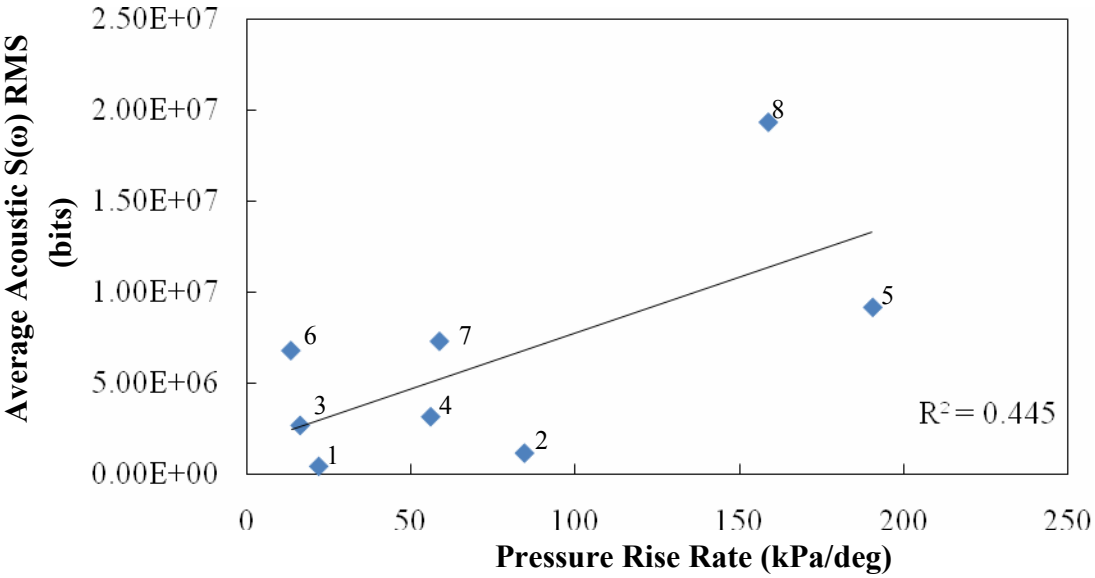

Figure 5.27 A 500 cycle average of the 2000 – 2500 Hz frequency band acoustic emission RMS as a function of instantaneous PRR

At this point it is clear the average magnitude of the acoustic emission in the analyzed frequency bands is increasing with the PRR. By referencing the set point numbers in Figure 5.26 and Figure 5.27, it is evident the engine speed impacts the acoustic emission just as the load does. The general trends indicate it would be sufficient to use the magnitude of the acoustic emission to indicate the level of PRR for an engine operating at constant speed and differing loads. Conversly, the general trends indicate the magnitude of the acoustic emission would be less likely to indicate the level of PRR for a constant load and differing speed engine operating condition. The general trends are unfavorable for using acoustic emission to indicate cylinder PRR, indicating the initial rate of release in energy, for low engine speed and load set points. Converesly and comparable to the vibration results, the trends show the acoustic emission would provide indication of the level of cylinder PRR, and thus the initial release rate of energy from combustion, at higher speed and load set points.

Again, the trends indicate the magnitude of the vibration and acoustic emissions would be less likely to indicate the level of PRR for a constant load and differing speed engine operating condition. Recall the PRR decreased with a change in speed at a given load. As was explained, this was a result of defining the PRR on a crank-angle basis. Therefore, a simple calculation using the engine speed was done to convert the PRR from a crank angle basis to a temporal basis. This conversion in given by the following equation:

$$\mathrm{PRR}\left(\frac{\mathrm{kPa}}{\mathrm{deg}}\right) \times \text{engine speed}\left(\frac{\mathrm{rev}}{\mathrm{min}}\right)\left(\frac{360\ \mathrm{deg}}{1\ \mathrm{rev}}\right)\left(\frac{1\,\mathrm{min}}{60\,\mathrm{sec}}\right) = \mathrm{PRR}\left(\frac{\mathrm{kPa}}{\mathrm{sec}}\right) \tag{5.3}$$

The set point average speed and load results for the vibration and acoustic emissions did not change as a result of this calculation since the PRR was not used. The per-cycle

results did not change as well since they were for a set engine speed. Conversely, the behavior of the PRR with speed and load variations does change, see Figure 5.28. The instantaneous PRR exhibited the same trends and will not be shown.

Instead of a decreasing magnitude with speed, the PRR exhibits a constant to slight increase in magnitude with engine speed. This is not surprising since at a higher engine speed, more engine cycles are being produced in a given amount of time. Therefore, the temporal PRR should increase with increasing engine speed. From these results it was desired to investigate the relation between the set point average vibration and acoustic emissions and the temporal PRR.

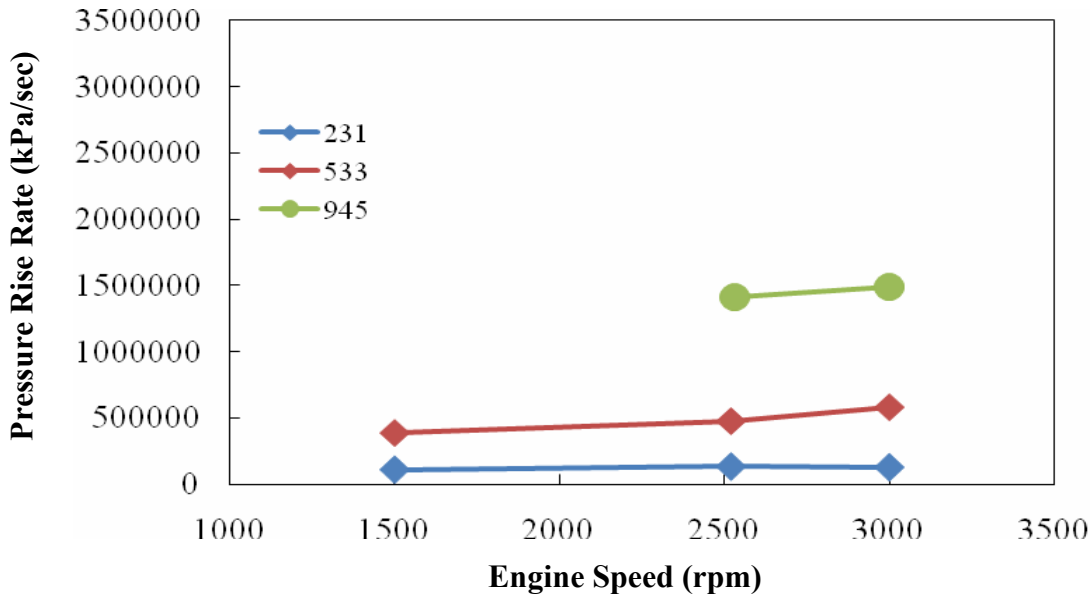

Figure 5.28 Development of average PRR (kPa/sec) with speed and load

The average structure vibration levels for the 500 - 700 Hz frequency band at the LCW accelerometer location are shown in Figure 5.29. This is the same average structure vibrations plotted in Figure 5.9. Notice the correlation coefficient (R^2) has a higher value indicating a stronger relation between the structure vibrations and the temporal average PRR. The structure vibrations in the 2000 – 2500 and 6000 – 6600 Hz frequency bands were also compared to the temporal average PRR, see Figure 5.30. All accelerometer locations exhibited the same trends in both frequency bands and therefore only the 2000 – 2500 Hz structure vibrations for the LCW accelerometer location will be shown. Again the structure vibrations exhibited a very strong correlation to the temporal PRR. The acoustic emissions also showed better correlations to the temporal PRR than the crank-angle PRR for set point average comparisons.

These results are significant in that they allude to analyzing the cylinder pressure on a temporal basis rather than crank-angle. The vibration and acoustic emissions are heavily time dependant, i.e. resolving the spectral content of the signal is based upon the accurate time representation of the waveforms. Therefore, it is conceivable the cylinder pressure may need to analyzed on a temporal basis; however this should be investigated further before final conclusions are drawn.

5.1.3.3 Per-cycle results. With the general trends of the acoustic emission results being comparable to those of the previous vibration results, it was desired to investigate the relation of acoustic emission and PRR on a cycle-to-cycle basis. Therefore the per-cycle acoustic data was analyzed in the same manner as the structure vibration data. An RMS value for the power spectrum in the 500 – 700, 2000 – 2500, and 6000 – 6600 Hz

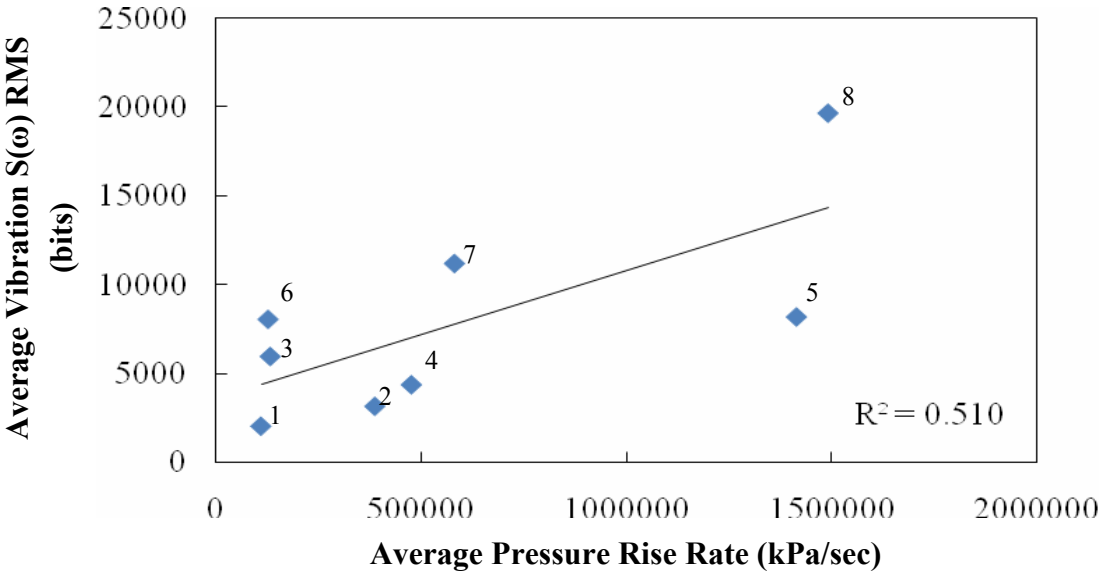

Figure 5.29 A 500 cycle average of LCW 500 – 700 Hz frequency band structure vibration RMS as a function of average PRR, each point represents a set point from Table 5.1

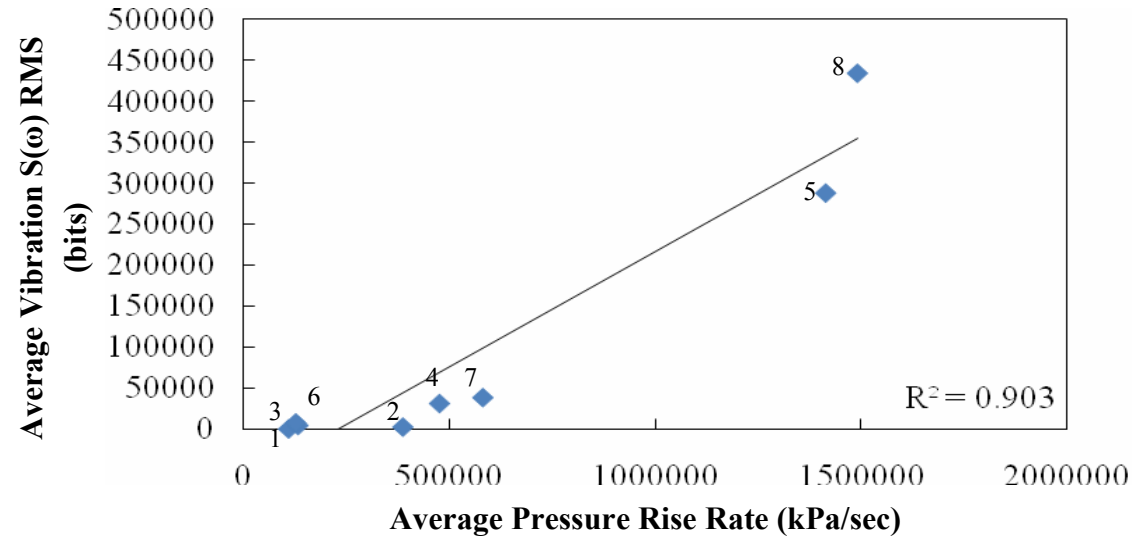

Figure 5.30 A 500 cycle average of LCW 2000 – 2500 Hz frequency band structure vibration RMS as a function of average PRR, each point represents a set point from Table 5.1

frequency bands were calculated on a per-engine-cycle basis. For each set point, the acoustic RMS values were compared to the per-cycle PRR.

Analysis began with the per-cycle acoustic emission in the 500 – 700 Hz frequency band compared to per-cycle average PRR for set point number 1 (1500 rpm, 231 kPa IMEPn), see Figure 5.31. It is clear no trend exists between the per-cycle acoustic emission in this frequency band and the average PRR at this engine set point. In fact the acoustic emission in the 2000 – 2500 and 6000 – 6600 Hz frequency bands at this set point also showed no relation to the average PRR. The acoustic emission in all three frequency bands analyzed showed no relation to the instantaneous PRR at this set point as well. In fact, no trend between the instantaneous PRR and the acoustic emission in any frequency band analyzed was found at any engine operating condition. Also, no trend was seen between the acoustic emission in the 6000 – 6600 Hz frequency band and the average PRR at any engine set point.

For the low load (231 kPa IMEPn) engine operating condition, no trend was seen between the acoustic emission in any frequency band and the average PRR at any engine speed. For the mid-load (533 kPa IMEPn) engine operating, no trend was seen between all acoustic emission frequency bands analyzed and the average PRR at the engine speeds of 1500 and 3000 rpm.

Interestingly, the acoustic emission in the 500 – 700 Hz frequency band at the 2520 rpm, 533 kPa set point showed a slight increasing trend with an increase in average PRR, see Figure 5.32. The correlation coefficient is small and would be considered a weak correlation, however the increasing acoustic emission trend is identifiable. The 2000 – 2500 Hz frequency band did not exhibit such a trend at this operating set point.

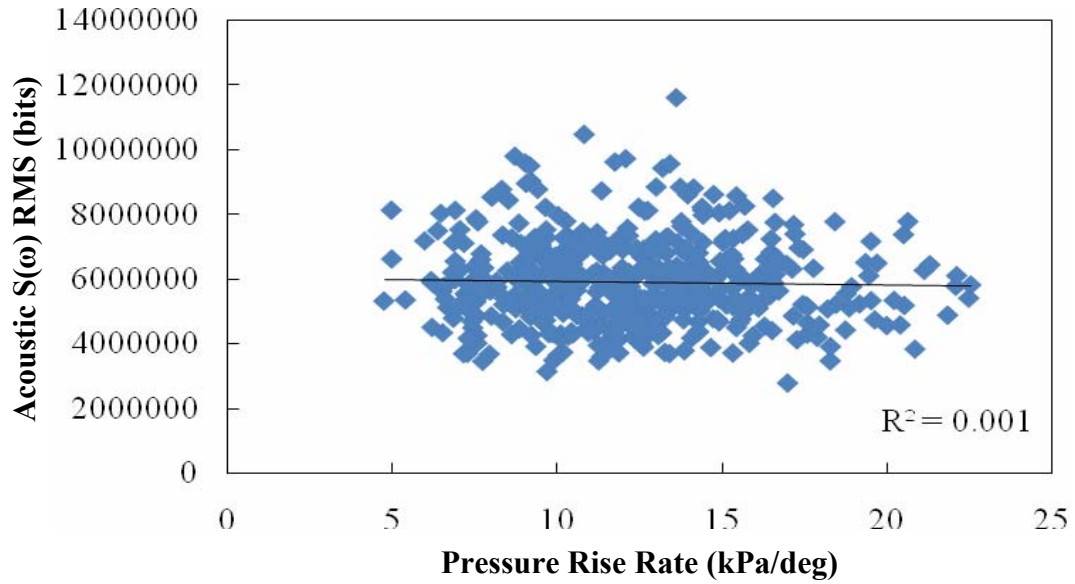

Figure 5.31 Per-cycle 500 – 700 Hz frequency band acoustic emission as a function of the average PRR (1500 rpm, 231 kPa)

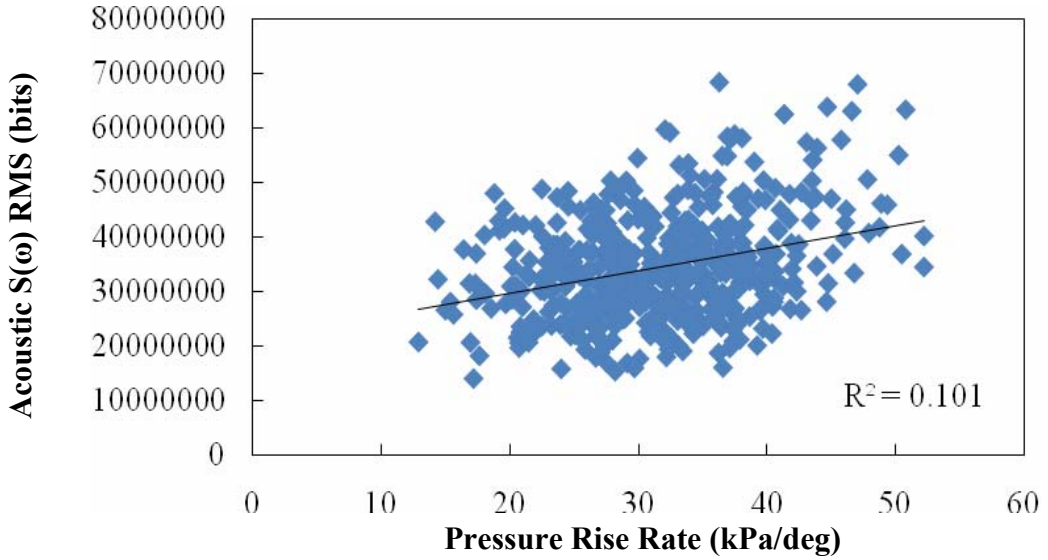

Figure 5.32 Per-cycle 500 – 700 Hz frequency band acoustic emission as a function of the average PRR (2520 rpm, 533 kPa)

The high-load (945 kPa IMEPn) engine operating condition, exhibited much stronger trends than was previously seen at the light- and mid-load engine set points. These results are consistent with those seen in the initial experiments. The 2520 rpm speed set point showed an increase in acoustic emission in the 500 – 700 Hz frequency band as the average PRR increased, see Figure 5.33. However, the increasing trend was not as noticeable for the 2000 – 2500 Hz frequency band, see Figure 5.34. The acoustic emission in the 2000 – 2500 Hz bandwidth shows a near constant magnitude for average PRR values below approximately 100 kPa/deg. However, once this average PRR value is reached, an increasing trend in the acoustic emission is noticed. The reason for this behavior is unclear as it is not in absolute agreement with the initial experimental results. The same increasing trends were seen for the 3000 rpm, 945 kPa IMEPn set point, see Figure 5.35 and Figure 5.36. Notice for the 2000 – 2500 rpm frequency band, see Figure 5.36, the increase in acoustic emission with average PRR is much more pronounced for the 3000 rpm engine speed.

Comparable to the structure vibration results, the acoustic emission also provided a weak indication of cylinder PRR at low speed and load engine operating conditions. Interestingly, if the speed was held constant and the load was varied, the average acoustic emission in all three frequency bands provided indication of the average cylinder PRR. The acoustic emission in the 6000 – 6600 Hz frequency band representing the cavity resonant mode would be a poor indicator of per-cycle average PRR at any engine operating condition.

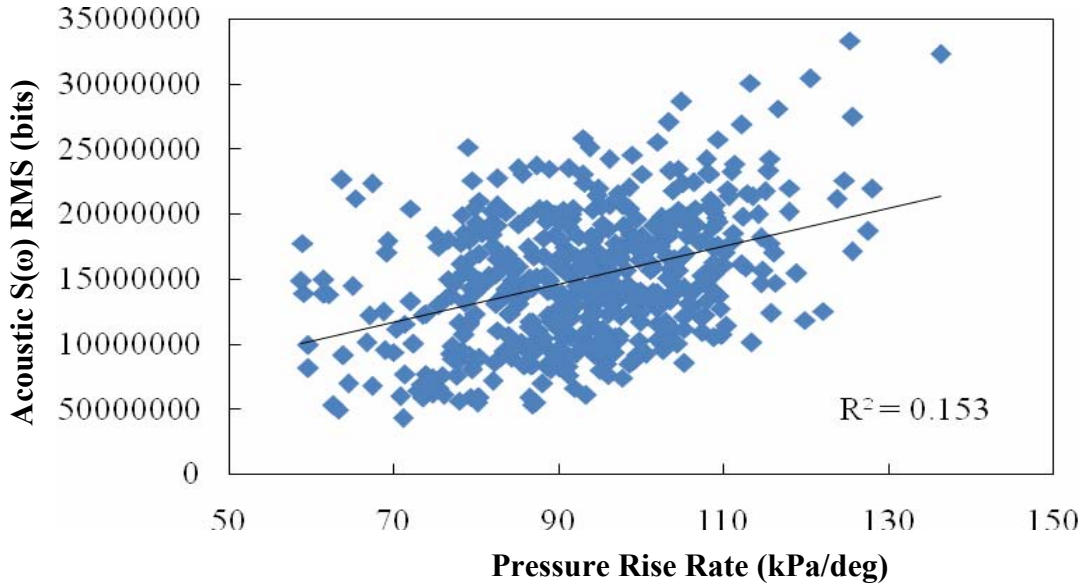

Figure 5.33 Per-cycle 500 – 700 Hz frequency band acoustic emission as a function of the average PRR (2520 rpm, 945 kPa)

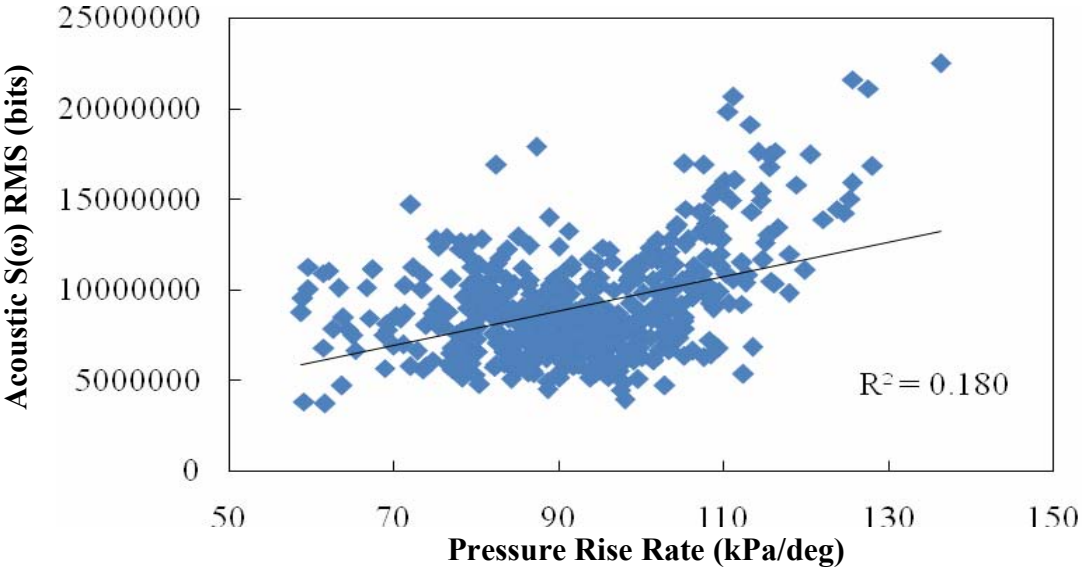

Figure 5.34 Per-cycle 2000 – 2500 Hz frequency band acoustic emission as a function of the average PRR (2520 rpm, 945 kPa)

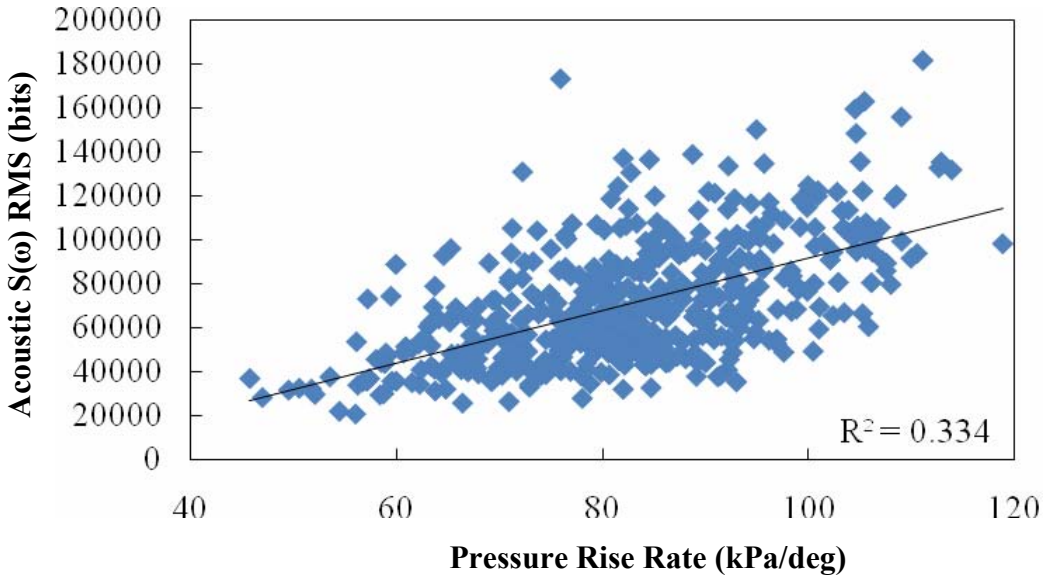

Figure 5.35 Per-cycle 500 – 700 Hz frequency band acoustic emission as a function of the average PRR (3000 rpm, 945 kPa)

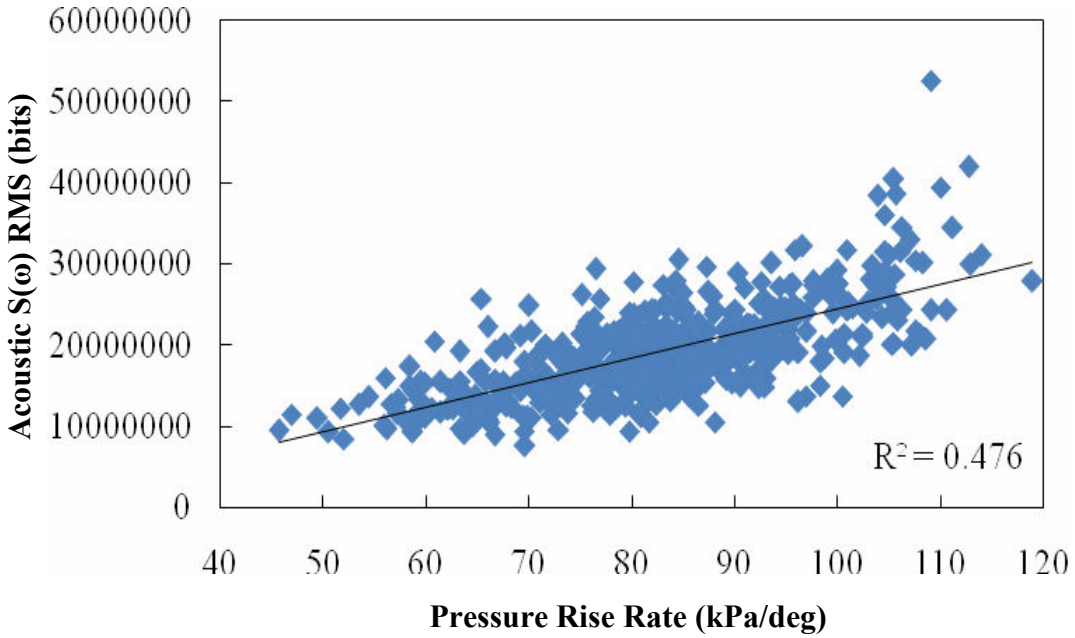

Figure 5.36 Per-cycle 2000 – 2500 Hz frequency band acoustic emission as a function of the average PRR (3000 rpm, 945 kPa)

The results from the vibration and acoustic emissions are significant in that they show for increases in cylinder PRR, the ability of the non-intrusive sensing techniques are able to indicate the level of initial energy release. The set point average comparisons clearly showed an increase in sensitivity between the level of the vibration and acoustic emissions and the cylinder PRR with an increase in speed. These comparisons also showed the magnitude of the vibration and acoustic emissions increased with load at a given speed set point. Per-cycle comparisons between the vibration and acoustic emissions and the cylinder PRR showed the vibration and acoustic emission levels increased with an increase in PRR at higher speed and load set points. From these results, it was concluded the non-intrusive sensing techniques are able to indicate the level of the initial rate of energy release for higher speed and load operating conditions in the SI engine.

One possible reason for the greater response of the vibration and acoustic emissions to higher load is simply from the greater release in energy occurring during the engine cycle. There are two major vibration and acoustic energy generating mechanisms in an internal combustion engine, mechanical component interaction and combustion. Examples of mechanical component interaction would be valve opening and closing events, crankshaft/bearing interactions, and etc. At a given speed, the energy released from mechanical component interaction, will generally, remain constant with increases in load. Combustion generated vibration and acoustic energy is less understood but would result in higher pressure wave amplitudes in the cylinder when load is increased. Greater pressure wave amplitudes, and thus energy, released from the combustion process results in more energy transmitted through the vibration and acoustic transmission paths. The

higher load set points are releasing more energy and therefore raising the vibration and acoustic emissions related to combustion energy released to levels much greater than that of the mechanical component interactions.

5.2 CI ENGINE INVESTIGATION

The combustion process in a diesel engine can, at times, be characterized by having an initial rapid partial burning of the combustion products followed by a slow burning of the remaining fuel/air mixture. This is typical of a fuel injection scheme involving both a pilot and main injection. The result is a cylinder pressure trace involving two humps, which does not lend itself to a simple linear regression between SOC and peak cylinder pressure for estimating an average PRR. The investigation conducted at the NTRC was heavily focused on the changes in structure vibrations resulting from changes in the combustion process. To achieve different types of combustion at constant speed and load, fuel injection type (e.g. pilot + main or main only) was varied to modify the combustion process. The timing of peak pressure and start of combustion for each cycle varied dramatically for each parameter change, see Table 5.2 for parameter variations. Time did not permit developing methods of analysis to estimate an average pressure rise rate value which accounted for the combustion variations, therefore only the instantaneous pressure rise rate was used in comparisons for this investigation.

The original structure vibration waveform was digitally filtered using the SPTool function in MATLAB. A 23 order least-squares direct-form finite impulse response (FIR) filter was designed and implemented with a pass band of 5.0 – 8.0 kHz. This filter

exhibited good impulse and step response which was important for the dynamic structure vibration signal. Specifications and a MATLAB m-file for the filter can be found in Appendix B.

Five engine cycles were recorded for each file listed in Table 5.2 at a constant speed and load of 1500 rpm and 37.3 N-m, respectively. The values listed in Table 5.2 are for cylinder 1. The remaining three cylinders were operated with a pilot and main injection having SOI timings of -18.2 and -2 CAD ATDC, respectively. Pressure data was collected from cylinder 1 only, therefore the net indicated mean effective pressure (IMEPn) was used as a metric to compare the work output from cylinder 1.

Table 5.2 CI engine operating conditions

File Number	Cylinders Firing	EGR dilution*	Pilot Injection (ATDC)	Main Injection (ATDC)	IMEPn (kPa)
0	All	Normal	-18.2	-2	389
1	2,3,4	Normal	-18.2	-2	-33
2	1,3,4	Normal	-18.2	-2	395
10	All	Normal	-	-2	271
11	All	Normal	-	-5	310
12	All	Normal	-	-7	318
13	All	Normal	-18.2	-2 (cylinder 1 off)	17

***EGR Dilution value of Normal is equivalent to 20% dilution by volume of intake air**

To limit influences from other cylinders for which no combustion data was available, comparison of the structure vibration and combustion characteristics was performed from -20 to 40 CAD ATDC during each engine cycle of cylinder 1. For the following results, comparisons were conducted by scatter plots using 5 cycle average

vibration RMS and peak instantaneous pressure rise rate values. Also, per cycle vibration RMS values and peak instantaneous pressure rise rate values were compared and will be presented. This provided approximately 35 cycles of various combustion types to compare.

A five cycle average RMS value was calculated for the cavity resonant frequency band of the structure vibration, characterized by the 5.0 – 8.0 kHz frequency band. The peak instantaneous PRR value was determined from the first order numerical pressure derivative. A scatter plot was constructed comparing the two data sets to determine any correlation between the two calculated metrics, see Figure 5.37. The numbers beside each data point represents which file average the point represents. Initially, no linear correlation between all per file average points was determine.

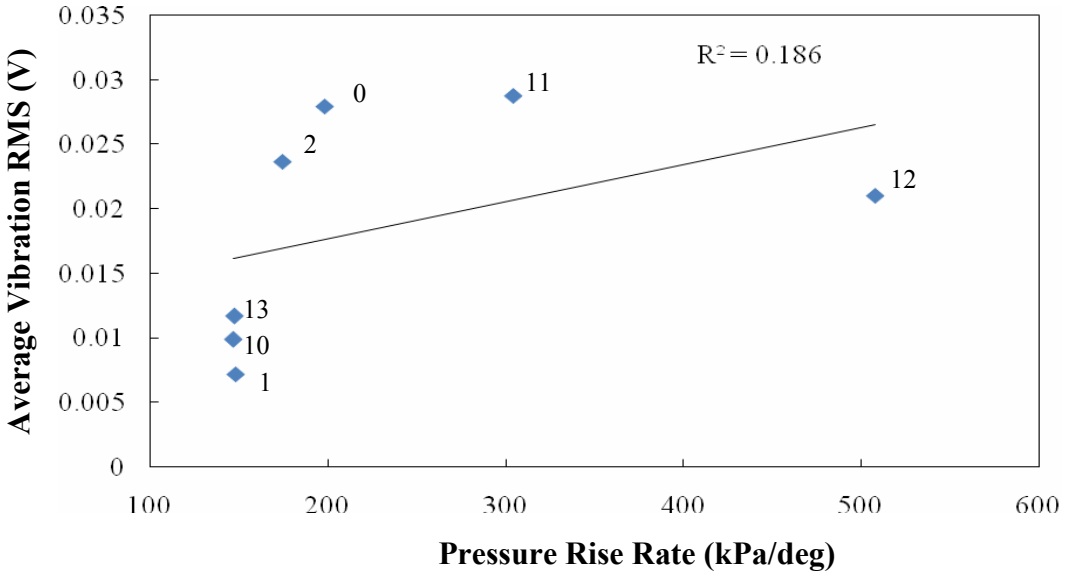

Figure 5.37 Per-file average cavity resonant frequency band structure vibrations as a function of peak instantaneous PRR

Interestingly, when the average file 12 point was thrown out, the correlation became stronger, see Figure 5.38. File 12 consisted of a main only fuel injection event timed at -7° ATDC. This moderate correlation suggests the overall level of PRR could be predicted from the level of vibration of the cavity resonant frequency for the CI engine.

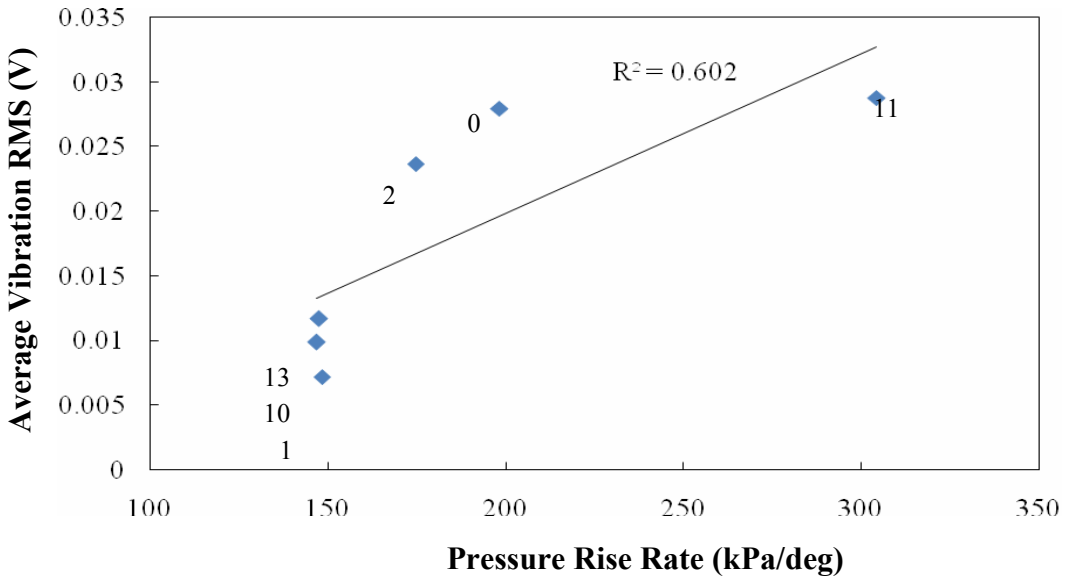

Figure 5.38 Per-file average cavity resonant frequency band structure vibrations as a function of peak instantaneous PRR, **excluding file 12**

In order to investigate prediction of PRR level on a cycle to cycle basis, the cavity resonant frequency structure vibration level RMS and the peak instantaneous PRR were compared, see Figure 5.39. Each set of file data is represented by a different character facilitating determination of trends with combustion type. File 12 has been omitted just as in Figure 5.38. Interestingly, no apparent trend is seen for the per cycle comparisons. The low work output combustion types (i.e. low IMEPn), resulting in low PRR values

(file's 1 and 13), exhibit very little scatter with low structure vibration response. As the work output increases (IMEPn > 300), the scatter becomes much greater for each file, but not in a linear fashion. File 11 has a lower IMEPn than file's 0 and 2; however it has a higher standard deviation from the mean. This is most likely a result of the main only fuel injection combustion type. Referring back to Table 5.2, file's 0 and 2 are combustion initiated with a pilot injection followed by a main injection while file 11 has only a single main injection.

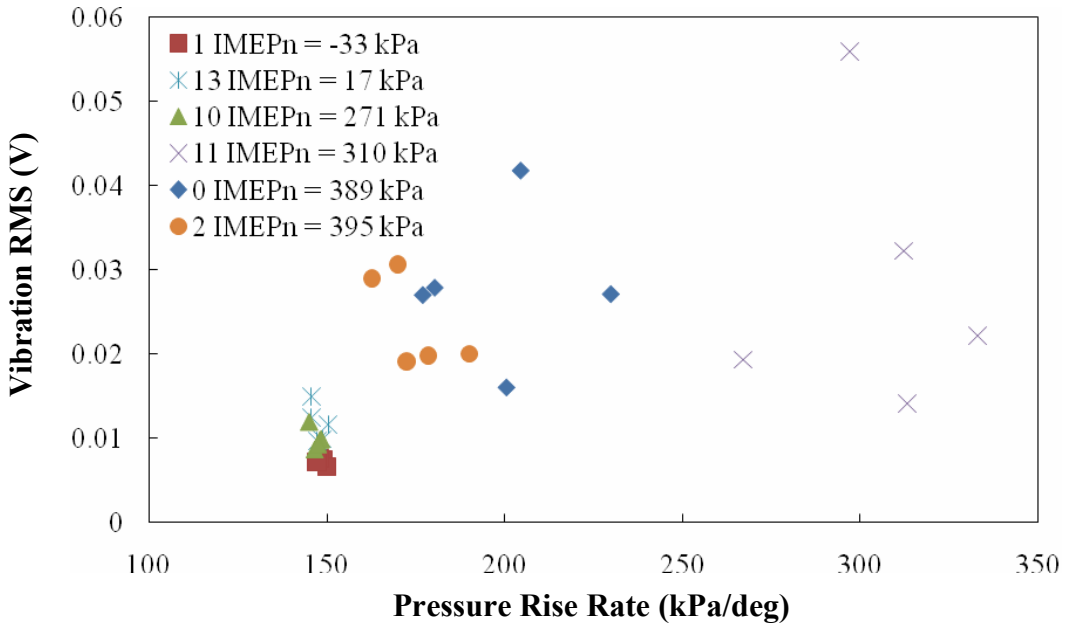

Figure 5.39 Per-cycle cavity resonant structure vibrations plotted as a function of peak instantaneous PRR, **excluding file 12**

The five cycle average cylinder pressure traces for file's 0, 2, and 11 along with the motored trace were plotted to better understand the development of cylinder pressure with relation to injection type, see Figure 5.40. File's 0 and 2 have the same injection

parameters resulting in a near identical pressure trace. The pilot injection causes combustion to begin at approximately -6 CAD ATDC, after the main injection event, the pressure undergoes another increase at approximately 6 CAD ATDC. File 11 has only a main injection at -5 CAD ATDC resulting in combustion not being initiated until ATDC and therefore the first section of the pressure diagram follows the motored cylinder pressure trace. Eventually the fuel/air mixture ignites and causes a spike in the pressure, comparable to file's 0 and 2. Notice the magnitude of file 11 is below the magnitude of file's 0 and 2, explaining the decrease in IMEPn.

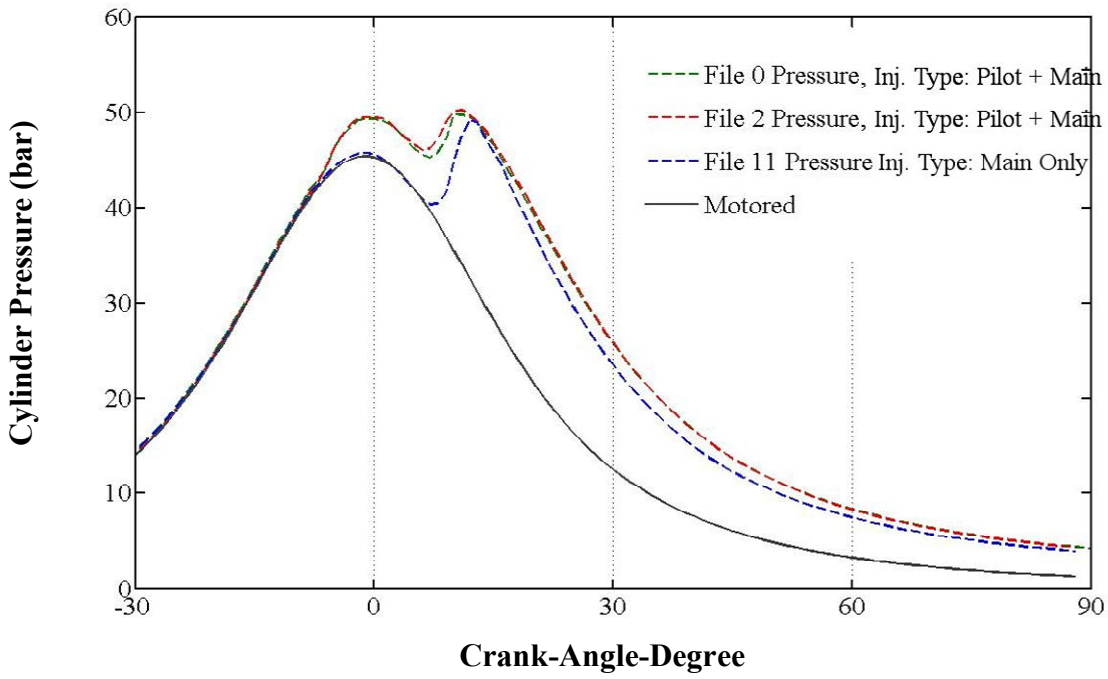

Figure 5.40 Comparison of the cylinder pressure development with varying injection parameters

Investigation of a five cycle average first order pressure derivative was conducted to understand the effect of varying injection parameters on the instantaneous PRR, see Figure 5.41. Since file 0 and file 2 had essentially the same cylinder pressure development, only file 2 and file 11 were compared, see Figure 5.41. Cycles initiating combustion with a pilot injection exhibits an initial peak in the instantaneous PRR before top-dead-center (BTDC). Conversley, for a main only injection, the peak instantaneous PRR occurs after top-dead-center (ATDC).

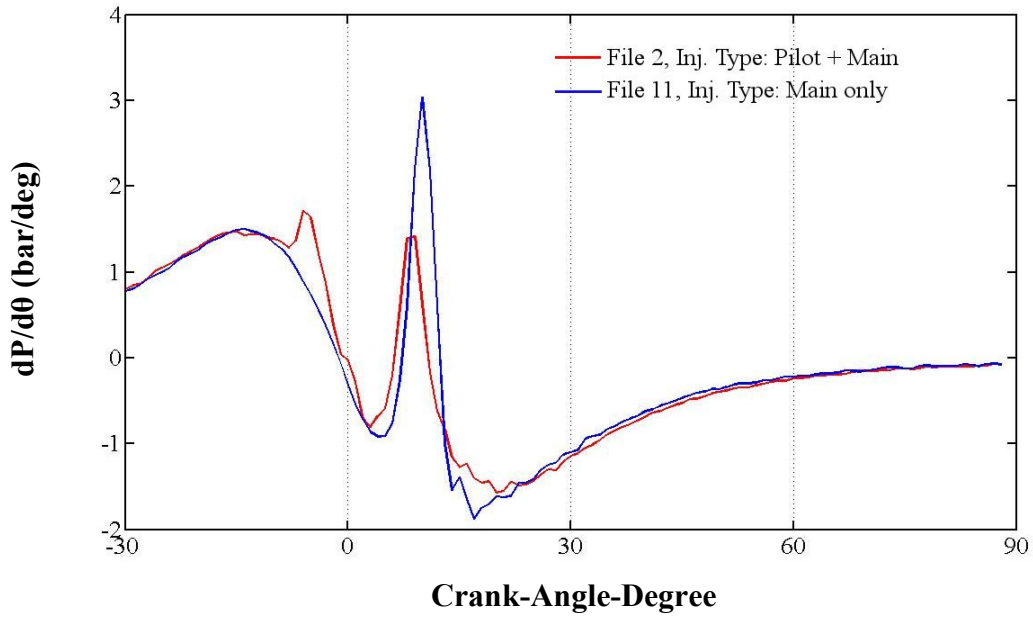

Figure 5.41 First numerical derivative (representing the instantaneous PRR) of the cylinder pressure

After investigating the development of the cylinder pressure and instantaneous PRR, it was desired to segment the cycle in-order to seperate structure vibrations resulting from the combustion initiated by the pilot and the second cylinder pressure

increase initiated, most likely, from the main injection. Therefore, the cavity resonant 5.0 – 8.0 kHz filtered structure vibration waveform was plotted along with the cylinder pressure to examine the development of the structure vibration with pressure changes, see Figure 5.42. For file's 0 and 2, the top waveforms, the 5.0 – 8.0 kHz band begins to increase at approximately -6 CAD ATDC. Next, there is a single energy increase just ATDC and, finally, a large increase of energy that occurs with the second cylinder pressure increase. For file 11, the bottom waveforms, the energy in the 5.0 – 8.0 kHz frequency band has a small increase just ATDC then a large energy increase accompanying the second increase in the cylinder pressure resulting from combustion. Therefore it was decided to split the cycle into two segments: 1.) -10 – 0 CAD ATDC, and 2.) 1 – 40 CAD ATDC. Investigation into the relation of the cavity resonant

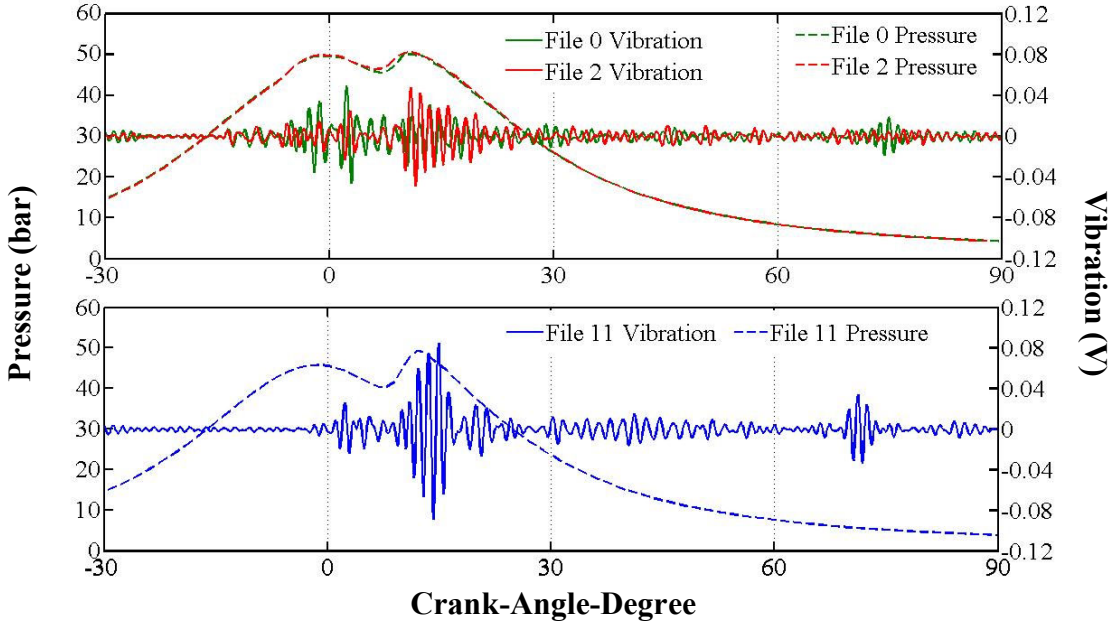

Figure 5.42 Comparison in the development of filtered structure vibrations for differing injection parameters

frequency structure vibration and the instantaneous PRR for each segment will be conducted. This cycle segmentation was implemented for cycles that contained pilot + main and main only injections. It was assumed that if, for example, only a main injection is used at -5° ATDC and SOC occurs after TDC, then the vibrations occurring before TDC will be minimal. This should strengthen any correlations between the cavity resonant frequency structure vibrations and instantaneous PRR.

Initially, a five engine cycle average of the 5.0 – 8.0 kHz filtered structure vibrations were compared to the peak instantaneous PRR for the two time segments, see Figure 5.43 and Figure 5.44. File 12 was included in the following results. For the first segment (-10 – 0 CAD), there appears to be a moderate-high linear correlation, determined by the R^2 value, between the cavity resonant frequencies, characterized by the 5.0 – 8.0 kHz vibration RMS, and the level of peak instantaneous PRR. Interestingly, for the second cycle segment (1 – 40 CAD), the strength of the linear correlation decreases, yet maintains a linear trend.

Per-file average comparisons indicated a relation between the cavity resonant frequencies and the level of peak instantaneous PRR, but, it was desired to investigate this relation on a per cycle basis. Interestingly, for the first cycle segment, the relation remained moderate-high, see Figure 5.45. However, the second cycle segment did not exhibit this same relation, Figure 5.46.

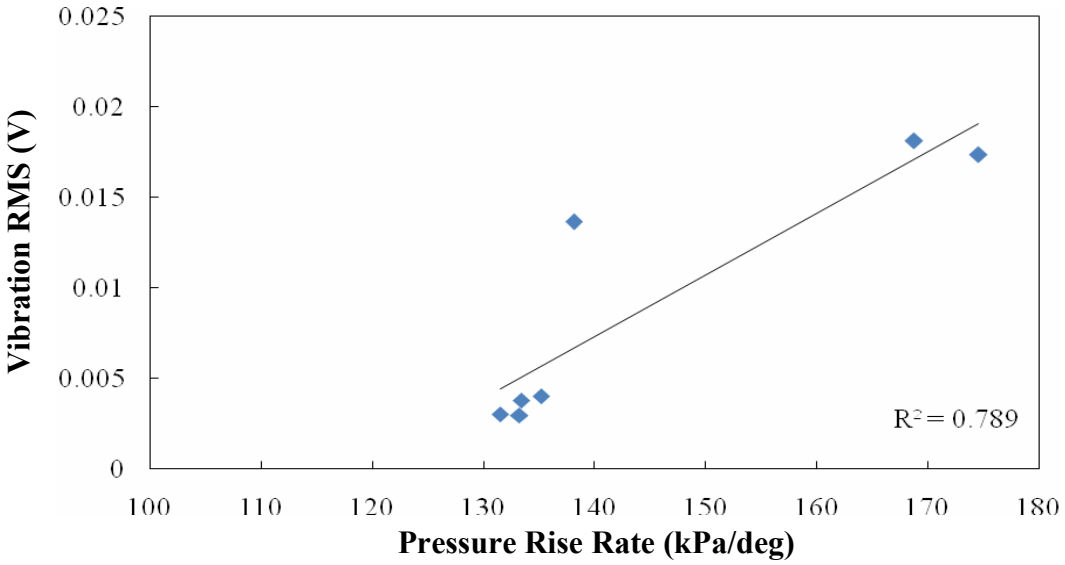

Figure 5.43 Per-file average 5-8 kHz filtered structure vibration as a function of peak instantaneous PRR (-10 - 0 CAD)

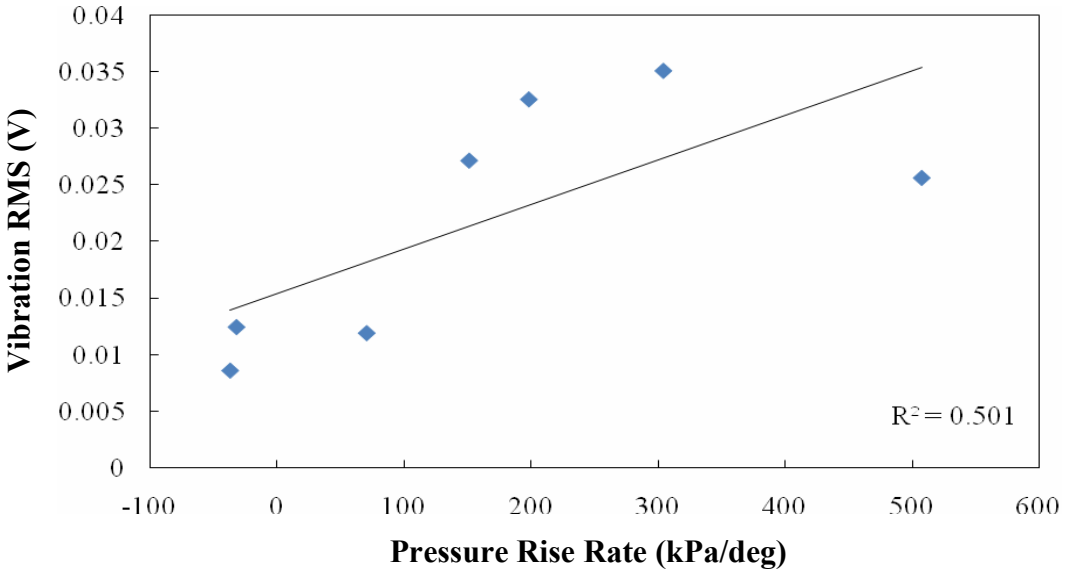

Figure 5.44 Per-file average 5-8 kHz filtered structure vibration as a function of peak instantaneous PRR (1 - 40 CAD)

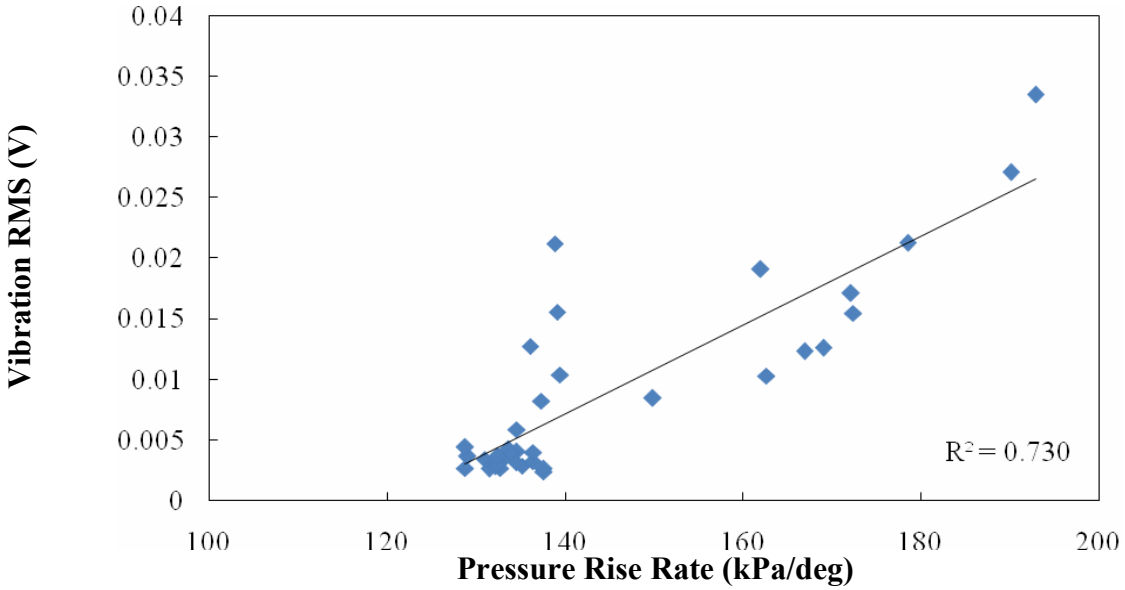

Figure 5.45 Per-cycle 5-8 kHz filtered structure vibration as a function of peak instantaneous PRR (-10 - 0 CAD)

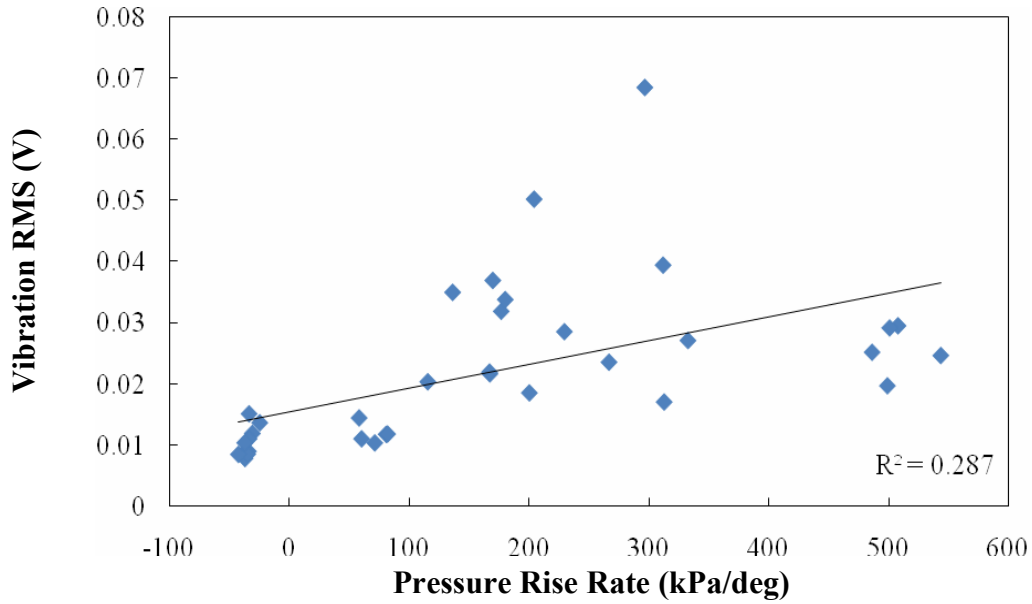

Figure 5.46 Per-cycle 5-8 kHz filtered structure vibration as a function of peak instantaneous PRR (1 - 40 CAD)

Since the five cycle average comparisons exhibited moderate-high correlations, the data from both cycle segment comparisons were combined on one plot to investigate consistency of this correlation, see Figure 5.47. This comparison showed the relation does not exhibit consistency between the two segments. Due to the low number of cycles investigated, it is premature to make definite conclusions. Nevertheless, the preliminary results suggests a cavity resonant frequency structure vibration RMS value may indicate, to some degree, the level of peak instantaneous PRR for engines operating under auto-ignited combustion.

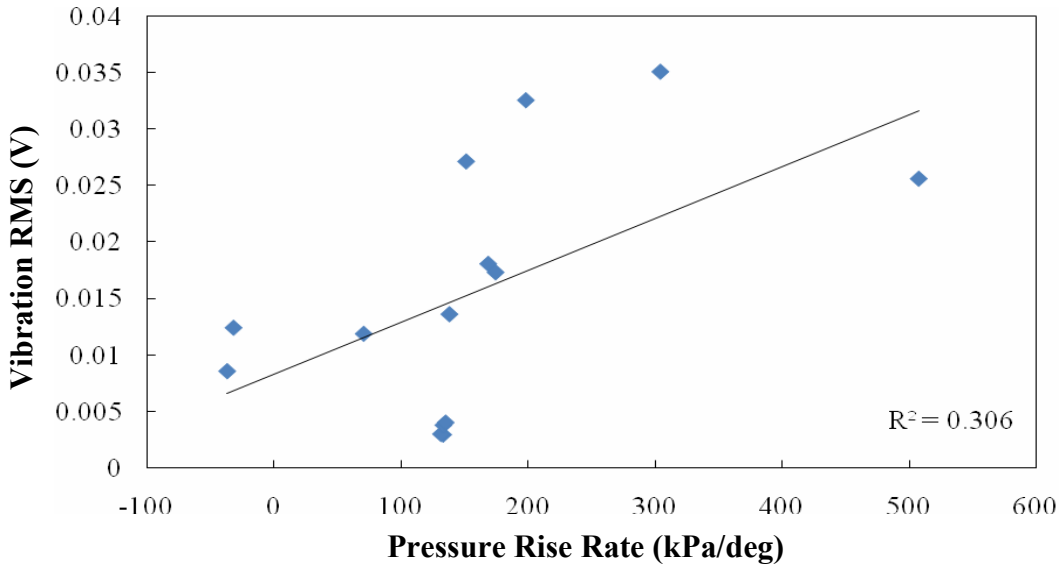

Figure 5.47 Combined -10 – 0 and 1 – 40 CAD segment per-file average 5-8 kHz filtered structure vibration and instantaneous PRR

Recall the cavity resonant vibration frequency band in the vibration and acoustic emissions of the SI exhibited virtually no relation to the PRR. Also recall for per-cycle comparisons, the instantaneous PRR exhibited no relation to any of the vibration and

acoustic emissions analyzed. Conversely, for the CI engine, a relation between the structure vibrations in the cavity resonant frequency band and the instantaneous PRR was clearly evident. This result is most likely due to the difference in the combustion initiating phenomena between the SI and CI engine. The spark ignited combustion exhibits a much more controlled burning of the combustion products and therefore slower initial release of energy than that of the auto-ignited combustion present in the CI engine. The auto-ignited combustion results in extremely rapid and less controlled initial burning of the combustion products, also resulting in higher peak cylinder pressures. This rapid release of energy excites the resonant modes of the engine cylinder. The level of excitation of the cylinder resonant mode is not as high for the slower burning SI engine. Operating the SI engine under knocking (or auto-ignition of the combustion products) conditions would verify this conclusion.

6. SUMMARY AND CONCLUSIONS

Experiments were conducted to investigate indication of the rate of pressure rise in an internal combustion engine using vibration/acoustic energy emissions. Past literature has shown acoustic emission is dependent upon the cylinder pressure rise rate at the onset of combustion for compression ignition (CI) engines and spark ignition engines operating with auto-ignition of the fuel-air mixture. Conversely, only minimal acoustic emission investigation has been conducted with regard to a SI engine operating under normal spark initiated combustion.

Structure vibration measurements were conducted on both a small single-cylinder spark ignition engine and a four-cylinder Mercedes 1.7L diesel engine. Acoustic measurements were taken solely on the SI engine operating under normal spark-ignited combustion. The structure vibrations on the SI engine were collected to mainly assist in determining transmission paths of the acoustic energy, however interesting results were seen when compared to the average cylinder pressure rise rate (PRR). Due to limited time, only structure vibrations were recorded for the CI engine.

To characterize the cylinder PRR, two different methods of determining a PRR value was used. First, for the SI engine, to quantify a per-cycle average PRR occurring at the onset of combustion, a least-squares linear regression line was constructed from spark (or start-of-combustion) to the peak cylinder pressure. The slope of this regression line was used as an average PRR value. In an effort to investigate indication of the peak instantaneous PRR, the first derivative of the cylinder pressure was numerically determined using the central difference method. The per-cycle peak value of the

derivative during combustion was used to represent the instantaneous PRR. This value was used for both the SI and CI investigations.

Rather than analyzing the entire frequency spectrum of the vibration and acoustic signals, specific frequency bands were selected to represent combustion generated vibration/acoustic energy and cavity resonant vibration/acoustic energy. To determine the cavity resonant modes for each engine, the fuel-air mixture in the engine cylinder just before top-dead-center (TDC) was modeled as a circular disk. The solution to the cylindrical wave equation resulted in a wave pressure as a function of Bessel's Function of the first kind. Therefore, the resonant frequency modes of the disk were dependent upon the roots of the first derivative of Bessel's Functions of the first kind. The cavity resonant mode for the SI engine was determined to be 6.4 kHz, while the cavity resonant mode for the CI engine was determined to be 7.3 kHz. Since past literature had shown the first circumferential cavity resonant mode as being dominant, a frequency band of 6.0 – 6.6 kHz was chosen to represent the cavity resonance for the SI engine. Past literature had also shown the spectral density of the cylinder pressure was a good indicator of cavity resonant modes for auto-ignited combustion. Therefore, a frequency spectrum was constructed from the CI engine cylinder pressure spectrum a frequency band of 5.0 – 8.0 kHz was selected to represent the cavity resonant frequencies.

To establish frequencies in the vibration/acoustic emissions representative of combustion, the Short-Time-Fourier-Transform (STFT) was implemented on the vibration and acoustic signals to simultaneously investigate the temporal and spectral distributions of energy. Attention was focused on time segments containing only combustion. From this analysis, the frequency band chosen to represent combustion

generated energy in the acoustic emission was 500 – 700 Hz while the 2000 – 2500 Hz frequency band was chosen to represent combustion generated energy in the structure vibrations. Combustion frequency investigation was not conducted for the CI engine. In order to compare the spectral content in each frequency band selected to the cylinder PRR, an RMS value for the spectral density in each frequency band was calculated.

Initial experiments of the SI engine were conducted at a mid-speed, high-load set point. The results from these experiments showed an increase in the acoustic emission in the 500 – 700 and 2000 – 2500 Hz frequency bands with an increase in the average PRR. The 6000 – 6600 Hz frequency band was not initially investigated. From these results, a test matrix of varied speed and load was developed and used to conduct experiments on the SI engine. In general, the vibration and acoustic emission increased with speed and load. However, it was seen that the cylinder PRR increased only with load and actually decreased with speed. Therefore, the average vibration and acoustic emissions at each operating condition were plotted as a function of the average PRR. Interestingly, the magnitude of both the vibration and acoustic emissions increased with the increase in PRR. However the dependence on speed was made evident. If engine set points operating at the same load were compared, the PRR decreased with speed as the vibration and acoustic emissions increased. Conversely, if same speed engine set points were compared, the vibration and acoustic emissions exhibited increasing trends with increasing PRR. These results indicated the relation between the vibration and acoustic emissions and the cylinder PRR were dependent upon both engine speed and load, thus limiting their usefulness as indicators.

Finally, per-cycle comparisons between the vibration and acoustic emission of the SI engine and the per-cycle PRR were conducted. It was desired to investigate the ability of the per-cycle vibration and acoustic emissions of the engine for predicting the per-cycle PRR, indicative of the energy release. It was concluded for low engine speed and load engine operating set points; no relation between the vibration or acoustic emissions and the average PRR was established. This conclusion was established for all low-load set points, regardless of engine speed. Also, no relation was seen in the per-cycle results between any frequency band of the vibration and acoustic emissions at any set point and instantaneous PRR for the SI engine. Moreover, no relation was seen between the 6000 – 6600 Hz frequency band and average PRR for either vibration or acoustic emissions. It was concluded the spark initiated combustion does not excite the first circumferential cylinder cavity resonances to a level proportional to the release of energy from the combustion process. Interestingly, as the load was increased, the 500 – 700 and 2000 – 2500 Hz frequency bands exhibited increasing trends with the increase in PRR. This was seen at both the 2520 rpm and 3000 rpm engine speeds. It was concluded the per-cycle vibration and acoustic emissions were less likely to indicate the level of cylinder PRR at low engine speed and load operating set points. However, for high speed/load engine set points, the vibration and acoustic emission did show consistently upward trends. This provided indication of the PRR by the vibration and acoustic emissions under high speed and load engine operating conditions.

Investigation of a Mercedes 1.7L diesel engine was conducted to investigate the ability of the structure vibrations to indicate cylinder PRR for an engine undergoing auto-ignition. The CI engine was operated at a constant speed and load of 1500 rpm, 37.3 N-

m, with the injection type varied resulting in different combustion schemes. Five engine cycles was collected for each engine set point.

Initially, five cycle average comparisons were made between the 5.0 – 8.0 kHz structure vibration RMS and the instantaneous PRR. These results showed the structure vibrations did increase with an increase in PRR. Next, per-cycle comparisons were conducted to investigate the ability of the structure vibrations to predict the PRR. For this comparison, the analysis for each cycle was split into two windows to segregate combustion initiated by the pilot injection and combustion resulting from the main injection. Separately, these two segments showed moderate to strong linear correlations between the cavity resonant vibrations and the instantaneous PRR. However, when the results from these segments were combined on one plot, the general trend of increasing vibrations with PRR remained, but the data became much more scattered. Therefore, it was concluded more data should be collected and analyzed before definite conclusions are drawn. However, the current results do suggest a relation between the structure vibrations and PRR.

Regardless of the lack of relation between the vibration and acoustic emissions in the SI engine and the instantaneous PRR, there was a clear correlation between the emissions and the average PRR. Therefore, it is concluded that as the initial release of energy increases for the SI or CI engines, the vibration and acoustic emissions become more influenced by this release in energy. Consequently, for the more rapid initial release of energy, the non-intrusive sensing techniques could indicate the level of this energy release.

7. RECOMMENDATIONS

The results of this investigation revealed a possible relation between the vibration and acoustic energy emissions of an internal combustion engine and the cylinder pressure rise rate. This result was determined for an SI engine subject to normal spark-ignited combustion and a CI engine subject to normal auto-ignition of the fuel-air mixture. Although the combustion development is different in the two engines, the results have exposed similarities in the behavior of the vibration and acoustic emissions to the cylinder PRR in each system. However there are issues that could be addressed to further this work.

Performing the SI engine experiments on a small-single cylinder engine is advantageous due to the exclusion of signal interference from other operating cylinders. However, to the vast majority of SI internal combustion engines being multi-cylinder, it is only appropriate to expand this research to a multi-cylinder SI engine. This would provide another set of results for a different engine platform. Hopefully, there would be similarities found between the different engine platforms that would provide information useful in engine design and sensor development.

Further investigation into the selected cavity resonant mode frequency band of 6000 – 6600 Hz should be conducted. This would most likely be best analyzed while the SI engine is being operated under auto-ignition of the combustion products. By doing this, the cylinder cavity resonant frequencies will be excited to a much higher level than normal, and therefore the cylinder pressure signal could be used to better extract the cavity resonant modes, as was done with the CI engine.

Thirdly, the use of a linear regression line to model the average PRR should be investigated. As was seen the low load set points exhibited different cylinder pressure development than that of the high load. It would be advantageous to investigate the vibration and acoustic emission with relation to the amount of heat released in the cylinder, the mass fraction of the burned gasses, or the rate at with the heat is released in the cylinder. Such an investigation would encompass other details of the combustion process. Investigation with regard to the heat release and mass fraction burned should be done with the CI engine data as well.

Fourthly, smoothing the SI engine cylinder pressure data should be considered in order to better approximate the numerical derivative of the cylinder pressure. For set point average results the average and instantaneous PRR values exhibited similar trends. However, the per-cycle comparisons showed no relation between the vibration or acoustic emissions and the instantaneous PRR at any engine operating condition. If discontinuities are present in the cylinder pressure waveform, smoothing the SI engine cylinder pressure may result in correlations comparable to the average PRR results.

Finally, the CI engine should be operated at other speed and load set points. Doing this would reveal any dependence the structure vibrations have on speed and load. Acoustic emission measurements should also be conducted for comparison to the SI engine results.

APPENDIX A

ACCELEROMETER DATA SHEET

Model Number 352B10	ACCELEROMETER, ICP®	Revision D ECN #: 24842

Performance	ENGLISH	SI	
Sensitivity (±10 %)	10 mV/g	1.02 mV/(m/s²)	
Measurement Range	±500 g pk	±4905 m/s² pk	
Frequency Range (±5 %)	2 to 10000 Hz	2 to 10000 Hz	
Frequency Range (±10 %)	1 to 17000 Hz	1 to 17000 Hz	
Resonant Frequency	≥65 kHz	≥65 kHz	
Broadband Resolution (1 to 10000 Hz)	0.003 g rms	0.03 m/s² rms	[1]
Non-Linearity	≤1 %	≤1 %	[3]
Transverse Sensitivity	≤5 %	≤5 %	
Environmental			
Overload Limit (Shock)	±10000 g pk	±98100 m/s² pk	
Temperature Range (Operating)	-65 to +250 °F	-54 to +121 °C	[2]
Temperature Response	See Graph	See Graph	
Electrical			
Excitation Voltage	18 to 30 VDC	18 to 30 VDC	
Constant Current Excitation	2 to 20 mA	2 to 20 mA	
Output Impedance	≤200 ohm	≤200 ohm	
Output Bias Voltage	7 to 11 VDC	7 to 11 VDC	
Discharge Time Constant	0.3 to 1.0 sec	0.3 to 1.0 sec	
Settling Time (within 10% of bias)	<3 sec	<3 sec	
Spectral Noise (1 Hz)	1000 µg/√Hz	9810 (µm/s²)/√Hz	[1]
Spectral Noise (10 Hz)	300 µg/√Hz	2943 (µm/s²)/√Hz	[1]
Spectral Noise (100 Hz)	80 µg/√Hz	785 (µm/s²)/√Hz	[1]
Spectral Noise (1 kHz)	25 µg/√Hz	308 (µm/s²)/√Hz	[1]
Physical			
Sensing Element	Ceramic	Ceramic	
Sensing Geometry	Shear	Shear	
Housing Material	Titanium	Titanium	
Sealing	Hermetic	Hermetic	
Size (Height x Diameter)	0.32 in x 0.24 in	8.1 mm x 6.1 mm	
Weight	0.03 oz	0.7 gm	[1]
Electrical Connector	Solder pins with attached cable	Solder pins with attached cable	
Electrical Connection Position	Top	Top	
Cable Termination	10-32 Coaxial Plug	10-32 Coaxial Plug	
Cable Length	10 ft	3 m	
Cable Type	030 Coaxial	030 Coaxial	
Mounting	Adhesive	Adhesive	

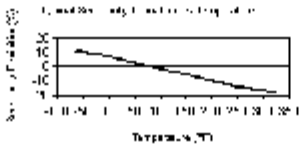

All specifications are at room temperature unless otherwise specified.
In the interest of constant product improvement, we reserve the right to change specifications without notice.
ICP® is a registered trademark of PCB group, Inc.

Optional Versions (Optional versions have identical specifications and accessories as listed for standard model except where noted below. More than one option maybe used.)

HT - High temperature, extends normal operation temperatures		
Temperature Range (Operating)	-65 to 325 °F	-54 to 163 °C
W - Water Resistant Cable		
Temperature Range (Operating)	-20 to 220 °F	-29 to 104 °C
Electrical Connector	Sealed Integral Cable	Sealed Integral Cable
Cable Type	018 Coaxial	018 Coaxial

Notes
[1] Typical.
[2] 250° F to 325° F data valid with HT option only.
[3] Zero-based, least-squares, straight line method.
[4] See PCB Declaration of Conformance PS023 for details.

Supplied Accessories
080A109 Petro Wax (1)
080A90 Quick Bonding Gel (1)
ACS-1 NIST traceable frequency response (10 Hz to upper 5% point). (1)

Entered: BAN	Engineer: BAM	Sales: WDC	Approved: JJB	Spec Number:
Date: 08/18/2006	Date: 08/21/2006	Date: 08/21/2006	Date: 08/21/2006	15312

PCB PIEZOTRONICS
VIBRATION DIVISION
3425 Walden Avenue
Depew, NY 14043
UNITED STATES
Phone: 888-684-0013
Fax: 716-685-3886
E-mail: vibration@pcb.com
Web site: www.pcb.com

Model Number 352B10	ACCELEROMETER, ICP®	Revision D ECN #: 24842

Performance	ENGLISH	SI	
Sensitivity (±10 %)	10 mV/g	1.02 mV/(m/s²)	
Measurement Range	±500 g pk	±4905 m/s² pk	
Frequency Range (±5 %)	2 to 10000 Hz	2 to 10000 Hz	
Frequency Range (±10 %)	1 to 17000 Hz	1 to 17000 Hz	
Resonant Frequency	≥65 kHz	≥65 kHz	
Broadband Resolution (1 to 10000 Hz)	0.003 g rms	0.03 m/s² rms	[1]
Non-Linearity	≤1 %	≤1 %	[3]
Transverse Sensitivity	≤5 %	≤5 %	
Environmental			
Overload Limit (Shock)	±10000 g pk	±98100 m/s² pk	
Temperature Range (Operating)	-65 to +250 °F	-54 to +121 °C	[2]
Temperature Response	See Graph	See Graph	
Electrical			
Excitation Voltage	18 to 30 VDC	18 to 30 VDC	
Constant Current Excitation	2 to 20 mA	2 to 20 mA	
Output Impedance	≤200 ohm	≤200 ohm	
Output Bias Voltage	7 to 11 VDC	7 to 11 VDC	
Discharge Time Constant	0.3 to 1.0 sec	0.3 to 1.0 sec	
Settling Time (within 10% of bias)	<3 sec	<3 sec	
Spectral Noise (1 Hz)	1000 µg/√Hz	9810 (µm/s²)/√Hz	[1]
Spectral Noise (10 Hz)	300 µg/√Hz	2943 (µm/s²)/√Hz	[1]
Spectral Noise (100 Hz)	80 µg/√Hz	785 (µm/s²)/√Hz	[1]
Spectral Noise (1 kHz)	25 µg/√Hz	308 (µm/s²)/√Hz	[1]
Physical			
Sensing Element	Ceramic	Ceramic	
Sensing Geometry	Shear	Shear	
Housing Material	Titanium	Titanium	
Sealing	Hermetic	Hermetic	
Size (Height x Diameter)	0.32 in x 0.24 in	8.1 mm x 6.1 mm	
Weight	0.03 oz	0.7 gm	[1]
Electrical Connector	Solder pins with attached cable	Solder pins with attached cable	
Electrical Connection Position	Top	Top	
Cable Termination	10-32 Coaxial Plug	10-32 Coaxial Plug	
Cable Length	10 ft	3 m	
Cable Type	030 Coaxial	030 Coaxial	
Mounting	Adhesive	Adhesive	

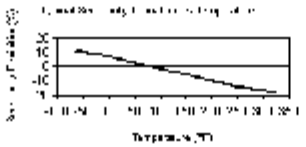

All specifications are at room temperature unless otherwise specified.
In the interest of constant product improvement, we reserve the right to change specifications without notice.
ICP® is a registered trademark of PCB group, Inc.

Optional Versions (Optional versions have identical specifications and accessories as listed for standard model except where noted below. More than one option maybe used.)

HT - High temperature, extends normal operation temperatures		
Temperature Range (Operating)	-65 to 325 °F	-54 to 163 °C
W - Water Resistant Cable		
Temperature Range (Operating)	-20 to 220 °F	-29 to 104 °C
Electrical Connector	Sealed Integral Cable	Sealed Integral Cable
Cable Type	018 Coaxial	018 Coaxial

Notes
[1] Typical.
[2] 250° F to 325° F data valid with HT option only.
[3] Zero-based, least-squares, straight line method.
[4] See PCB Declaration of Conformance PS023 for details.

Supplied Accessories
080A109 Petro Wax (1)
080A90 Quick Bonding Gel (1)
ACS-1 NIST traceable frequency response (10 Hz to upper 5% point). (1)

Entered: BAN	Engineer: BAM	Sales: WDC	Approved: JJB	Spec Number:
Date: 08/18/2006	Date: 08/21/2006	Date: 08/21/2006	Date: 08/21/2006	15312

PCB PIEZOTRONICS VIBRATION DIVISION
3425 Walden Avenue
Depew, NY 14043
UNITED STATES
Phone: 888-684-0013
Fax: 716-685-3886
E-mail: vibration@pcb.com
Web site: www.pcb.com

Model Number 320C17	SHEAR ICP® ACCELEROMETER	Revision C ECN #: 23473

Performance	ENGLISH	SI	
Sensitivity (±10 %)	10 mV/g	1.02 mV/(m/s²)	
Measurement Range	±500 g pk	±4900 m/s² pk	
Frequency Range (±5 %)	2.0 to 10000 Hz	2.0 to 10000 Hz	
Frequency Range (±10 %)	1.5 to 18000 Hz	1.5 to 18000 Hz	
Frequency Range (±3 dB)	0.7 to 30000 Hz	0.7 to 30000 Hz	
Resonant Frequency	≥60 kHz	≥60 kHz	
Broadband Resolution (1 to 10000 Hz)	0.005 g rms	0.05 m/s² rms	[1]
Non-Linearity	≤1 %	≤1 %	[2]
Transverse Sensitivity	≤5 %	≤5 %	[3]
Environmental			
Overload Limit (Shock)	±10000 g pk	±98100 m/s² pk	
Temperature Range (Operating)	-100 to +325 °F	-73 to +163 °C	
Temperature Response	See Graph	See Graph	[1]
Base Strain Sensitivity	≤0.005 g/με	≤0.05 (m/s²)/με	[1]
Electrical			
Excitation Voltage	18 to 30 VDC	18 to 30 VDC	
Constant Current Excitation	2 to 20 mA	2 to 20 mA	
Output Impedance	≤100 ohm	≤100 ohm	
Output Bias Voltage	8 to 12 VDC	8 to 12 VDC	
Discharge Time Constant	0.25 to 1 sec	0.25 to 1 sec	
Setting Time (within 10% of bias)	<5 sec	<5 sec	
Spectral Noise (1 Hz)	2800 μg/√Hz	27468 (μm/s²)/√Hz	[1]
Spectral Noise (10 Hz)	500 μg/√Hz	4905 (μm/s²)/√Hz	[1]
Spectral Noise (100 Hz)	90 μg/√Hz	883 (μm/s²)/√Hz	[1]
Spectral Noise (1 kHz)	30 μg/√Hz	294 (μm/s²)/√Hz	[1]
Physical			
Sensing Element	Quartz	Quartz	
Sensing Geometry	Shear	Shear	
Housing Material	Titanium	Titanium	
Sealing	Hermetic	Hermetic	
Size (Hex x Height)	0.28 in x 0.55 in	7.1 mm x 14.0 mm	
Weight	0.06 oz	1.7 gm	[1]
Electrical Connector	2-Pin Solder	2-Pin Solder	
Electrical Connection Position	Top	Top	
Mounting Thread	5-40 Male	5-40 Male	
Mounting Torque	8 to 12 in-lb	90 to 135 N-cm	

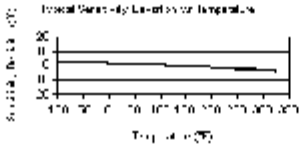

All specifications are at room temperature unless otherwise specified.
In the interest of constant product improvement, we reserve the right to change specifications without notice.
ICP® is a registered trademark of PCB group, Inc.

Optional Versions (Optional versions have identical specifications and accessories as listed for standard model except where noted below. More than one option maybe used.)

A - Adhesive Mount
Supplied Accessory: Model 080A90 Quick bond Gel (for use with accelerometer adhesive mtg bases to fill gaps on rough surfaces) replaces Model 080A15

J - Ground Isolated		
Frequency Range (5 %)	8 kHz	8 kHz
Frequency Range (10 %)	12 kHz	12 kHz
Frequency Range (3 dB)	25 Hz	25 kHz
Resonant Frequency	≥50 kHz	≥50 kHz
Electrical Isolation (Base)	>10^8 ohm	>10^8 ohm
Size (Hex x Height)	0.38 in x 0.53 in	9.7 mm x 13.5 mm
Weight	0.10 oz	2.8 gm

M - Metric Mount
Supplied Accessory: Model M080A15 Metric adhesive base, 0.31" hex x 0.125" thk, M3 x 0.50 thd, aluminum with insulating hardcoat finish replaces Model 080A15

Notes
[1] Typical.
[2] Zero-based, least-squares, straight line method.
[3] Transverse sensitivity is typically <= 3%.
[4] See PCB Declaration of Conformance PS023 for details.

Supplied Accessories
080A109 Petro Wax (1)
080A15 Adhesive Mounting Base (1)
ACS-1 NIST traceable frequency response (10 Hz to upper 5% point). (1)

Entered: BAN	Engineer: JJB	Sales: WDC	Approved: BAM	Spec Number:
Date: 01/16/2006	Date: 01/16/2006	Date: 01/16/2006	Date: 01/16/2006	9960

PCB PIEZOTRONICS VIBRATION DIVISION
3425 Walden Avenue
Depew, NY 14043
UNITED STATES
Phone: 888-684-0013
Fax: 716-685-3886
E-mail: vibration@pcb.com
Web site: www.pcb.com

Model Number 357B04	ACCELEROMETER, CHARGE OUTPUT	Revision H ECN #: 25956

Performance	ENGLISH	SI	
Sensitivity (±15 %)	10 pC/g	1.02 pC/(m/s²)	
Measurement Range	±2000 g pk	±19600 m/s² pk	
Frequency Range (+5 %)	9 kHz	9 kHz	[2]
Frequency Range (+10 %)	12 kHz	12 kHz	[2]
Frequency Range (+3 dB)	18 kHz	18 kHz	[2]
Resonant Frequency	≥38 kHz	≥38 kHz	
Non-Linearity	≤1 %	≤1 %	[3]
Transverse Sensitivity	≤5 %	≤5 %	
Environmental			
Overload Limit (Shock)	±21000 g pk	±206010 m/s² pk	
Temperature Range	-95 to +500 °F	-71 to +260 °C	
Temperature Response	See Graph	See Graph	[1]
Base Strain Sensitivity	0.0002 g/με	0.002 (m/s²)/με	[1]
Electrical			
Capacitance	750 pF	750 pF	[1]
Insulation Resistance (at 70° F [21°C])	$>10^{12}$ ohm	$>10^{12}$ ohm	
Insulation Resistance (at 500°F)	$>10^{10}$ ohm	$>10^{10}$ ohm	[1]
Output Polarity	Negative	Negative	
Physical			
Sensing Element	Ceramic	Ceramic	
Sensing Geometry	Shear	Shear	
Housing Material	Titanium	Titanium	
Sealing	Hermetic	Hermetic	
Size (Hex x Height)	0.5 in x 1.19 in	12.7 mm x 30.2 mm	
Weight	0.39 oz	11 gm	[1]
Electrical Connector	10-32 Coaxial Jack	10-32 Coaxial Jack	
Electrical Connection Position	Top	Top	
Mounting Thread	10-32 Female	10-32 Female	

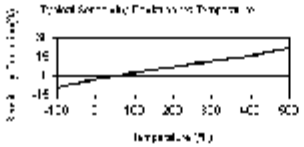

All specifications are at room temperature unless otherwise specified.
In the interest of constant product improvement, we reserve the right to change specifications without notice.
ICP® is a registered trademark of PCB group, Inc.

Optional Versions (Optional versions have identical specifications and accessories as listed for standard model except where noted below. More than one option maybe used.)

J - Ground Isolated			
Frequency Range (+5 %)	7000 Hz	7000 Hz	
Frequency Range (+10 %)	8000 Hz	8000 Hz	
Resonant Frequency	≥30 kHz	≥30 kHz	
Electrical Isolation (Base)	$>10^{8}$ ohm	$>10^{8}$ ohm	
P - Positive Output Polarity			
Output Polarity	Positive	Positive	
W - Water Resistant Cable			[4]
Electrical Connector	Sealed Integral Cable	Sealed Integral Cable	
Electrical Connection Position	Top	Top	

Notes
[1] Typical.
[2] Low frequency response is determined by external signal conditioning electronics.
[3] Zero-based, least-squares, straight line method.
[4] Capacitance will vary based on cable length. Typical cable capacitance is 29 pF/ft (95 pF/m).

Supplied Accessories
080A109 Petro Wax (1)
081B05 Mounting Stud (10-32 to 10-32) (1)
ACS-1 NIST traceable frequency response (10 Hz to upper 5% point). (1)
M081B05 Mounting Stud 10-32 to M6 X 0.75 (1)

Entered: BLS	Engineer: JJB	Sales: WDC	Approved: BAM	Spec Number:
Date: 03/13/2007	Date: 03/13/2007	Date: 03/14/2007	Date: 03/14/2007	1005

PCB PIEZOTRONICS
VIBRATION DIVISION
3425 Walden Avenue
Depew, NY 14043
UNITED STATES
Phone: 888-684-0013
Fax: 716-685-3886
E-mail: vibration@pcb.com
Web site: www.pcb.com

VP50/1

VP50/1
knock Sensor Monitor

- **High Sensitivity**
- **Wide Operating Temperature range**
- **Good high frequency response**
- **Integral M12 stud**
- **Electrically isolated construction**
- **Integral connector**
- **High volume construction**
- **Fully endurance tested**

Features

The VP50/1 is a piezo electric accelerometer specifically designed for knock sensing in automotive control systems. The experience gained during many years of development and production of piezo electric transducers has enabled Lamerholm Fleming to produce a low cost sensor which fully satisfies automotive industry demands for performance, reliability and environmental endurance.

An exhaustive test programme has been undertaken to prove resistance to temperature cycling, vibration, humidity, salt spray and other under bonnet hazards. Rigorous test and QA procedures during manufacture assure consistent performance and reliability.

The VP50/1 has a wide band response tightly specified from 2kHz to 20kHz to ensure maximum system performance with simple electronic filters.

High sensitivity and full ground isolation help minimise electrical interference problems. An integral stud and connector result in a straightforward one component installation.

The VP50/1 is in large volume production and its numerous advantages have made it the sole or first choice for a number of major motor manufacturers.

Lamerholm Fleming Ltd
Isaac Newton House, Norton Road
Stevenage, Hertfordshire - SG1 2BB
Tel: +44 (0) 1438 728844 - Fax: +44 (0) 1438 742326
Email: sales@shocklog.com Web: www.shocklog.com

Lamerholm Fleming
Data intelligence

VP50/1

Technical Specification

Complete Sensor		min	max.	unit
Sensitivity (@2 KHz, 300pF		20.4	27.6	mV/g
Charge Sensitivity		2	34	pC/g
Capacitance		825	1375	pF
Frequency response	1Hz - 2kHz		±100	%
	2kHz - 10kHz	-5	±100	%
	10kHz - 13kHz		±20	%
	13kHz - 18kHz		±60	%
	18kHz - 20kHz		±100	%
Temperature coefficient of voltage sensitivity			±15	%°C
Capacitance to ground	Pin B to case	150	450	PF
Leakage to ground	@2V	>100		Mohm
	@100V	>100		Mohm
Leakage resistance	Pin A to pin B @ 2V	>100		Mohm
Noise isolation	@6kHz	>55		DB
Operating Temperature		-30	+120	°C
Maximum acceleration		-100	+100	G
Weight			55	Gm
Mounting torque		10	15	N/m
Connections	Integral connector			
Case material	Mild steel zinc plated			
Connector material	ICI Maranyl A390			
Seal	Epoxy			
Marking	Code and batch no.			

All performance data applies at 20 ± 5 °C except frequency response which holds over the entire operating temperature range.

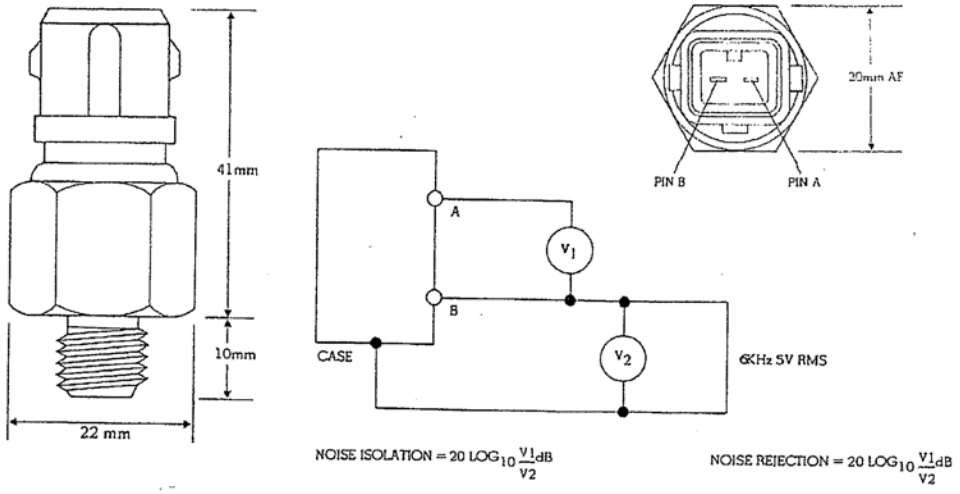

The VP50 accelerometer includes features which are the subject of world wide patents or patent applications and/or other intellectual property. While the information contained in this document is believed to be accurate no responsibility can be accepted for its use; nor for any infringements of patents or other rights of third parties which may result from its use. Lamerholm Fleming Ltd reserve the right to modify performance specifications without notice.

Lamerholm Fleming makes no warranty for the use of its products, other than those expressly contained in the Company's standard Terms and Conditions of Sale which are available on request. Lamerholm Fleming assumes no responsibility for any errors which may appear in this document, reserves the right to change devices or specifications detailed herein at any time without notice, and does not make any commitment to update the information contained herein. No licenses to patents or other intellectual property of Lamerholm Fleming Ltd are granted by the Company in connection with the sale of Lamerholm Fleming products, expressly or by implication. Lamerholm Fleming products are not authorised for use as critical components in life support devices or systems.

Lamerholm Fleming Ltd
Isaac Newton House, Norton Road
Stevenage, Hertfordshire - SG1 2BB
Tel: +44 (0) 1438 728844 - Fax: +44 (0) 1438 742326
Email: sales@shocklog.com Web: www.shocklog.com

Lamerholm Fleming
Data intelligence

APPENDIX B

DIGITAL FILTER SPECIFICATIONS

```
% Generated by MATLAB(R) 7.4 and the Signal Processing Toolbox 6.7.
%
% Generated on: 11-Jan-2008 15:02:33
%

% Coefficient Format: Decimal

% Discrete-Time FIR Filter (real)
% -------------------------------
% Filter Structure  : Direct-Form FIR
% Filter Length     : 24
% Stable            : Yes
% Linear Phase      : Yes (Type 2)


Numerator:
-0.01367060609207638
-0.019982963709003498
 0.0066746031287919097
 0.031467266163462383
 0.012808607224564547
 0.0035939565649825162
 0.049831526771004664
 0.040463735210806158
-0.11225228364718461
-0.21462988300631272
-0.035718919798688284
 0.2492606094518911
 0.2492606094518911
-0.035718919798688284
-0.21462988300631272
-0.11225228364718461
 0.040463735210806158
 0.049831526771004664
 0.0035939565649825162
 0.012808607224564547
 0.031467266163462383
 0.0066746031287919097
-0.019982963709003498
      -0.01367060609207638
```

```
function Hd = FIRLSO_5_8khz
%FIRLSO_5_8KHZ Returns a discrete-time filter object.

% M-File generated by MATLAB(R) 7.4 and the Signal
Processing
% Toolbox 6.7.
%
% Generated on: 21-Dec-2007 09:59:08
%

% FIR least-squares Bandpass filter designed using the
% FIRLS
% function.

% All frequency values are in Hz.
Fs = 36000;  % Sampling Frequency

N      = 23;     % Order
Fstop1 = 2500;   % First Stopband Frequency
Fpass1 = 5000;   % First Passband Frequency
Fpass2 = 8000;   % Second Passband Frequency
Fstop2 = 10500;  % Second Stopband Frequency
Wstop1 = 1;      % First Stopband Weight
Wpass  = 1;      % Passband Weight
Wstop2 = 1;      % Second Stopband Weight

% Calculate the coefficients using the FIRLS function.
b  = firls(N, [0 Fstop1 Fpass1 Fpass2 Fstop2…
 Fs/2]/(Fs/2), [0 0 1 1 0 0], [Wstop1 Wpass Wstop2]);
Hd = dfilt.dffir(b);

% [EOF]
```

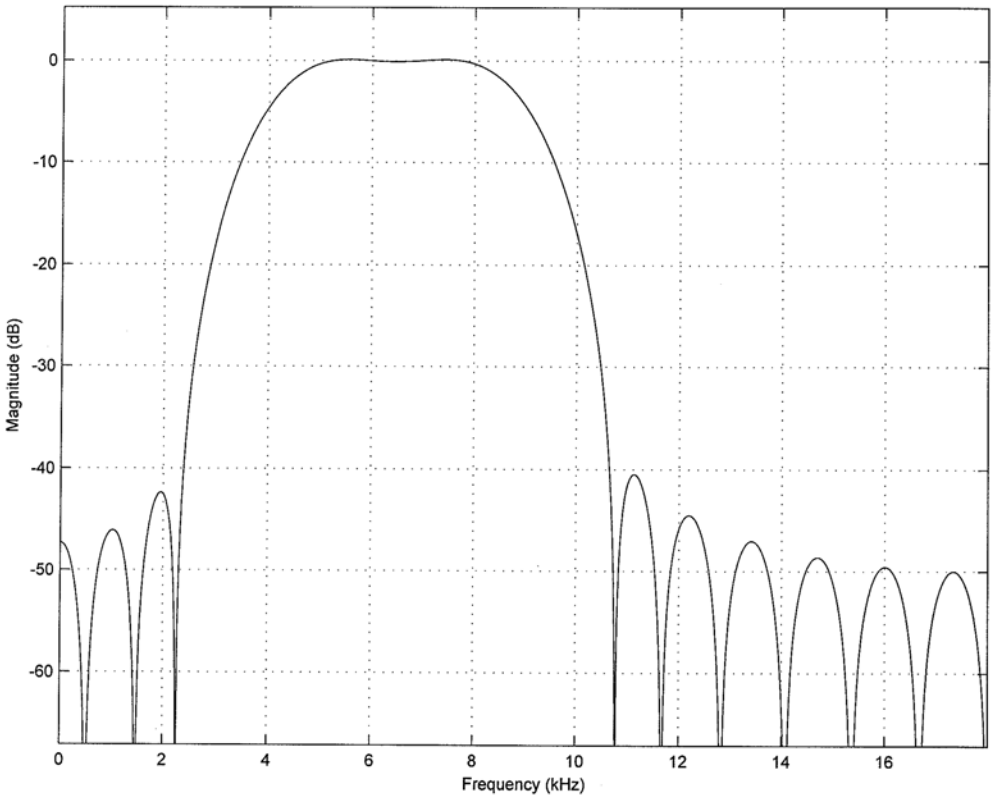

Figure B.1 Filter Response Curve

BIBLIOGRAPHY

1. Priede, T. "Relation Between Form of Cylinder-Pressure Diagram and Noise in Diesel Engines." Proceedings of the Institution of Mechanical Engineers. London: Institution of Mechanical Engineers, 1960. 63-77.

2. Anderton, D. "Relation Between Combustion System and Engine Noise." SAE 790270. Society of Automotive Engineers, 1979.

3. Schnieder, M., K. Schmillian and F. Pischinger. "Regularities of Cylinder Pressure Oscillations and Their Effects on the Combustion Process and Noise." SAE 872248. Society of Automotive Engineering, 1987.

4. Priede, T. and R.K. Dutkiewicz. "The Effect of Normal Combustion and Knock on Gasoline Engine Noise." SAE 891126. Society of Automotive Engineers, 1989.

5. Schaberg, P.W., T. Priede and R.K. Dutkiewicz. "Effects of a Rapid Pressure Rise on Engine Vibration and Noise." SAE 900013. Society of Automotive Engineers, 1990.

6. Vora, K.C. and B. Ghosh. "Vibration Due to Piston slap and Combustion in Gasoline and Diesel Engines." SAE 911060. Society of Automotive Engineers, 1991.

7. Kanda, Hiroshi, Minoru Okubo and Tohru Yonezawa. "Analysis of Noise Sources and Their Transfer Paths in Diesel Engines." SAE 900014. Society of Automotive Engineers, 1990.

8. Carlucci, A.P., F.F. Chiara and D. Laforgia. "Block Vibration as a Way of Monitoring the Combustion Evolution in a Direct Injection Diesel Engine." SAE 2006-01-1532. Society of Automotive Engineers, 2006.

9. Carlucci, A.P., F.F. Chiara and D. Laforgia. "Analysis of the relation between injection parameter variation and block vibration of an internal combustion diesel engine." Journal of Sound and Vibration (2006): 141 - 164.

10. Chiatti, G. and O. Chiavola. "Experimental Analysis of Combustion Noise in Spark Ignition Engine." SAE 2003-01-1422. Society of Automotive Engineers, 2003.

11. Chiatti, G. and O. Chiavola. "Combustion Induced Noise in Single Cylinder Diesel Engines." SAE 2004-32-0071. Society of Automotive Engineers, 2004.

12. Patro, T.N. "Combustion Induced Powertrain NVH - A Time-Frequency Analysis." SAE 971874. Society of Automotive Engineers, 1997.

13. Villarroel, Grover Zurita and Anders Agren. "Wavelet Transform Analysis of Measurements of Engine Combustion Noise." SAE 972003. Society of Automotive Engineers, 1997.

14. Stoffels, H. and Collings, N. "Effect of gasoline homogeneous charge compression ignition on engine acoustics and vibration," Int. J. Engine Res. 8.1 (2007): 51-62.

15. Souder, Jason S., et al. "Microphones and Knock Sensors for Feedback Control of HCCI Engines." ICEF2004-960. Proceedings of ICEF'04, ASME Internal Combustion Engine Division, 2004.

16. Naber, Jeffery D., et al. "Analysis of Combustion Knock Metrics in Spark-Ignition Engines." SAE 2006-01-0400. Society of Automotive Engineers, 2006.

17. Kinsler, Lawerence E., et al. Fundamentals of Acoustics. 4th. Hoboken, NJ: John Wiley & Sons, Inc., 1999.

18. Heywood, John B. Internal Combustion Engine Fundamentals. New York: McGraw-Hill, Inc., 1988.

19. Devore, Jay L. Probability and Statistics for Engineering and the Sciences. 4th Edition. Wadsworth Publishing Co., 1995, Page 512.

VITA

Jeffery Alexander Massey was born September 7, 1983 in Batesville Arkansas to James and Terrie Massey. He received his B.S. in Engineering with emphasis in Mechanical Engineering from Arkansas State University, Jonesboro, Arkansas, USA in December 2005. Jeffery worked part time during 2005 at Hytrol Conveyor Company as an Engineering Intern and, as an undergraduate, conducted engineering research in the Computational Dynamics Lab at Arkansas State University. In January of 2006, Jeffery began working toward his Master of Science degree under the direction of Dr. James. A. Drallmeier at the Missouri University of Science and Technology, Rolla, Missouri, USA. He worked during the summer of 2007 as an U.S. Department of Energy Higher Education Research Experience (HERE) participant. He also worked as a Graduate Research Assistant as well as a Graduate Teaching Assistant until he received his M.S. in Mechanical Engineering in May 2008 from the Missouri University of Science and Technology (formerly University of Missouri – Rolla).

Jeffery Massey is a participant of the Ronald E. McNair Post-baccalaureate Program. He is also a member of the Society of Automotive Engineers and the American Society of Mechanical Engineers. He served as the Arkansas State University ASME Student Chapter Chair for the 2005-2006 academic school year.